Bachelor Thesis

Degree Project in
Geology 30 hp

The Bonahaven dolomite formation - an evaporitic perspective

Sofie Elvestedt

Stockholm 2025

Department of Geological Sciences
Stockholm University
SE-106 91 Stockholm

Abstract

Member 3 of the Bonahaven Dolomite Formation (BDF) preserves sedimentological and mineralogical evidence consistent with deposition in a sabkha environment. Abundance of heavy minerals and rare earth element-bearing phases point to anomalously high detrital input for a sabkha, inferred to be linked to extreme levels of precipitation. These interpretations are based on thin section analyses by polarising microscope, SEM and Raman spectroscopy. A total of 14 stratigraphic beds contain evidence of vertical recycling of ions, abundance of pseudomorphs of intrasedimentary evaporites, and features such as haloturbation and dissolution of salt beds. Furthermore, metamorphic biotite is present in seven beds, suggesting that greenschist facies metamorphism either reached biotite-grade conditions or that biotite stabilisation was controlled by bulk rock chemistry under chlorite-grade conditions.

These findings support a revised interpretation of the depositional and possibly metamorphic history of Member 3 of the BDF. The interpretation presented in this study aligns with post-Sturtian paleoclimate conditions, marked by extreme greenhouse conditions in the aftermath of Snowball Earth.

Table of Contents

List of Figures

List of Tables

List of appendices

1. Introduction

The rock record allows us to trace variations in Earth's climate throughout its history. A spectacular example of past climate recorded in ancient strata is described by Hoffman et al. (2017) - the Snowball Earth and the extreme greenhouse climate that followed. This study focuses on Member 3 (Spencer & Spencer, 1972) of the Bonahaven Dolomite Formation (BDF), a remarkable example of post-Snowball conditions.

The BDF consists of sedimentary rocks, including dolomitic strata, microbial mats, and stromatolites - features that require warm, shallow conditions to form (Warren, 2016). The formation includes both syn- and epigenetic structures, from which their genesis can be interpreted. The BDF directly overlies a 1.1 km-thick glaciogenic succession known as the Port Askaig Formation (PAF), which most authors associate with the Sturtian Snowball Earth glaciation (Rugen et al., 2024; Hoffman et al., 2017).

The Snowball Earth hypothesis (Kirschvink, 1992) suggests globally synchronous glaciation at equatorial latitudes for millions of years implying that the entire planet was frozen over. Ice would then have blocked CO2 uptake by the oceans and weathering of rocks, leading to the accumulation of large amounts of atmospheric CO2 from volcanic eruptions, ending Snowball Earth.

The Sturtian glaciation lasted from 716 to 659 Ma, encompassing both glacials and interglacials, and included a possible Snowball Earth panglaciation. It was followed by the Marinoan glaciation 645 to 635 Ma (Hoffman et al., 2017). These two events mark the start and end of the Cryogenian period and the BDF was deposited between these two events (Rugen et al., 2024). Geochemical data from the end of the Sturtian deglaciation suggests atmospheric CO2 levels ranging from 10,000 to 100,000 ppm. This extreme CO2 buildup counteracted the albedo effect and ultimately led to the melting of Snowball Earth (Hoffman et al., 2017).

During the Quaternary, it took approximately 10,000 years for full deglaciation after the Last Glacial Maximum. Various climate modeling studies suggest that it took only about 2,000 years to melt the Sturtian Snowball Earth, supporting the idea of extreme atmospheric CO2 levels (Hoffman et al., 2017). This rapid warming would have been amplified by factors as stronger radiative forcing during the Cryogenian period than today (Hoffman et al., 2017) and melting of methane-rich permafrost (Kennedy et al., 2001).

The post-Sturtian climate is expected to be characterized by high temperatures and an adjoined intense evaporation/precipitation cycle (Hoffman et al., 2017). Heavy precipitation leads to severe weathering of continental rocks, causing high rates of sedimentation and release of various ions, as HCO3-, Ca2+ and Mg2+, into the ocean (Hoffman et al., 2017). Deglaciation also enables CO2 to dissolve in water, leading to ocean acidification (Rugen et al., 2024) (Hoffman et al., 2017). Melting ice would cause flooding of continental shelves and create a quickly warming freshwater lid segregating the uppermost 2 km of ocean from the underlying hypersaline, cold, and dense waters. This would persist until whole ocean mixing (on timescales of 4×10^4 to 6×10^4 years) equilibrates salinity, temperature, and ocean acidification. The heavy precipitation would also strengthen water flow and storms, transporting detrital products including heavier minerals. Intense weathering can be observed in the rock record through the rapid oversaturation of carbonate minerals, which accumulate and precipitate in the upper freshwater lid (Hoffman et al., 1998, Hoffman at al., 2017). Along continental shelves, where the formation of dolostone and limestone is favored (Warren, 2016), sediment deposition would be influenced by ice for up to 60,000 years after deglaciation, due to peripheral ice bulges (Hoffman at al., 2017). As long as the ice bulges remain, there would be continuous addition of freshwater and deposition of dust and volcanic ash from atop the ice through cracks.

Fig. 1. *All of Scotland, parts of England, and Northern Ireland (in yellow) were situated on the southeastern margin of Laurentia (left). The location of the study area on Islay is marked with a red star. The geography of southern Laurentia and the included parts of the UK and Ireland is re-drawn from a map by Cocks et al. (2011).*

Both the BDF and the PAF are part of the Argyll Group of the Dalradian Supergroup (Roberts & Treagus, 1979; Rugen et al., 2024). The BDF is approximately 300 m thick (Spencer & Spencer, 1972), and since it directly overlies the PAF, it provides an ideal setting for studying paleoclimate in extreme post-glacial conditions.

The study area is located on the north shore of Islay, NW Scotland. At the time of deposition of the BDF, Islay was part of southeastern Laurentia (Dalziel & Soper, 2001) (Cocks et al., 2011) (Fig. 1). Paleolatitudes shifted from approximately 30° south of the equator at the onset of the Sturtian to somewhere in between 30-40° south of the equator during deposition of the BDF (Li et al., 2008) (Fig. 2).

The terminal deglaciation deposits of the PAF are represented by thinning diamictite horizons and thick, non-glacial sandstones, which are interpreted as deltaic and shallow marine deposits. Within this deglaciation sequence, depositional age constraints have been established through zircon dating, yielding an age of 662.7 ± 7.8 Ma (Rugen et al., 2024). Whether the BDF should be ascribed to the Sturtian or Marinoan Snowball Earth deglaciations has been debated. Re–Os dating of beds underlying the PAF and overlying the BDF suggests a Marinoan age. However, comparison with dating from other formations in the Argyll Group implies that these results reflect diagenesis rather than deposition. The PAF includes banded iron formations, which are considered characteristic of the Sturtian Snowball glaciation. Additionally, on Islay, the PAF directly overlies the Lossit Limestone Formation, which contains molar-tooth calcite—a feature linked to the Tonian (1000–720 Ma). Units underlying the PAF on Garbh Eileach Island (northeast of Islay) display Sr- and C-isotopic values matching those of the Tonian ocean (Rugen et al., 2024) (Fairchild et al., 2018) (Rooney et al., 2011).

Typical of Cryogenian events, glacial deposits are often overlain by 3–30 m of cap carbonates—continuous beds of limestone and/or dolostone deposited on continental platforms, shelves, and slopes. Most Marinoan cap carbonates begin with cap dolostones, while Sturtian cap carbonates, if present, tend to be micritic, organic-rich limestones. Marinoan cap carbonates record a long transgressive period, with continuous flooding of continental shelves due to ice melting and ocean warming. In contrast, Sturtian cap carbonates primarily reflect the stage of maximum sea level, when the ocean had reached its greatest extent. The prolonged flooding associated with post-Marinoan cap carbonates includes giant wave ripples, seafloor barite, and aragonite fans from the transgressive stage. These features are usually minor or absent in post-Sturtian sequences (Rugen et al., 2024). The lowermost member of the BDF (Member 1) consists of psammitic and pelitic beds, sometimes partly dolomitic.

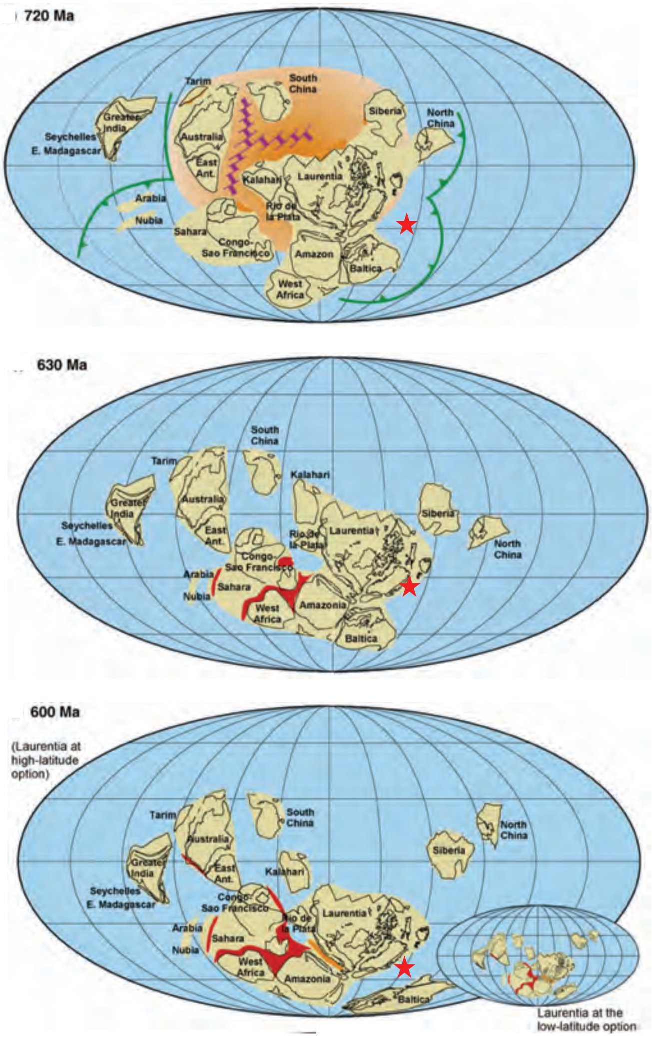

Fig. 2. *Paleotectonic overview from Li et al. (2008), with the lowermost globe showing two alternative paleolatitudes suggested for Laurentia at 600 Ma. Laurentia shows a continuous southward drift from the onset of the Sturtian through the Marinoan, Red star marks the position of the BDF (Cocks et al., 2011).*

Dolomite formation is favored in shallow waters with a high Mg/Ca ratio, mean annual surface temperatures above 22 °C, and seasonal temperatures ranging from 35 °C to 55 °C (Spencer & Spencer, 1972). Today, dolomite is primarily found in aquatic evaporitic environments with marine-anoxic, organic-rich sediments, dominated by bacterial sulphate reduction. Primary dolomite precipitates directly from water, while secondary dolomite forms through the dolomitization of limestone (Warren, 2016). Research in the Red Sea indicates that primary dolomite forms only when gypsum or anhydrite is also present (Friedman, 1980). Dolostone composed of primary dolomite and significant amounts of detrital material reflects slow formation, as the dolomite is diluted by terrestrial input. If detrital material is minor, faster precipitation from oversaturated Mg/Ca water is inferred, suggesting high weathering rates that release Mg and Ca ions (Warren, 2016) (Rugen et al., 2024).

The presence of microbial mats and stromatolites in dolomitic strata not only supports the idea of warm, shallow conditions, but also suggests precipitation of dolomite by sulphate-reducing bacteria. The presence of organic matter and anaerobic conditions lead to the formation of sulfides, as pyrite. In arid and warm climates, dolomite is associated with capillary-precipitated evaporites and the growth of anhydrite nodules. This phenomenon is observed today in ephemeral saline waters of intertidal and supratidal environments, such as sabkhas (evaporitic mudflats) and saline pans, primarily at latitudes between 25° and 35°. Sabkhas and saline pans at higher latitudes, such as Corong in Australia (36° south of the equator), differ from those at lower latitudes, as the nightly and seasonal temperatures are too cold to preserve anhydrite. Modern coastal sabkhas hosting microbial mats, dolomite, and evaporites—including preserved anhydrite—are well documented in the Persian Gulf (Warren, 2016).

Geologic fluids percolating through sedimentary rocks cause re-equilibration, where original minerals are replaced. This includes dissolution–precipitation reactions, resulting in the formation of pseudomorphs. Evaporitic pseudomorphs can be identified based on the shape and mineralogy of their rims and interiors. Replacement starts at the edges of the original mineral and continues inward, facilitated by cracks and porosity (Betkowski et al., 2016).

Typically, gypsum and anhydrite pseudomorphs contain a rugose rim of quartz and pyrite—sometimes calcite—and an interior with megaquartz, carbonates, and pyrite. Depending on brine chemistry, other minerals such as baryte and celestite also replace evaporites. The original mineralogy is typically best preserved in the center of the pseudomorph, sometimes as inclusions in megaquartz. If dissolution exceeds precipitation, an empty void is formed. This allows formation of a pseudomorph lacking a rim, while still preserving the shape of the precursor mineral. Within the void, minerals grow relatively freely (Warren, 2016).

Due to the Grampian Orogeny (470–460 Ma), the BDF has undergone regional greenschist facies metamorphism, classified as chlorite grade (Harte & Graham, 1975). Low-grade metamorphosed rocks may still retain evidence of depositional paleoclimate. Evaporitic pseudomorphs, inclusions of evaporitic minerals preserved in quartz, lithified microbial mats, and stromatolites are examples of paleoclimate indicators of warm, arid conditions at the time of deposition (Warren, 2016).

The aim of this study is to identify and interpret paleoclimate indicators preserved in Member 3 of the BDF. These findings are used to reconstruct aspects of the paleoclimate and assess their relevance in the context of the Snowball Earth hypothesis. Samples were collected during a six-day field study and analysed using polarising microscopy, scanning electron microscopy (SEM), and Raman spectroscopy.

1.1 Characteristics of Deposition in the Capillary Zone

Primary evaporites precipitate from a saturated surface or near-surface brine, where evaporation is driven by solar radiation. Brines responsible for evaporite precipitation can originate from resurging groundwater, marine, and/or meteoric water. For evaporite deposition to occur, the influx of undersaturated meteoric and marine waters must be limited. The sequence of evaporite mineral precipitation follows solubility trends. The first minerals to precipitate from evaporating brines are alkaline earth carbonates: dolomite ($CaMg(CO_3)_2$), calcite ($CaCO_3$), and aragonite ($CaCO_3$). The specific carbonate that precipitates depends on the Mg/Ca ratio of the brine. As evaporation proceeds, the least soluble evaporite salts, gypsum ($CaSO_4 \cdot 2H_2O$) and anhydrite ($CaSO_4$), precipitate. These are followed by highly soluble evaporites such as halite (NaCl) and glauberite ($Na_2Ca(SO_4)_2$). In the final stages of evaporation, depending on the availability of ions, bittern salts may precipitate (Warren, 1997).

Identifying the brine source often requires isotopic measurements, but one diagnostic feature provides insight — the presence of intrasedimentary evaporites or their pseudomorphs. Intrasedimentary evaporites can only form from resurging groundwater within the capillary zone. There are several evaporitic environments partly influenced by capillary brines, but only one in which capillary activity is dominant. Identifying capillary action as the primary control on evaporitic deposition directly points to a sabkha — an evaporitic mudflat where lithologies are primarily controlled by the ionic composition of groundwater. In some scientific literature, the term "playa" is used to describe sabkhas, but a playa is actually a broader term that includes various hydrological settings (Warren, 2016).

At depths greater than one meter below the surface of a sabkha, evaporation rates are insufficient for evaporite precipitation. Retrograde (thermalite) salts can form deeper within the sabkha, due to temperature changes in the capillary brine as it moves upward and downward. Thermalites are diagenetic evaporites and commonly appear as anhydrite nodules (Warren, 2016).

The influx of marine and meteoric water at the surface of the sabkha does not affect the chemistry of the capillary brine, due to pore pressure retaining the capillary brine within pore spaces above the capillary fringe, hindering meteoric and marine water to percolate downwards. The chemistry of capillary brines may still reflect both surrounding lithologies and ocean water chemistry, due to subsurface lateral inflow of continental and marine waters to the brine (Warren, 2016).

Capillary-driven cycles and brine chemistry govern dissolution, precipitation, oxygen transport, and matrix recrystallization. In high-Mg^{2+} evaporitic environments, phreatic mud is commonly recrystallized into dolomite, illustrating the interplay between brine chemistry and diagenetic processes in capillary zone deposits. The height of capillary rise through various sediments is summarized in Table 1 (Warren, 2016).

Sediment	Grain size (mm)	Capillary rise (cm)
Coarse sand	0.5	15
Medium sand	0.3	25
Fine sand	0.15	50
Very fine sand	0.075	100
Coarse silt	0.025	300
Fine silt	0.008	750
Coarse clay	0.002	3750
Fine clay	0.0002	37500

Table 1. *Capacity of capillary rise through various sediments (Warren (2016).*

A sabkha contain up to 30–50% intrasedimentary evaporites in a matrix dominated by phreatic mud and carbonates. When capillary brines reach the surface, a crust forms on the sabkha. These crusts are rarely preserved, as they are often flushed away by groundwater and marine and/or meteoric waters. Depressions in the sabkha, where the capillary fringe remains more permanently exposed, are termed saline pans (Warren, 2016).

A sabkha can be either continental or near-marine. In the latter case, the sabkha forms a narrow belt in the supratidal zone and is typically flooded periodically by marine and meteoric waters. This leads to schizohaline conditions and the dissolution of salt crusts at the sabkha surface. Gypsum is common in both continental and near-marine sabkhas, while anhydrite is also present, but to a lesser extent. Glauberite is more likely to be found in continental sabkhas (Warren, 2016).

Near-marine and continental sabkha types can transition laterally into one another. Modern sabkhas typically receive very little rainfall and therefore exhibit minimal terrestrial input (Loughland et al., 2016). The presence of sulphate-reducing microbialites also affects brine chemistry and leads to the dissolution of sulphates, releasing ions that are incorporated into and redistributed by the capillary brine (Warren, 2016) (Rosen, 2000).

Characteristics of intrasedimentary evaporites

Recognizing intrasedimentary evaporites involves identifying key characteristics. These features are often preserved even after pseudomorphism (Warren, 2016) (Rosen, 2000):

- **Vertical orientation:** Caused by the vertical movement of resurging groundwater and faster crystal growth along the direction of minimal stress (toward the surface).
- **Irregular placement:** Dependent on available pore space, resulting in an irregular distribution.
- **Displacive growth:** Crystals push surrounding sediments aside as they form, causing sediment realignment around the evaporite

.- **Variations in size:** Crystal growth is controlled by the availability of pore space.
- **Clustered morphology:** Nucleation sites within a matrix are rarer than on the surface, resulting in multiple crystals growing from a single nucleation site.

Characteristics of evaporites precipitated at the surface/brine or air/brine interface

When the capillary fringe reaches the surface, evaporites can precipitate directly on the surface or at the air/brine interface. Air/brine interface precipitates sink and form cumulates at the bottom of the brine. Surface/brine precipitation is recognized by evaporites or their pseudomorphs aligning along a horizontal plane. Surface growth of lenticular evaporite crystals, such as gypsum, typically form within cracks, conforming to their crystal habit (Warren, 1997) (Warren, 2016).

Over time, surface and air/brine precipitates may coalesce into evaporite beds, typically ranging from millimetres to metres in thickness. Flushing by meteoric and/or marine water commonly leads to their dissolution, often followed by replacement forming well-cemented siliciclastic beds. If the water influx is of continental origin, the siliciclastic bed will include detrital minerals derived from the surrounding terrain. In the rock record, schizohaline conditions may be indicated by lithified haloturbated (highly disturbed siliciclastics) structures, teepees, and breccias (Warren, 1997) (Warren, 2016).

1.2 Recognizing Evaporitic Pseudomorphs

All evaporites eventually undergo dissolution and replacement. This process is driven by sulphate-reducing microbial activity, groundwater interaction, hydrothermal fluids and/or influx of meteoric and/or marine water. Ancient calcium sulphates as gypsum and anhydrite, and sodium-calcium sulphates such as glauberite are therefore preserved as pseudomorphs in the rock record (Warren, 2016). In the capillary zone, capillary brines control precipitation, dissolution and replacement of evaporites within the sabkha.

The classification of an evaporitic pseudomorph depends on diagnostic features such as characteristic crystal shapes (Fig. 6–8) and the mineralogical composition of the replacement phases. While pseudomorphs of evaporites do not necessarily indicate metamorphism, metamorphic processes can alter their orientation and composition (Warren, 1997) (Warren, 2016) (Rosen, 2000), leading to formation of metamorphic minerals within pseudomorphs.

Formation of a Rim

Evaporitic pseudomorphs can form through various processes. In the early stages of replacement, if dissolution does not outpace mineral precipitation, a microcrystalline quartz (SiO_2) rim forms around the edge of the evaporite, preserving its shape. As sulphate dissolves, it is diffused and reduced to hydrogen sulfide (H_2S). In iron-rich brines, H_2S reacts with Fe, resulting in pyrite (FeS_2) nucleation within the quartz rim. Replacement progresses inward through cracks and fissures. The vacant space left by the dissolved sulphate allows early replacement minerals to grow freely within the pseudomorph interior (Warren, 1997) (Warren, 2016) (Rosen, 1990).

If dissolution exceeds replacement, the pseudomorph does not develop a rugose quartz–pyrite rim. Instead, an empty vug is left behind, preserving the shape of the dissolved evaporite. Fast dissolution is often associated with liquefaction, microbial activity, or the influx of marine and/or meteoric water at the surface. As meteoric and marine surface water cannot percolate down into the capillary brine (Warren, 2016), they can only dissolve evaporites at surface level. Evaporitic pseudomorphs formed through rapid dissolution may either lack a rim entirely or have a thin or partial rim composed primarily of quartz. If this occurs at the very surface, multiple detrital minerals may fill the open vug left by the dissolved evaporite. At any depth below surface level, within the capillary zone, these voids are instead filled by minerals precipitated from the capillary brine (Warren, 1997).

The interior of an evaporitic pseudomorph

The presence of alkaline earth minerals in evaporitic lithologies leads to dolomite and calcite commonly occurring as replacement minerals within evaporitic pseudomorphs. Influxes of fluids carrying Ba^{2+} or Sr^{2+} may facilitate replacement by baryte ($BaSO_4$) or celestite ($SrSO_4$) (Warren, 2016. If crystal growth dominates over nucleation, a sparry cement forms; conversely, if nucleation dominates, micritic cement fills the pseudomorph. Crystal growth and nucleation rates are controlled by available pore space and the rate of precipitation (Warren, 2016).

Remnants of the evaporite precursor, if present, are most likely to be found within the pseudomorph interior. These remnants are commonly preserved as inclusions, typically within megaquartz, but occasionally in carbonates. Since anhydrite is the anhydrous form of gypsum and water is released during replacement and burial, pseudomorphs with gypsum precursors often contain anhydrite inclusions (Warren, 2016). Since replacement minerals in most evaporitic pseudomorphs are similar, shape remains a key diagnostic feature for distinguishing between them. Additionally, specific shapes are characteristic of different depositional environments (Warren, 2016).

In anoxic conditions with a very high concentration of organic material, sulfur and reactive iron can lead to complete pyritization of gypsum. This may also be linked to low-grade metamorphism. where elevated temperatures and pressures enhance the mobility of iron and sulfur, favoring complete pyritization. Such replacement is documented by Hall (1982) in the Ballachulish Slate in Scotland.

Replacement of evaporites by silica, pyrite, and carbonates can occur at any point in the burial cycle. Dissolved atmospheric CO_2 yields bicarbonate-rich waters, which dissolve sulphates. Sulphate-reducing bacteria and flushing by waters undersaturated in evaporite salts and oversaturated with $CaCO_3$ can also lead to sulphate dissolution (Warren, 2016).

Shapes of Gypsum

Intrasedimentary gypsum typically exhibits tabular, hemi-pyramidal, or selenite disc morphologies, referred to as birdbeak gypsum (Fig. 3). Birdbeak gypsum is characterized by its distinct hooked endings (Fig. 3B and E). The termination of multiple lenticular gypsum crystals results in a fringed appearance along the edges of gypsum pseudomorphs (Fig. 3D) (Hanor, 2000) (Warren, 2016).

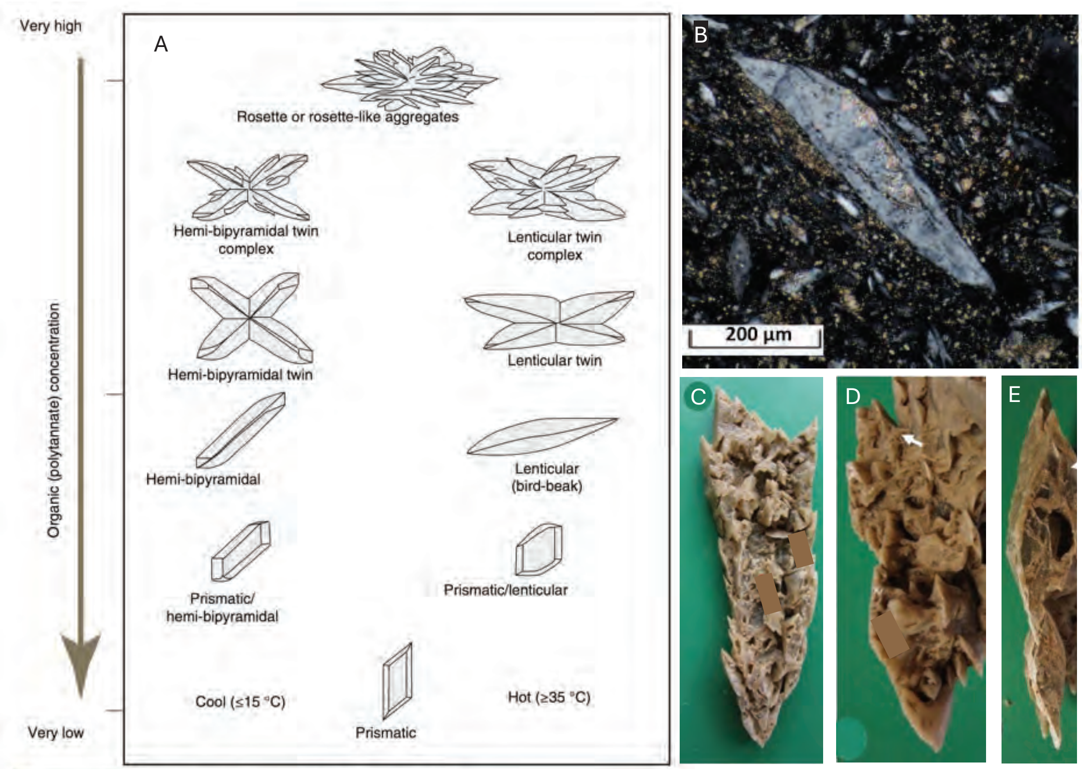

Fig. 3. *Typical gypsum morphologies. A) Hemi-bipyramidal, lenticular, and prismatic forms, influenced by organic content and temperature (Warren, 2016). B) Lenticular birdbeak gypsum with hooked endings in thin section, XPL (Schreiber, 2014). C) Twinned arrowhead gypsum, a typically subaqueous texture. D) Fringed terminations formed by multiple lenticular crystals (white arrow). E) Intergrown birdbeak gypsum. Images C–E adapted from Aref & Mannaa (2021).*

Lenticular birdbeak gypsum, whether single or twinned, is indicative of temperatures ≥35 °C, whereas hemi-bipyramidal gypsum forms at temperatures ≤15 °C (Fig. 3A) (Warren, 2016). Subaqueously precipitated gypsum typically exhibits twinned "arrowhead" shapes (Fig. 3C) (Schreiber, 2014), grass-like growth, swallowtail structures, and palmate crystals (Warren, 2016).

Gypsum pseudomorphs share morphological similarities with ikaite pseudomorphs. The presence of ikaite pseudomorphs indicates an arctic climate, while gypsum pseudomorphs suggest a warm, at least periodically arid, depositional environment. In contrast to what has been described about gypsum pseudomorphs, ikaite pseudomorphs commonly display a granular structure composed of rounded, sand-sized calcite grains in a mix of spherulitic and sparry cements (Warren, 2016).

When gypsum is buried and temperatures reach 50–60 °C, it converts to nodular anhydrite (Fig. 4). This may occur at just a few meters depth. If near-surface pore-fluid salinity reaches halite saturation, the conversion may begin at approximately 35–45 °C.

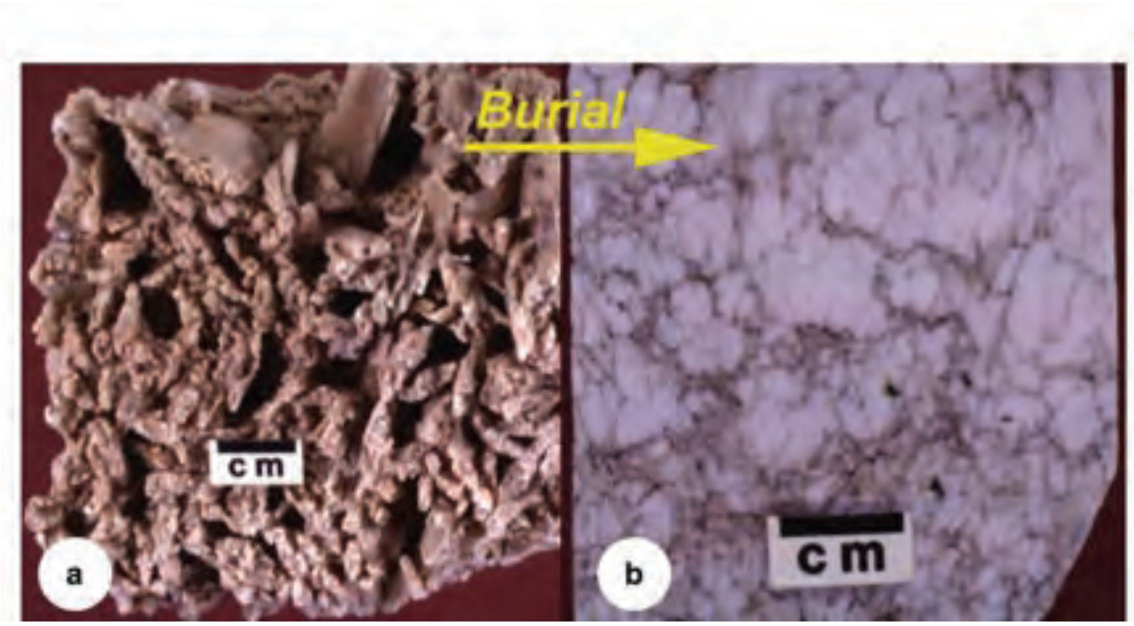

Fig. 4. *Conversion of gypsum to nodular anhydrite. Figure from Warren (2016).*

Shapes of Anhydrite

Like gypsum, anhydrite also displays lenticular crystal habit, but with distinct keg-barrel or axe-head shapes (5D, E). Both varieties lack the hooked terminations typical of birdbeak gypsum (Warren, 2016). Anhydrite may also form cauliflower-shaped nodules (typically mm to cm in size), often associated with dolomitization of carbonate mud. This process releases Ca^{2+}. If SO_4^{2-} is present, intrasedimentary cauliflower-shaped anhydrite nodules may precipitate (Warren, 2016).

At modern Earth surface temperatures, anhydrite does not precipitate directly from aqueous solutions. Near the surface of a modern sabkha, anhydrite forms through the dehydration of gypsum (Hardie, 1978). During this process, a mass of tiny anhydrite laths develops, releasing water. This anhydrite texture is easily deformed by the weight of the overlying sediment and may produce a "chicken-wire" structure (Fig. 5A), consisting of spherical or ovoid anhydrite nodules forming a ptygmatic structure. Anhydrite nodules forming chicken-wire textures are often separated by wavy remnants of sediment, representing the matrix's original mineralogy during nodule growth (Hardie, 1978).

Deeper in the sabkha, below the capillary fringe, nodular anhydrite may also precipitate as a burial salt (thermalite). due to temperature changes or the mixing of brines differing in salinity and chemistry (Warren, 2016). Upon uplift and contact with dilute groundwater, buried anhydrite rehydrates to gypsum, transforming chicken-wire anhydrite into chicken-wire gypsum (Hardie, 1978).

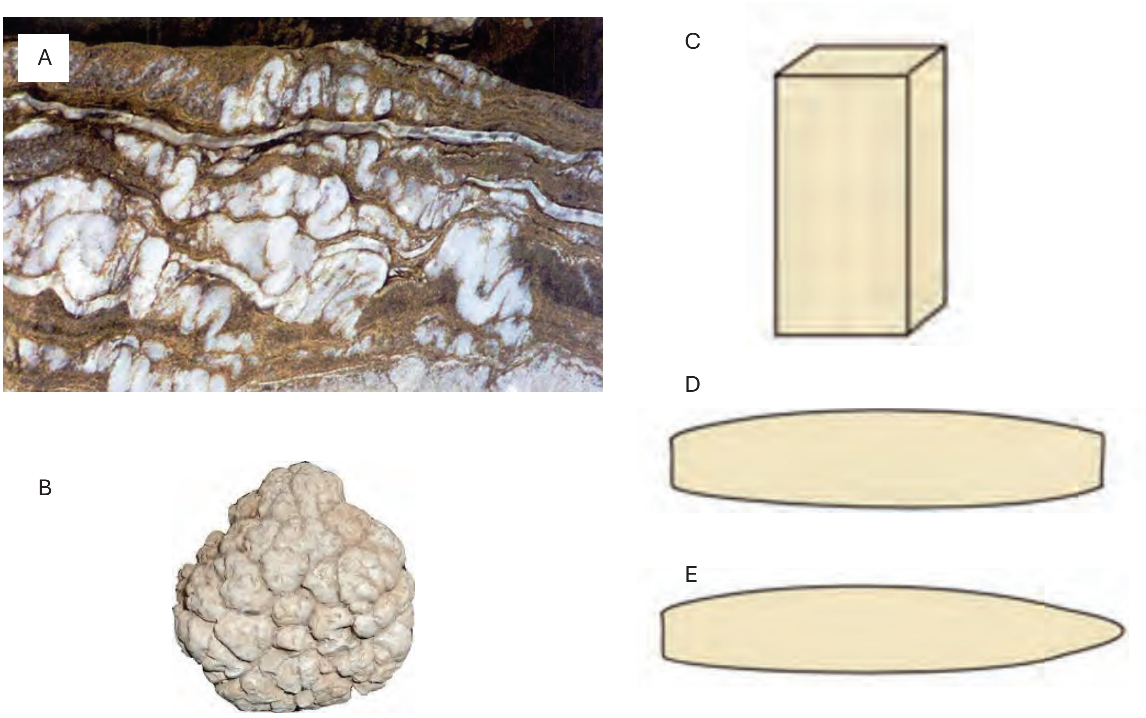

Fig. 5. *A) Chicken-wire structure, sourced from alexstreiksen.it. B) Cauliflower-shaped nodule (typically mm to cm in size). C) An anhydrite prism. D-E) Keg-barrel-shaped and axe-head-shaped anhydrite crystals, respectively. Figures B–C are adapted from Warren (2016).*

Shapes of Glauberite

Like gypsum and anhydrite, intrasedimentary glauberite can also display lenticular shapes (Figs 6 and 7). However, lenticular glauberite is generally more oval (Fig. 7A,C) and lacks the hooked terminations commonly observed in lenticular gypsum. Intrasedimentary glauberite often displays duplicate ends due to crystal twinning (Fig. 7B). Given its high solubility (Warren, 2016), glauberite is inferred unlikely to be preserved as rimmed pseudomorphs.

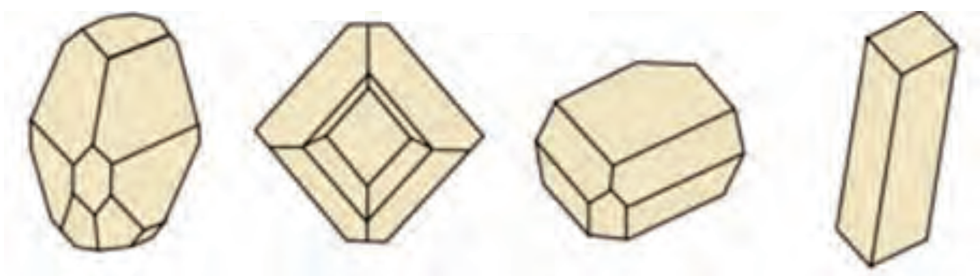

Fig. 6. *Illustration of euhedral glauberite crystal habit, adapted from Warren (2016).*

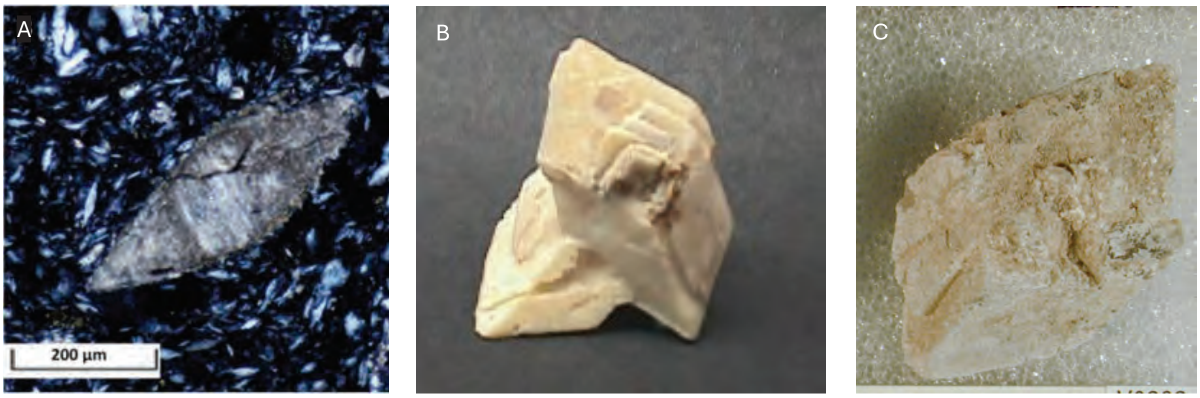

Fig. 7. *A) Thin section, XPL, showing lenticular glauberite (image from Bąbel & Schreiber, 2014). B–C) Glauberite crystals from the Vargas Gem and Mineral Collection, University of Texas.*

1.3 Differential Dissolution of Salt Beds

Bedded evaporites are highly soluble, both at the surface and in the subsurface. When an evaporitic bed dissolves later during diagenesis, it becomes more brittle and tends to form breccias. In contrast, a salt bed that dissolves during early burial—sometimes while the underlying strata are still accumulating—behaves more ductily. Lowering of the water table in the capillary zone and/or fluctuating salinities can also produce breccias in surface beds. This is typically associated with the formation of karst cones and/or teepees (Warren, 2016).

Differential dissolution refers to uneven dissolution and is caused by variations in solubility, water content, and permeability within the salt bed. If the salt bed is ductile, differential dissolution produces a sinuous curvature, appearing as continuous enterolithic intrabed slumps. Beds above and below these slumps remain undeformed, distinguishing this type of deformation from seismicity-induced slumps. The dissolving salt bed may act as a lubricant or décollement layer. If water is unable to escape, a quicksand-like consistency can develop, producing enterolithic textures with flow orientations in otherwise flat-lying, undeformed ancient salt beds (Warren, 2016) (Warren, 2017).

During burial, hydrous evaporites release structural water, which can induce liquefaction and facilitate the downward movement of overlying beds into the dissolving salt bed. A salt bed composed of varied evaporitic minerals develops intrabed asymmetry. For instance, the conversion of gypsum to anhydrite results in a 40% increase in porosity, allowing water to escape into underlying sediments and induce liquefaction. This process weakens the entire salt bed, enabling the overlying strata to subside most significantly where gypsum content was higher (Warren, 2016).

As a result of differential dissolution, irregular voids form within the salt bed, causing uneven collapse of the overlying strata. Increased pore pressure—resulting from sediment load—and storm events may also facilitate liquefaction (Warren, 2016).

As a salt bed dissolves, it leaves behind accumulations of insoluble minerals such as finely crystalline silica (termed chert), dolomite rhombs, clay, and eolian silt that were previously dispersed within the salt bed. Although silica is not an evaporitic mineral, chert accumulation is an indicator of evaporite dissolution. Chert may accumulate within pseudomorphs or remain as a residue from collapsed salt beds, filling fluid escape structures and voids (Warren, 2016).

The residual accumulation of insoluble minerals is significantly thinner than the original salt bed. A residual bed only 5 cm thick may represent a former salt bed up to 50 m thick. The insolubles are cemented by authigenic phases, typically calcite, dolomite, and silica. During diagenesis in the capillary zone, these residues are often dolomitized. Minerals from adjacent beds may also be redistributed and act as pore-filling material within the dolomitized former salt bed. Accumulations of chert and the presence of evaporitic pseudomorphs are important indicators for identifying enterolithic structures as former salt beds (Warren, 1997) (Warren, 2016).

Another structure caused by liquefaction is the formation of ball-and-pillow structures. This process is driven by variations in bulk density. It is a form of soft-sediment deformation in which chunks of clastic sediment separate from a denser overlying bed as pseudonodules which sink into a finer-grained, less dense, liquefied matrix (Fig. 8). The formation of pseudonodules is favored by a very weak underlying bed, prolonged deformation, and a large-magnitude triggering force, such as severe storms or seismic activity. Pseudonodules can drift laterally as they sink. With repeated shaking, more than one pseudonodule may separate from the same section of the overlying bed. The weight of the overlying layer can also force less dense sediment upward, forming flame structures (Owen, 1978).

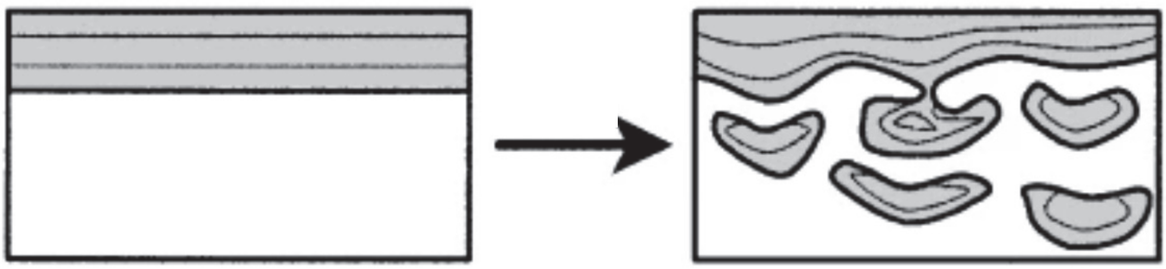

Fig. 8. *Formation of pseudonodules, which separate from an overlying, denser bed. Repeated shaking caused by storms or seismic activity can result in the detachment of multiple pseudonodules. Illustration adapted from Owen (1978).*

1.4 Implications of Storms

The transport and deposition of detrital heavy minerals and coarse quartz require water, and their abundance in lithified beds indicates high-energy conditions, typically driven by precipitation, crustal weathering, and erosion. These minerals are often deposited in low-energy settings such as alluvial fans, deltas, and estuaries (Church, 1997) (Dill, 1998), making heavy mineral-rich beds indicators of storm events.

Some alteration textures further indicate accumulations of detrital minerals. One example is leucoxene, an alteration product of Ti-bearing minerals. Leucoxene found in sedimentary rocks indicate extensive weathering and water transport. It forms in water at the surface, for instance by leaching of Fe from ilmenite, resulting in formation of pseudorutile (Mücke & Chaudhuri, 1991). Multiphase textures, as fluorapatite/carbonate is another indicator of accumulating detrital minerals, where mineralization occur at the sediment/water interface. Fluorapatite and carbonates share similar surface properties due to the presence of Ca^{2+} ions (Yi et al., 2013).

Major storms can alse be inferred from lithified giant ripples. In the geological record, such ripples are common in Neoproterozoic strata, indicating intense storm activity. Today, lithified giant ripples form in environments impacted by monsoons, tsunamis, or seismic events (Zhongwu et al., 2012).

1.5 Implications of the Presence of Baryte and Celestite

At temperatures as low as 25 °C, baryte and celestite form a solid solution series, $(Ba,Sr)SO_4$, with baryte as the Ba-dominant and celestite as the Sr-dominant end-member. Pure end-members are rare, and classification is based on which cation predominates (Hanor, 2000).

Celestite is generally highly soluble, while baryte is redox-sensitive but stable under oxidizing conditions; its preservation indicates a lack of reducing conditions. Baryte precipitation within evaporitic pseudomorphs likely reflects sulphate dissolution driven by freshwater input carrying Ba^{2+}, rather than redox-driven processes. These beds often also contain pyrite oxidized to goethite. Ba^{2+} is preferentially precipitated over Sr^{2+}, and a high Sr/Ba ratio favours sequential baryte then celestite formation as Ba^{2+} becomes depleted (Hanor, 2000).

Both minerals typically form through mixing of Ba^{2+}/Sr^{2+}-bearing water with sulphate-rich fluids, often sourced from dissolved evaporites. While Ba^{2+} is present in seawater, its primary source is K-feldspar weathering. Due to similar ionic radii, Ba^{2+} is readily incorporated into K-feldspar.

Marine Ba^{2+} concentrations range from 0.005–0.01 ppm but can reach 0.06 ppm in anoxic or hypersaline settings (Hanor, 2001). The average crustal Ba^{2+} concentration is approximately 650 ppm (Yaroshevsky, 2006). The presence of baryte within a pseudomorph is more likely linked to the weathering of continental crust than to the influx of marine water (Hanor, 2001). In contrast, Sr^{2+} is much more abundant in seawater, with concentrations ranging between 7.7 and 8.1 ppm. Average crustal Sr^{2+} concentration is 340 ppm (Yaroshevsky, 2006). The appearance of celestite within an evaporitic pseudomorph indicates increased Sr^{2+} in the brine. The origin of Sr^{2+} may reflect surrounding lithologies or influx of marine water. Celestite is less common in the rock record than baryte and is primarily associated with hypersaline, Sr-bearing fluids. It is often found in association with gypsum and anhydrite (Hanor, 2001).

Enrichment of Sr^{2+} in calcite and dolomite may be linked to the replacement of aragonite. Sr^{2+} is more readily incorporated into the crystal lattice of aragonite than into that of dolomite or calcite. When aragonite transforms into dolomite or calcite, some of the Sr^{2+} is released into solution (Katz et al., 1972). The presence of celestite alongside Sr-enriched dolomite and/or calcite could be indicative of aragonite replacement.

1.6 Implications of the Presence of Microbialites and Stromatolites

Cyanobacterial colonies can form varied morphologies. Microbialites are commonly described as microbial mats—benthic structures that grow in very shallow water, spreading across the substrate and containing algal channels that follow the bed’s surface. Their lithification in the rock record suggests brine presence but not necessarily long-term submersion. Upon brine evaporation, mud cracks form, accumulating debris and mat fragments that become lithified as quartz-rich structures, preserving both mats and mud cracks. Such algal-bound laminates with mud cracks are forming today in strandzone sabkhas of the Persian Gulf (Warren, 2016). Ancient microbial mats are documented in both marine and continental settings (Lehn et al., 2023).

Cyanobacteria can also form domal, layered stromatolites. These structures result from the combined action of microbial growth, mineral precipitation, and sediment trapping. As colonies grow, they precipitate carbonate minerals that cement surrounding sand, preserving both external morphology and internal laminations. Eventually, the cyanobacteria colonies are buried beneath accumulating sand and die (McLoughlin, 2015).

Today, stromatolites are primarily associated with peritidal marine environments and marginal lacustrine seep facies. However, ancient stromatolites are identified in a wider range of settings, including continental freshwater lakes and deeper marine environments—likely due to higher atmospheric CO_2 concentrations in the past. Although modern stromatolites are typically domal, a wider range of forms is documented in ancient deposits. For example, columnar, club-shaped stromatolites connected at the surface are rare today but commonly occur in the geological record. The few examples of modern columnar stromatolites are associated with tidal marine channels. The presence of stromatolites indicates prolonged water coverage (Warren, 2016).

In evaporitic environments where microbialites occur, sulphate dissolution by sulphate-reducing bacteria is common (Warren, 2016). These bacteria are the primary producers of iron sulphides—most commonly pyrite—in modern sedimentary environments where Fe is present. The presence of intrasedimentary pyrite is therefore an indicator of sulphate reduction and microbial sulphate dissolution (Duverger et al., 2020).

While pyrite can form through various processes, framboidal pyrite strongly suggests biogenic precipitation and anoxic conditions. Additionally, the presence of graphite further supports past organic activity (Warren, 2016).

Metabolic activity in microbialites produces various gases. The escape of these gases can form domal structures above lithified microbial mats (Farías et al., 2014).

2. Methods

The study area covers a 420 m section of coastline along the North Shore of Islay (Fig. 1) (Fig. 9). Seven sections were selected for closer investigation. Intervening sections were not included, as they are buried under sand and/or complexly folded. The selected sections represent all visible structural and lithological variations within the study area.

The stratigraphic column is divided into three logs, which have been correlated with one another. Each log includes one or more beds, which are also correlated. The stratigraphic column was hand-drawn in the field and later digitized (see Results, Fig. 10). Stratigraphic Log 1 represents the earliest deposited and lowermost beds (sections 5, 6a, and 6b), located in the easternmost part of the study area.

Log 2 includes a single bed (section 7), missing its overlying beds. As only part of this bed is exposed, its full thickness is unknown. Its position and proximity to the lowest visible bed in Log 3 (sections 1–4) suggest that Log 2 lies just beneath Log 3. The absence of beds from Log 1 in this area prompted the placement of Log 2 above Log 1. Uncertainties are indicated in the stratigraphic column (Fig. 10).

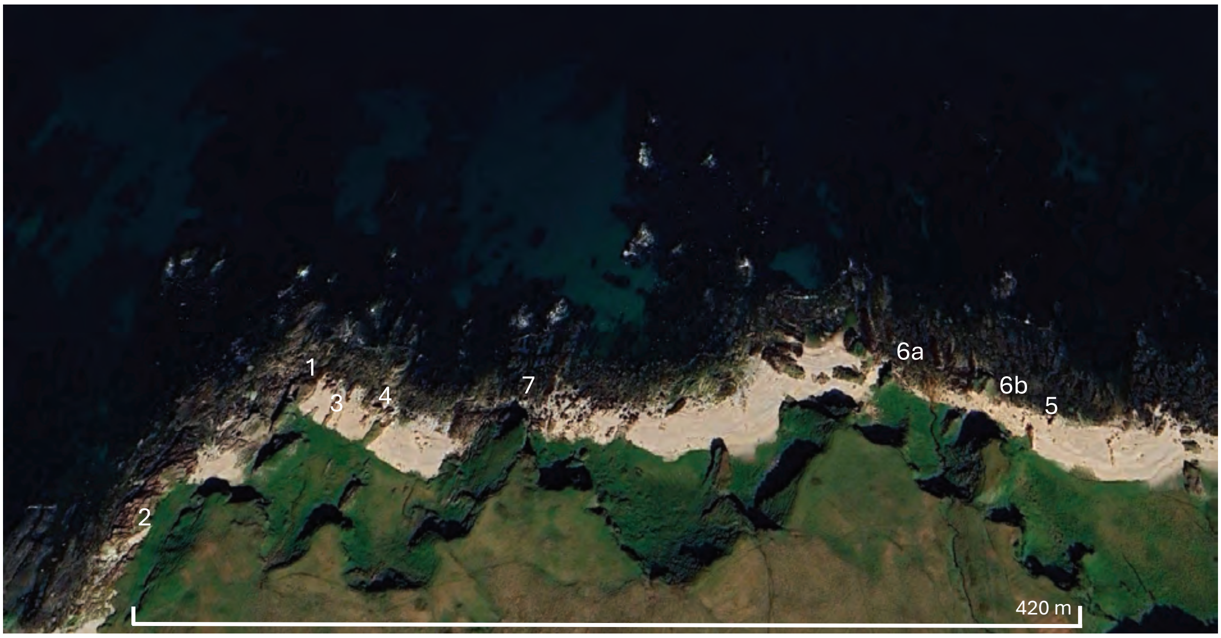

Fig. 9. *Image and scale from Google Earth (https://earth.google.com, retrieved December 2, 2024).*

All samples were taken from bedrock, which was photographed prior to collection. Samples were placed in plastic bags, labeled with a waterproof pen, and their locations were marked in the stratigraphic column while still in the field. In total, 17 beds were sampled, and 14 were analysed in thin section using a polarising microscope. Beds were typically sampled at multiple points to increase the likelihood of capturing evidence of pre-metamorphic mineralogy.

The cutting process was documented with videos and sketches to preserve orientation data and ensure that structural "way-up" indicators were retained. Most samples were cut perpendicular to bedding, except where internal structures required alternative orientations. A total of 100 chips were produced. Those most likely to contain palaeoclimate indicators were selected for thin section analysis. All thin sections were examined using both transmitted and reflected light. For beds not analysed in thin section, identification was based on field or hand sample observations of grain size and colour. For instance, samples easily cut by diamond saw were inferred to be dolomitic and/or clay-rich, whereas quartz-rich samples were harder to cut.

Six thin sections, each representing one or more distinguishing features, were further analysed using scanning electron microscopy (SEM). The SEM analysis provides weight percent (wt%) values for elements and oxides, from which minerals were identified by comparison with standard mineral formulas. The typical detection limit ranges from tens to hundreds of ppm, depending on mineral density and the calibration of the instrument (Kuisma-Kursula, 2000). The SEM cannot detect hydrogen due to its low atomic weight (Andreas Karlsson, pers. comm.).

The SEM produces a grayscale backscattered electron (BSE) image, where minerals can be distinguished by atomic density—denser minerals appear paler, with the densest appearing white.

Graphite can be difficult to identify under a polarising microscope, and is more easily distinguished using the SEM. All thin sections examined with the SEM must be coated with carbon, to provide a conductive layer on the sample surface. This inhibits charging, improves the secondary electron signal and reduces thermal damage (Leica microsystems, 2013). For the SEM to produce correct measurements of all elements but carbon, one needs to specify that the thin section is coated with carbon. When detecting a mineral with no reasonable amounts of other elements, after verifying the selected spectra point is not a hole, one needs to change the setting to ”not coated by carbon” to determine whether the mineral is graphite. By comparing the shape and optical properties of graphite identified with SEM to similar features observed in thin sections studied only with the polarising microscope, graphite was also identified in beds not analysed with SEM.

Measurements with the SEM indicated some $CaSO_4$ inclusions as having a total wt% below 70%. Raman spectroscopy was used to determine whether these inclusions contained water, as H is not detected by the SEM. With Raman spectroscopy, one can distinguish between gypsum and anhydrite. The presence of water is indicated by a characteristic peak; if this peak is absent, the mineral is interpreted as anhydrous.

Raman spectroscopy was also used to distinguish polymorphs of $CaCO_3$ and SiO_2. In Raman spectroscopy, monochromatic light (in this case, a laser) interacts with the chemical bonds of the targeted mineral. The light is scattered by the molecules, producing a spectral profile that is unique to each polymorph.

The classification of pseudomorphs is based on both morphology and mineralogy. Morphologies showing intergrown crystals are annotated to distinguish between the various crystals comprising the pseudomorph.

In the Results section, annotations of intergrown pseudomorphs are based on the pseudomorphs' terminations and internal contours defined by thin rims of quartz and/or pyrite. Multiple hooked terminations are interpreted as intergrown gypsum blades. Internal contours, often only visible at high magnification, are interpreted as remnants of individual crystals that once comprised the unified pseudomorph. In annotated images, clearly distinguishable shapes are outlined with continuous lines, while dashed lines indicate interpreted internal rims within the pseudomorph.

Images of thin sections presented in the Results section are shown right-side up, unless otherwise is indicated in specific figures.

3. Results

This section provides a detailed description of the beds included in the stratigraphic column, presented in ascending order from the basal bed. The evolution of the matrix, the classification of palaeoclimate indicators, and the corresponding thin section(s) associated with each bed are documented with reference to the digitised stratigraphic column (Fig. 10).

The matrices of the beds within the study area are primarily composed of dolomite, quartz, and micas. All dolomite examined with the SEM is ferroan, without exception. Most beds contain heavy minerals (density >2.9 g/cm^3) to some extent. These include rutile, fluorapatite, zircon, and monazite. In the uppermost beds of the stratigraphic column, the concentration of heavy minerals increases and also includes biotite.

All but one of the 14 beds examined in thin section contain evaporitic pseudomorphs. The characteristics of pseudomorphs evolve upwards in the stratigraphic column. In the lower and middle beds, the pseudomorphs exhibit distinct rugose rims of quartz and pyrite. In the upper portion of the stratigraphic column, where several rippled beds and stromatolite- or microbialite-bearing beds are present, the pseudomorphs most commonly lack distinct rims.

Lineations and tilt of the evaporitic pseudomorphs are consistent across the study area. Their orientation indicates a predominant NE–SW stretching direction during metamorphism. The influence of Grampian deformation in Member 3 of the BDF is further supported by the widespread occurrence of pyrite with strain fringes. The study area has also been structurally affected by Mesozoic faulting (Webster & Skelton, 2015) and intruded by Palaeogene dolerite dykes cutting through the strata (Fairchild, 1980).

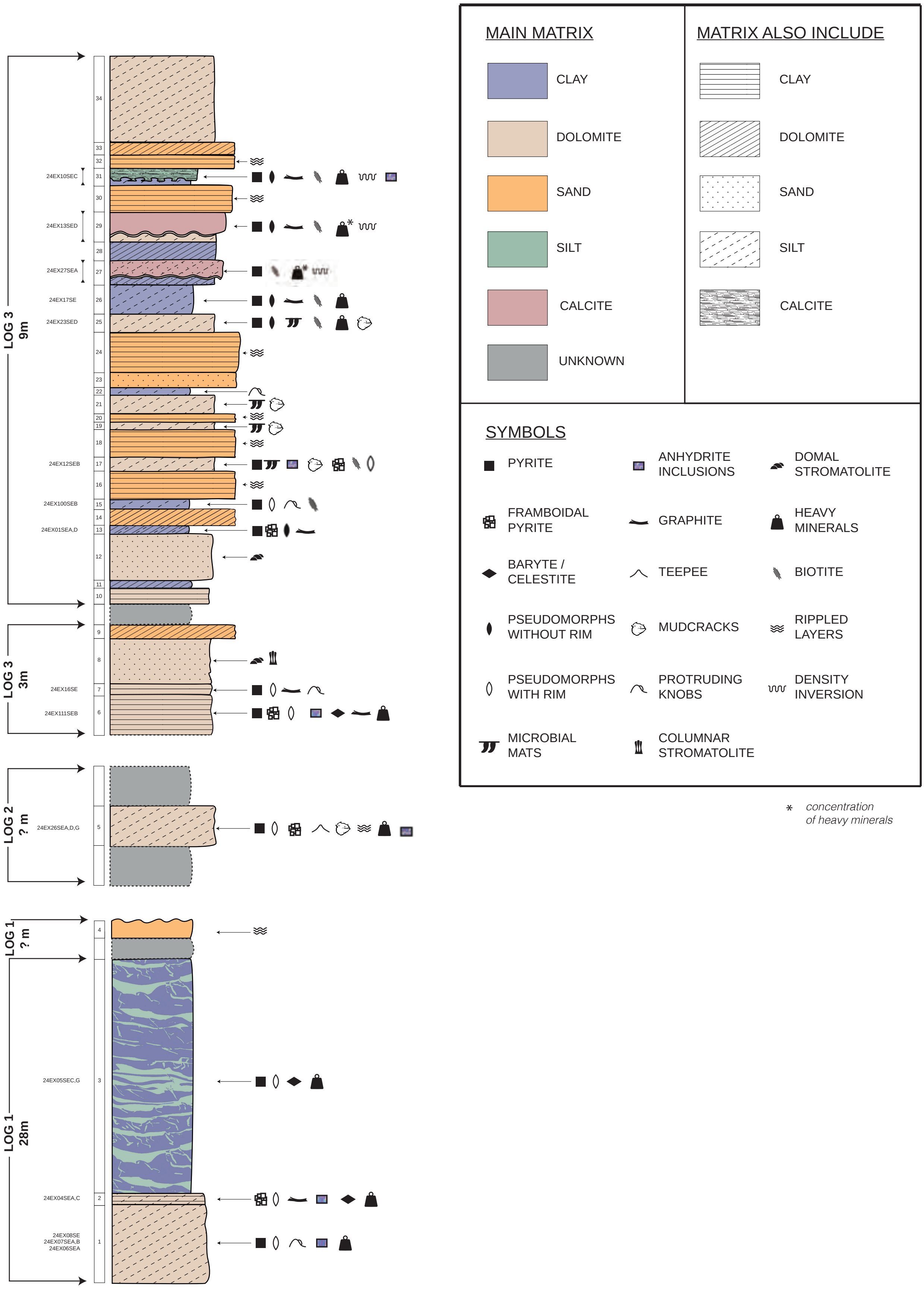

Fig. 10. *Digitised stratigraphic column and legend. The column is divided into three logs, each with a separate scale. Beds within each Log are correlated. Log 1 covers the lowermost beds. Log 2 is overlying Log 1 and consists of a single bed with unknown thickness. Log 3 includes the uppermost beds. Gaps between logs represent uncorrelated beds, buried by sand or complexly folded. Note numbering of beds (1–34). Graphics of Bed 3 are redrawn by after Spencer & Spencer (1972).*

3.1 Bed 1: Evidence of Evaporitic Precipitation Within the Capillary Zone

In the field, the lowermost bed appears pale grey and is characterised by 0.2–0.7 cm tall, protruding lenticular knobs, spaced 0.5–3 cm apart (Fig. 11A). The protruding knobs are studied in thin section 24EX07SEA, using a polarising microscope (Fig. 11B) and SEM. Additionally, this bed contains clusters of rounded, protruding nodules measuring 0.6–1.4 cm across. These are examined in thin section 24EX06SEA with polarising microscope (Fig. 13A,B).

Bed 1 is sampled at section 5 (Fig. 9). It extends approximately 14 metres beneath the portion included in the stratigraphic column. However, this lower extension is structurally disturbed due to a Mesozoic fault breccia (Webster & Skelton, 2015). Bedding within Bed 1 is predominantly vertical, except near a fold where the beds become horizontal.

Fig. 11. *A) Field image from the horizontally bedded part of section 5, where thin section 24EX07SEA was sampled. Note pen (14 cm) for scale. B) Thin section 24EX07SEA, which is 4 cm tall, XPL. Locations of anhydrite inclusions, verified using SEM, are circled in red. Zoom-in of one pseudomorph is shown in Fig. 13.*

Examination of thin section 24EX07SEA reveals that the protruding lenticular knobs are pseudomorphs with fringed terminations due to multiple blades with hooked endings (Fig. 14).

All pseudomorphs in thin section 24EX07SEA display rugose rims of quartz and pyrite. Three out of four pseudomorphs examined with the SEM contain inclusions of anhydrite preserved within megaquartz in the pseudomorph interiors (Fig. 11B, Fig. 12). These anhydrite inclusions are mostly square or rectangular, ranging from 10 to 60 µm in size. They display birefringence values between 0.042 and 0.044, consistent with the Michel-Lévy interference colours for anhydrite.

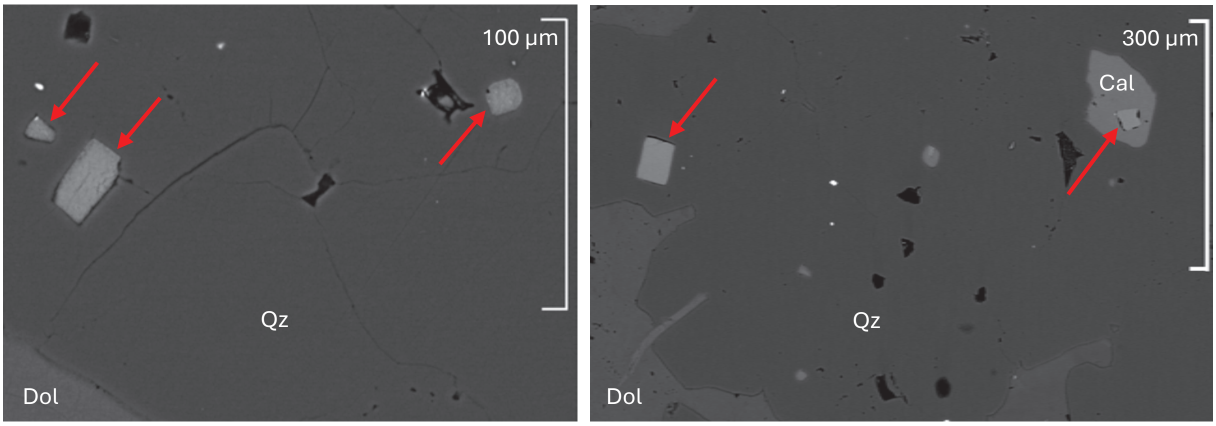

Fig. 12. *BSE images from the SEM. Anhydrite inclusions marked with red arrows. Cal = calcite, Qz = quartz, Dol = dolomite.*

Apart from megaquartz with anhydrite inclusions, the interiors of the pseudomorphs in thin section 24EX07SEA primarily consist of dolomite ($CaMg(CO_3)_2$) with minor amounts of Mg-bearing calcite ($CaCO_3$). The dolomite exhibits patchy variations in Fe content, with iron-rich areas corresponding to ankerite ($Ca(Fe,Mg,Mn)(CO_3)_2$).

The protruding, rounded nodules seen in thin section 24EX06SEA are cauliflower-shaped pseudomorphs, with some fringed terminations and rugose rims of quartz and pyrite (Fig. 13). Their interiors are filled with dolomite, quartz and pyrite. These are classified as anhydrite nodules, but the fringed terminations infers they formed from conversion from gypsum.

All pseudomorphs in thin sections 24EX06SEA and 24EX07SEA are displacive, irregularly spaced within the matrix and vary in size. The lenticular pseudomorphs with birdbeak endings display a clustered morphology. Orientation is assumed to have been vertical prior to metamorphism. These characteristics, adjoined with mineralogy and the rugose rims classify the pseudomorphs in Bed 1 as pseudomorphs of intrasedimentary precipitated gypsum (birdbeak shapes) and anhydrite (cauliflower, axe-head and keg-barrel shapes).

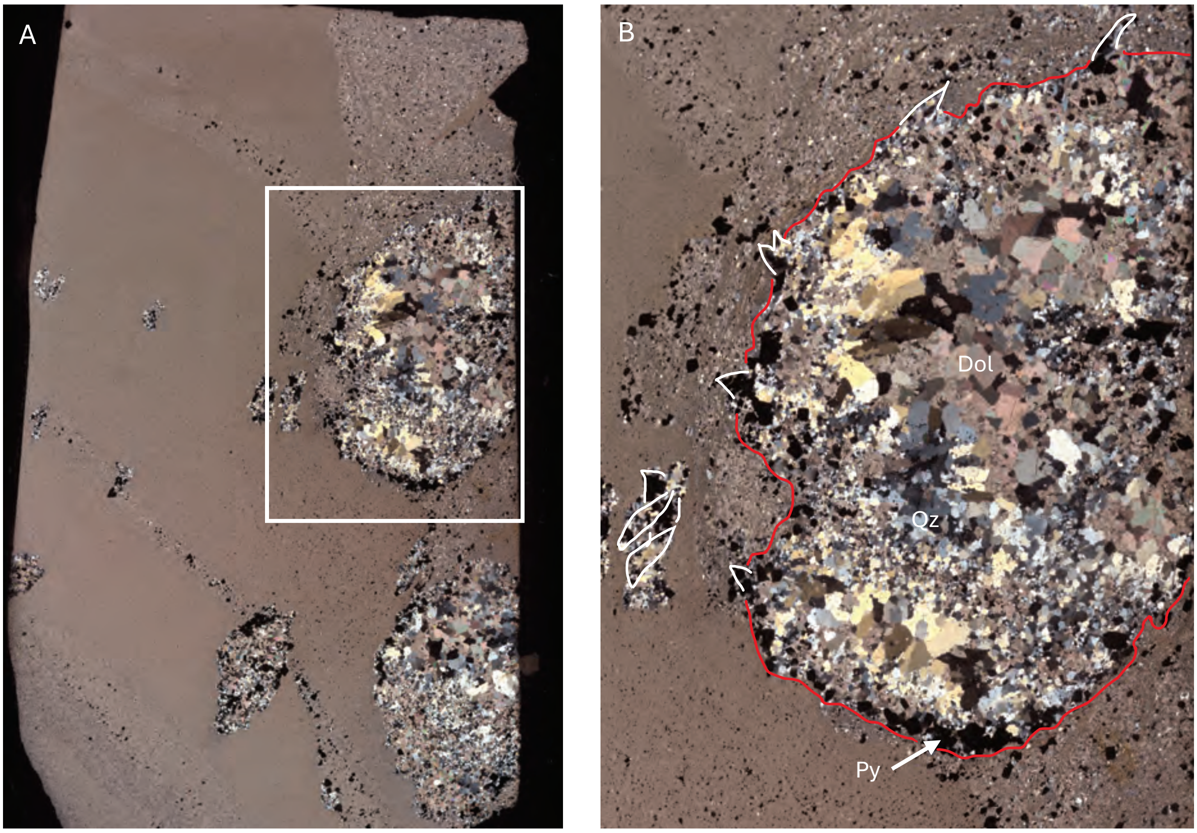

Fig. 13. *A) Thin section 24EX06SEA, which is 4 cm tall, XPL. B) Zoom in of area marked in A. Knobbly cauliflower shaped pseudomorph annotated in red. Fringed termintations marked in white. Intergrown lenticular shapes with hooked endings annotated in white. Py = pyrite, Qz = quartz, Dol = dolomite.*

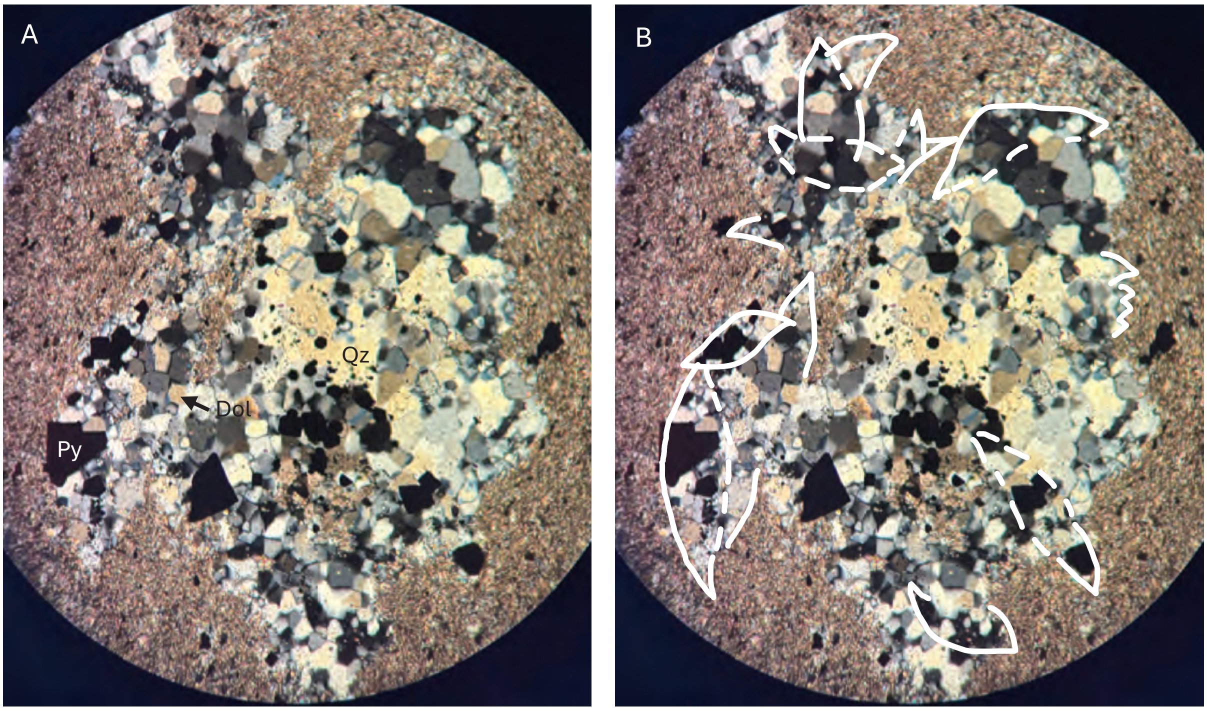

Fig. 14. *A) Close-up of pseudomorph seen in Fig. 11. B) Annotated version of A, displaying hooked endings. Dashed white lines annotate interpretations of the full crystal shape. Py = pyrite, Qz = quartz, Dol = dolomite.*

SEM analysis reveals the general matrix consist of ferroan dolomite, Nb-bearing rutile (TiO_2), fluorapatite ($Ca_5(PO_4)_3F$), and minor muscovite ($KAl_2(Si_3Al)O_{10}(OH,F)_2$). The dolomite occurs as subhedral and euhedral crystals ranging from 20 to 60 µm in size. Based on the classification of the depositional environment as the capillary zone, the matrix is interpreted to consist of dolomitized phreatic mud with detrital input of fluorapatite and rutile. All thin sections from this bed (Fig. 10) exhibit thin laminae containing abundant pyrite with strain fringes (Fig. 11B, Fig. 13A).

3.2 Bed 2: Appearance of Baryte

The next bed in the stratigraphic column was sampled at section 6b (Fig. 9). In the field, Bed 2 appears grey with pale laminae (Fig. 15). This bed was investigated in both thin sections 24EX04SEA and 24EX04SEC, with the latter examined in more detail using both SEM and polarising microscopy (Fig. 16). The pale laminae share compositional similarities with Bed 1 but exhibit greater cementation and geochemical differences in terms of elemental enrichments. SEM analysis reveals that the pale laminae in thin section 24EX04SEC contain Zr-bearing rutile, Ti-bearing muscovite, and that Mn substitutes for Mg in dolomite. Additionally, Ba-bearing K-feldspar is present in Bed 2, while absent in Bed 1. Fluorapatite occurs in the general matrix of Bed 1 and in the pale laminae of Bed 2.

Fig. 15. *A) Field image of Bed 2. Note pen (14 cm) for scale. B) Sample taken from bed 2, photographed during the cutting process.*

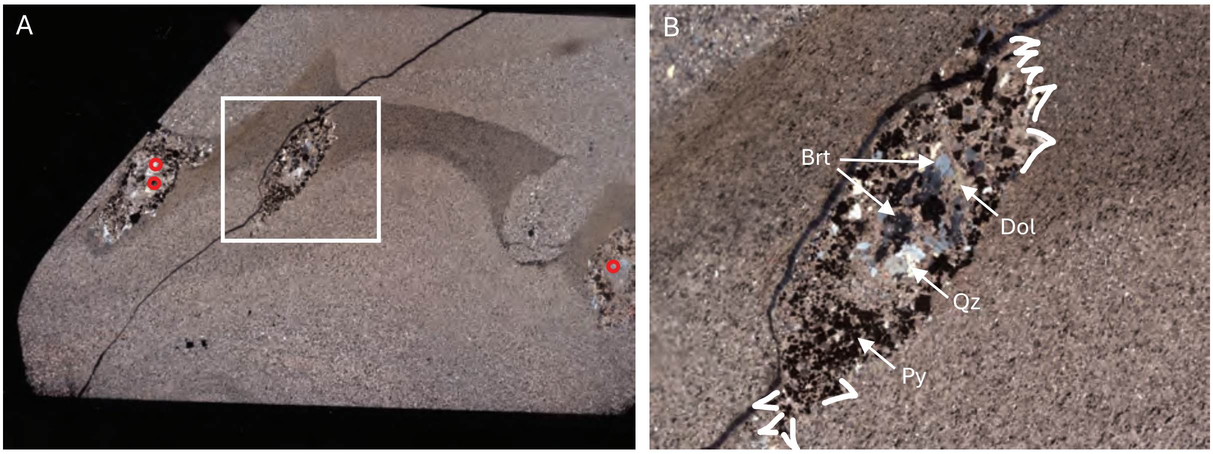

Fig. 16. *A) Scanned thin section 24EX04SEC (3.9 cm max width), XPL. Three 0.8–0.9 cm tall pseudomorphs with rugose quartz/pyrite rims and fringed terminations. The underlying matrix conforms to the pseudomorph's base. Red circles mark locations of megaquartz with anhydrite inclusions verified by SEM. All rimmed pseudomorphs contain baryte are are aligned along a dark lamina, inferred to have been horizontal before metamorphism. B) Zoom-in framed area in A. Hooked fringed terminations, typical of gypsum pseudomorphs, are marked in white. Unannotated image available in appendix 1. Brt = baryte, Dol = dolomite, Qz = quartz, Py = pyrite.*

The darker lamina in thin section 24EX04SEC consists of Ti-bearing muscovite, microcline ($KAlSi_3O_8$), kaolinite ($Al_2Si_2O_5(OH)_4$), ferroan dolomite, lineated graphite, and abundant lineated, framboidal, zoned Ti-bearing pyrite. SEM analysis shows many pyrites are intergrown with kaolinite, and rutile producing Al-rich rims and Al-poor cores and Ti-bearing pyrites respectively (Fig. 17). Pyrites not intergrown with kaolinite have Mn-enriched rims and Mn-free cores. Three pseudomorphs with rugose rims are aligned along the lamina, all featuring fringed terminations and interiors of Sr-bearing dolomite, quartz, and minor Sr-bearing calcite. All contain baryte (Fig. 17), and two include anhydrite within megaquartz (Fig. 16); both minerals are SEM-verified.

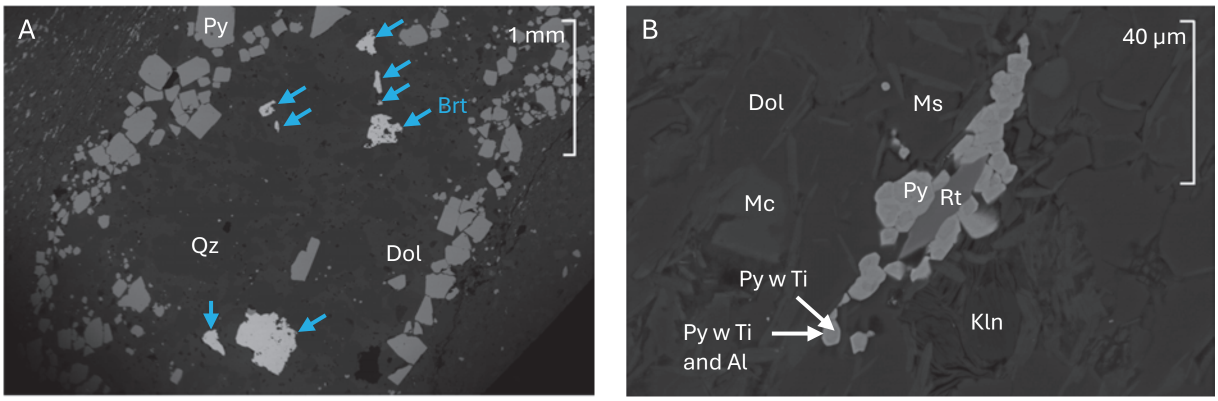

Fig. 17. *BSE images from thin section 24EX04SEC, illustrating key mineral phases. Qz = quartz, Dol = dolomite, Mc = microcline, Ms = muscovite, Kln = kaolinite, Rt = rutile, Py = pyrite, Brt = baryte. A) Baryte, marked with blue arrows, is present in all rimmed pseudomorphs. B) Rutile embedded in zoned framboidal pyrites that are intergrown with kaolinite. The pyrites exhibit Ti- and Al-bearing rims while the core lack Al. Framboidal pyrites are most abundant in the dark lamina of thin section 24EX04SEC, but also present in the pale lamina.*

Kaolinite is intergrown with framboidal pyrites in the darker lamina of thin section 24EX04SEC.

The rimmed pseudomorphs are classified as gypsum based on their fringed terminations and inclusions of anhydrite. The dark lamina has been deformed but is assumed to have been horizontal prior to metamorphism. The rimmed pseudomorphs with in v-shaped cracks, seemingly conformed to the shape of the pseudomorphs. This growth pattern suggest surface precipitation, distinguishing pseudomorphs in Bed 2 from the intrasedimentary pseudomorphs in Bed 1.

Additionally, thin section 24EX04SEC contains a 0.8 cm bulge-like structure (Fig. 16A) (Fig. 18A), which lacks a rugose quartz–pyrite rim. Polarising microscopy analysis reveal fringed and hooked terminations. Also, concentrations of framboidal pyrites outline lenticular shapes. The fringed terminations are classified as a clustered morphology of multiple gypsum blades. The bulge is filled with the same minerals as the pale matrix, classified as indicating dissolution at the surface.

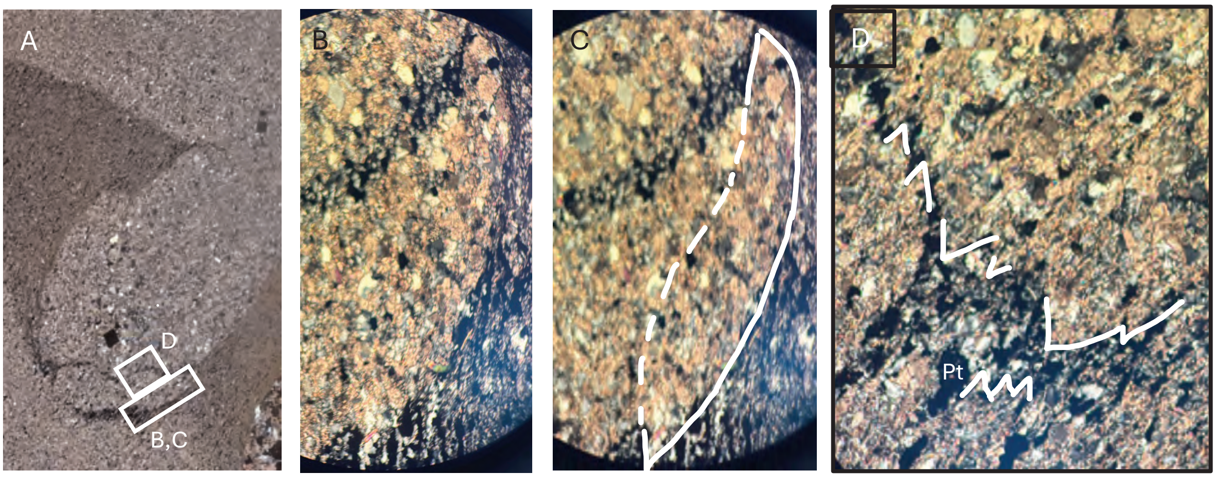

Fig. 18. *A) Bulge-like structure, lacking distinct rim apart from partial concentrations of framboidal pyrites. B) Zoom in from A, displaying a shape with hooked endings. C) Annotation of visible shape outlined in white. Assumed internal shape based on orientation of fringed terminations is marked with dashed line. D) Close up of frame marked with D in A, fringed termination indicate intergrowth of multiple crystal blades. Pt= pyrite.*

3.3 Beds 3 and 4: Highly Disturbed Siliciclastics and Giant Ripple Structures

The third stratigraphic bed is 20 m thick and displays an almost black matrix, interwoven with quartz-rich laths and protrusions extending in multiple directions (Fig. 19). The laths frequently exhibit ptygmatic shapes (Fig. 20). Disconnected quartz-rich bodies, lenticular and nodular in shape, are also present throughout the bed.

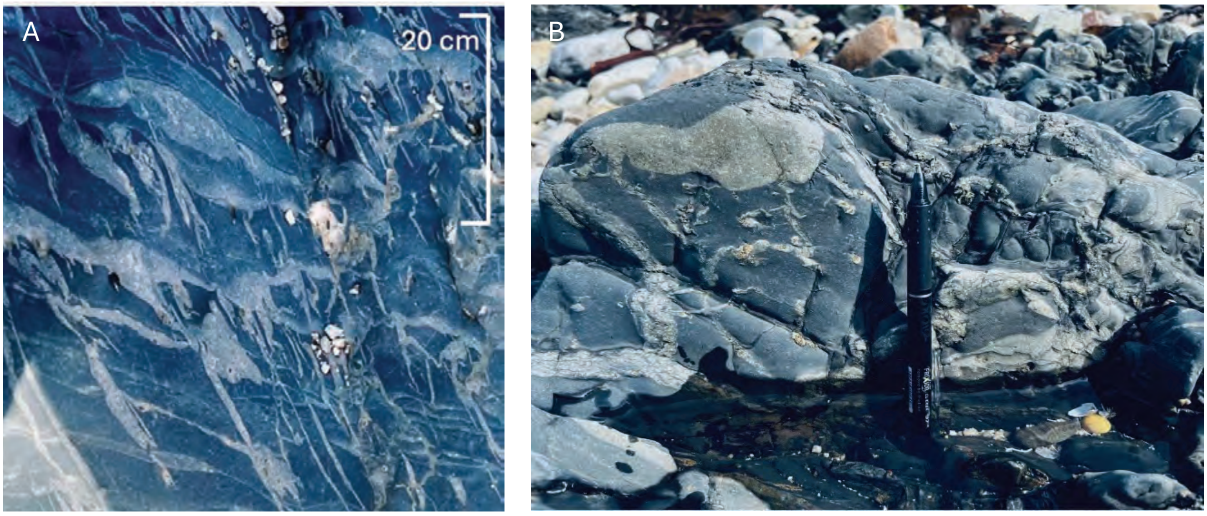

Fig. 19. A) Field image of Bed 3. Interconnected siliciclastic laths. B) Field image of Bed 3, variety of interconnected and separate siliciclastic shapes. Image is taken from a vertically bedded outcrop and the structure is seen from below. Note the pen (14 cm long) for scale.

Examination of thin sections 24EX05SEC and 24EX05SEG (Fig. 20A, B) reveals that the laths and disconnected bodies are lithified as well-cemented siliciclastics. SEM analysis of thin section 24EX05SEC confirms that these siliciclastic structures consist of relatively large, rounded quartz, Ti-bearing albite, Ba-bearing K-feldspar, fluorapatite, zircon, monazite, pyrites with goethite rims (up to 400 µm), and scarce dolomite. All minerals apart from pyrite and dolomite are classified as detrital. The main constituents of the black matrix are ferroan dolomite, Ti-bearing muscovite, albite, and relatively small pyrites (1–5 µm) with goethite rims.

Some protrusions resemble distorted mudcracks or lithified microbialites. However, most protrusions have distinct rounded forms that differ from typical mudcracks (Fig. 20, Fig. 21), appearing to widen from their point of connection to the laths (Fig. 20A). These features exhibit morphologies characteristic of gypsum, anhydrite, and possibly glauberite. Additionally, thin section 24EX05SEA and thin section 24EX05SEG contains cauliflower-shaped pseudomorphs with partly fringed terminations (Fig. 20A, D, F). Thses pseudomorph are classified as gypsum converted to anhydrite before pseudomorphism. All pseudomorphs feature rugose rims composed of quartz and pyrite, and are connected to both the dark matrix and the siliciclastic structures. They are irregularly spaced, display clustered morphology, vary in size and are displacive. These characteristics lead to a classification as pseudomorphs of intrasedimentary gypsum converted to anhydrite.

A few clusters of relatively large pyrite may represent remnants of pseudomorphs, but are excluded from classification due to strain fringes distorting their shape.

The interior of the pseudomorph in thin section 24EX05SEG consists of baryte Although the quartz-rich laths are well cemented, their thickness (up to 5 cm) is below the threshold necessary for maintaining capillary flow (Warren, 2016) (Table 1).

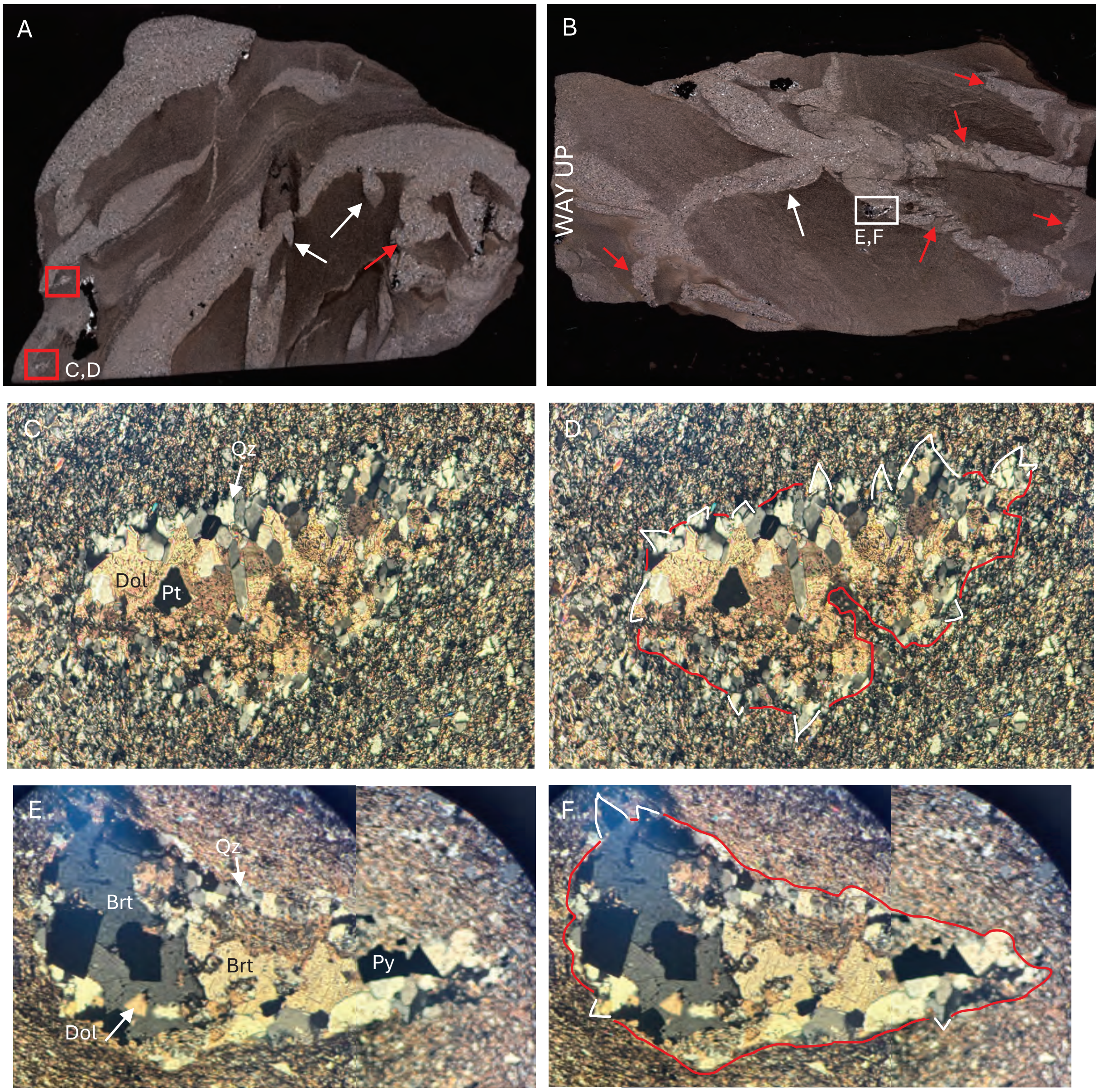

Fig. 20. A–B) Nodular pseudomorphs of anhydrite framed in red. Chicken-wire structures marked with red arrows. Protrusions considered unlikely to be distorted mudcracks marked with white arrows. A) Scanned thin section 24EX05SEC, 3.2 cm maximum width, XPL. B) Thin section 24EX05SEG, 4 cm tall, XPL. C–D) Zoom-in of frame marked C,D in A. E–F) Zoom-in of frame marked E,F in B. Pseudomorph containing baryte. Note sharp protrusions, indicating former presence of gypsum.

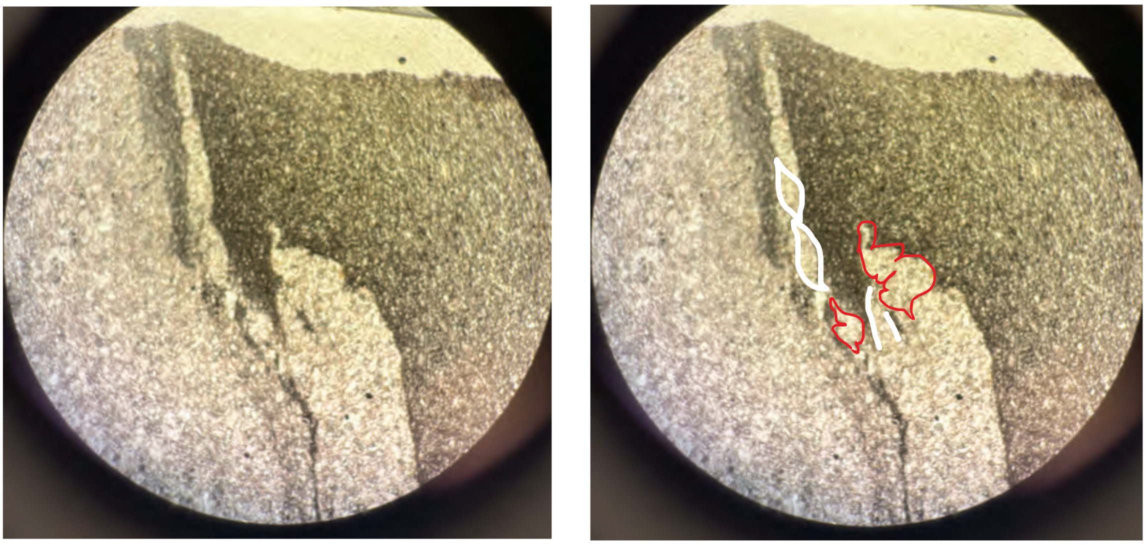

Fig. 21. *Close up of lath in thin section 24EX05SEG, PPL. Annotated lenticular shapes (white) and two chicken-wire shapes (red) classified as dissolved and replaced gypsum and anhydrite respectively.*

Overlying Bed 3 is a unit of lithified giant ripples (Fig. 22), examined only in the field and classified as being composed primarily of sand-sized quartz. Ripple heights range from 50 to 70 cm.

Fig. 22. *Bed 4, lithified giant ripples. Walking stick (130 cm tall) provides scale. Image courtesy of Anton Eriksson.*

3.4 Bed 5: Teepees, Breccia, Mudcracks, and Ripple Marks

The fifth stratigraphic bed is included in this study due to its intrabrecciated, slightly teepee-shaped structures and mudcracks (Fig. 23A). It was sampled at section 7 (Fig. 9). In the field, this bed exhibits various shades of yellowish beige. As it is nearly horizontally bedded and the overlying beds are missing, observations from above were possible. Lithified ripples are clearly visible on the surface, oriented SW/NE (Fig. 23B, C), approximately perpendicular to the NW shoreline at the time of deposition (Fairchild, 1980). This bed was analysed using a polarising microscope in thin sections 24EX26SEA, D, and G. Additionally, thin section 24EX26SED was examined with SEM.

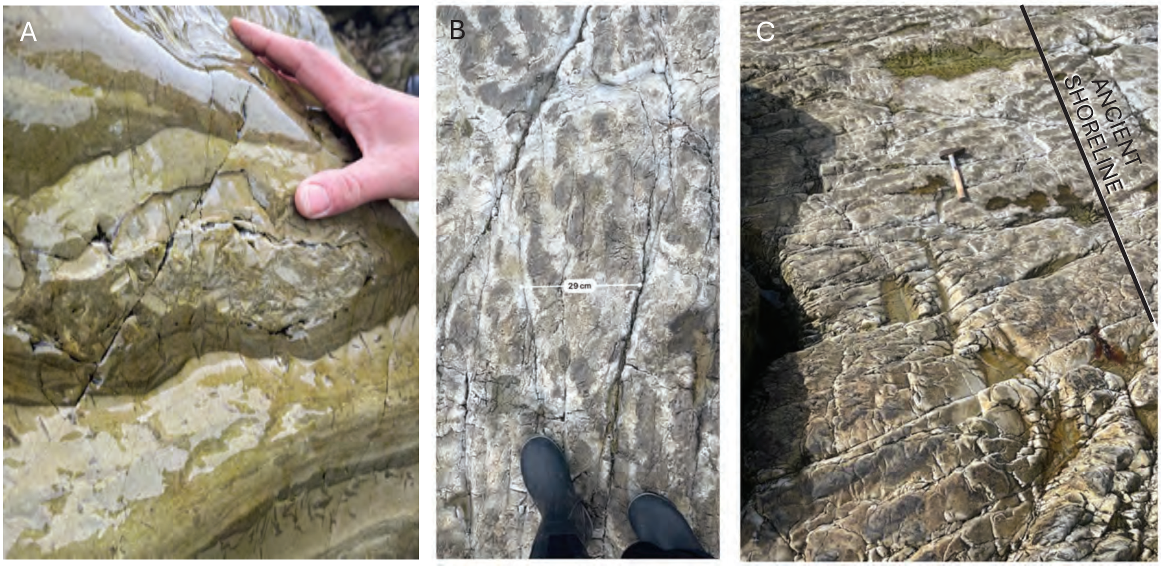

***Fig. 23**. A) Field image Bed 4. This bed is intrabrecciated and display teepee shapes and mudcracks. B-C) Bed 4 seen from above. Ripple marks indicate wave movement perpendicular to the ancient shoreline.*

Examinations with polarising microscope reveals that the brecciated clasts are quartz-rich, including both detrital (rounded and relatively large) quartz and chert. Examinations with SEM show that the quartz-rich brecciated bits also contains Ba-bearing feldspar, muscovite, and zircon. The surrounding matrix consists of approximately 90% dolomite, with minor muscovite and quartz. Elongated fragments within the breccia are partially outlined by elongated framboidal pyrite. Thin section 24EX26SEG contains nodules (Fig. 24B) filled with sparry calcite and rimmed by quartz and pyrite. Terminations of the nodules are fringed by lenticular shapes with hooked endings. The nodular pseudomorphs are classified as gypsum mostly converted to anhydrite prior to pseudomorphism. Thin section 24EX26SED contain one elongated pseudomorph, classified as intergrown gypsum discs. Its interior consist mainly of dolomicrite and quartz, some containing anhydrite and calcite inclusions. All pseudomorphs documented in Bed 5 display clustered morphology, irregular spacing and variation in size.

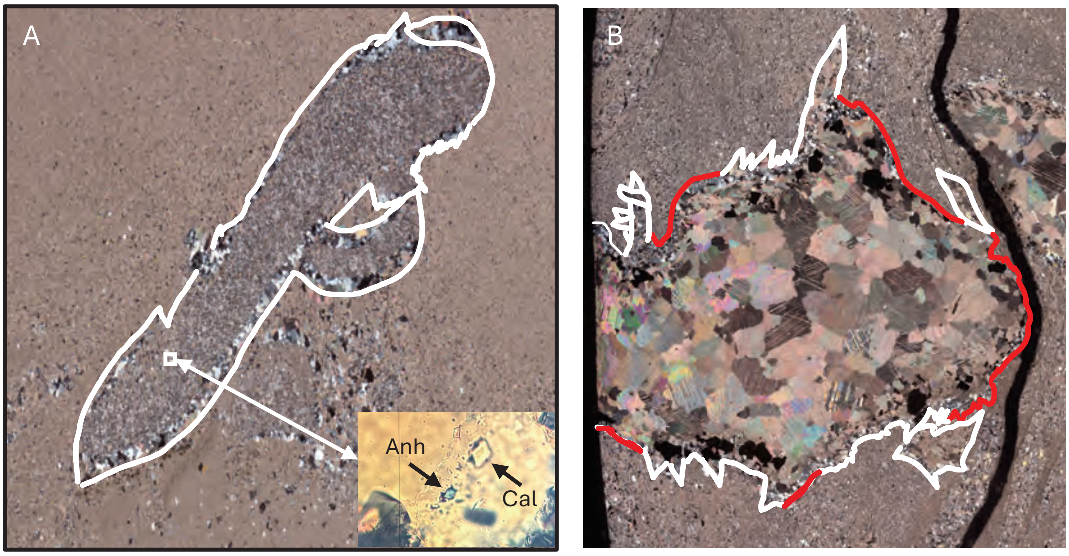

__Fig. 24__. Full thin sections, without annotations, is seen in Appendix 1. A) An 0.8 cm tall pseudomorph with partial rugose rim of quartz and pyrite, seen in thin section 24EX26SED, XPL. Quartz hold inclusions of anhydrite and calcite, identified with polarising microscope. The lack of internal rims in this pseudomorph limits possibilities to interpret internal shapes of intergrowth. B) One of the nodular pseudomorphs, 1.2 cm across, seen in thin section 24EX26SEG, XPL. Rugose rim of quartz and pyrite and fringed terminations.

3.5 Bed 6: Abundance of Anhydrite and Gypsum Pseudomorphs

The lowermost bed of section 4 (Fig. 9) is only partially exposed above the sand. It contains concentrations of densely packed, pink nodules (Fig. 25) embedded in a pale grey matrix. As only the uppermost portion of the bed is visible, its total thickness is marked unknown in the stratigraphic column (Fig. 10). Examination of thin section 24EX111SEB using a polarising microscope (Fig. 26A) and SEM reveals that the nodules possess rugose rims composed of quartz, pyrite, and baryte. The interiors of the nodules are predominantly composed of sparry calcite (Fig. 26B).

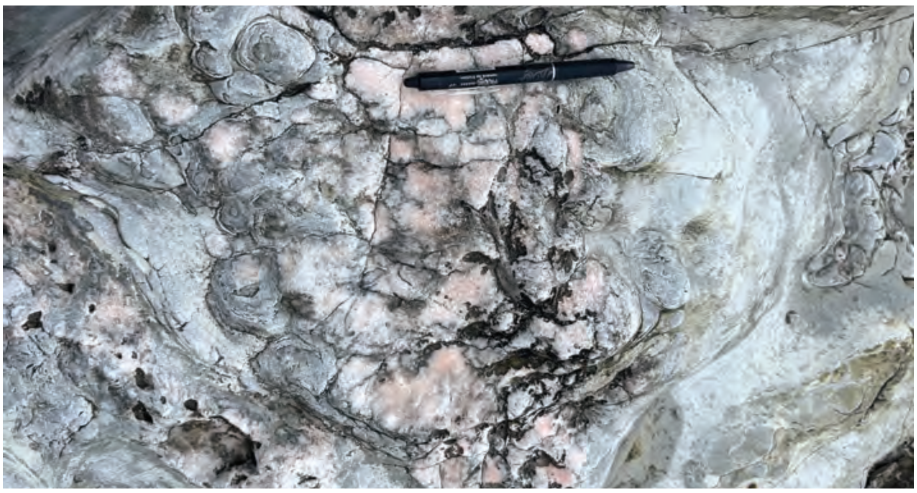

__Fig. 25.__ Field image of bed 5. Note pen (14 cm) for scale)

The nodular pseudomorphs display multiple fringed terminations, resulting in classification as gypsum converted to anhydrite nodules prior to pseudomorphism.

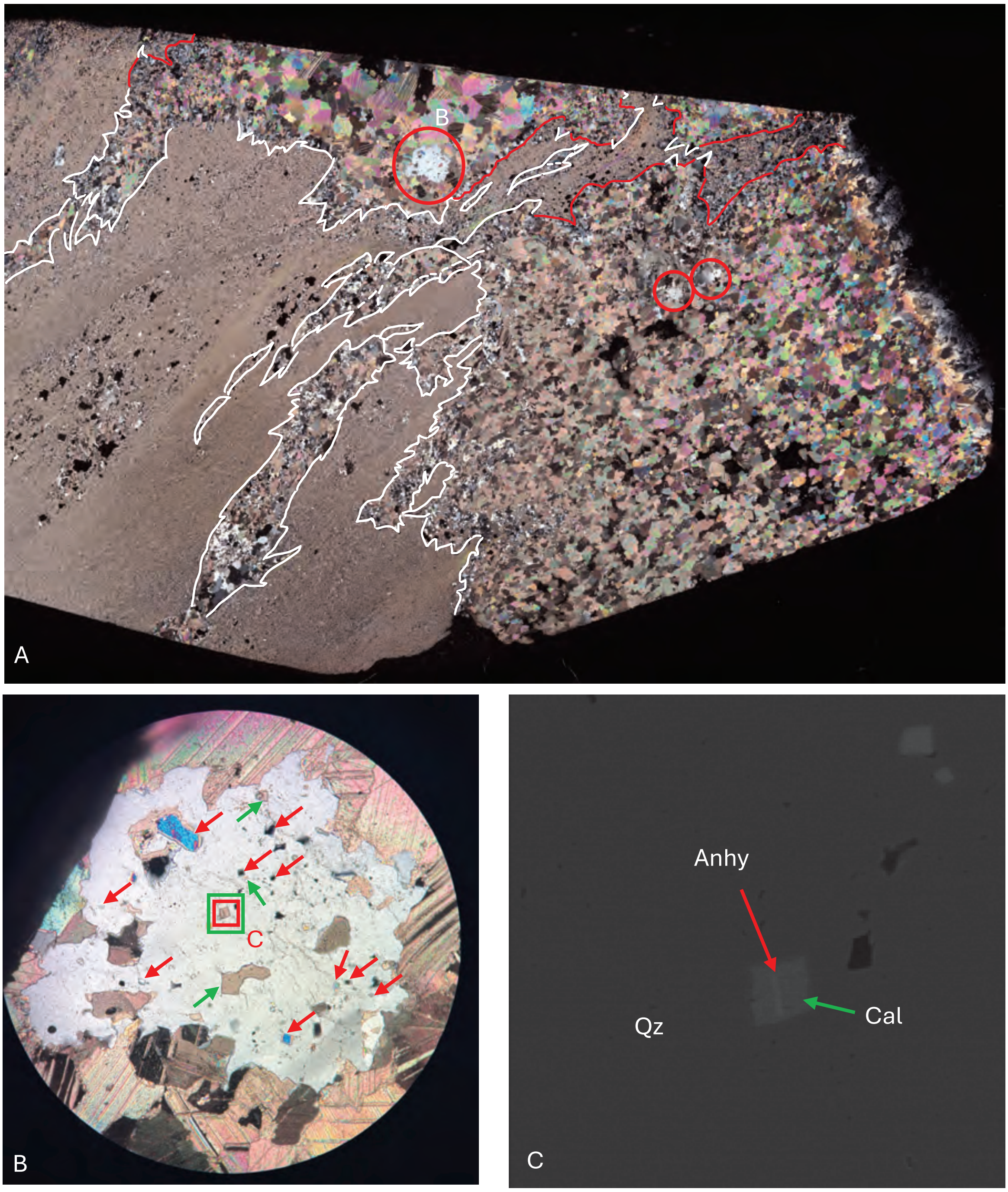

Fig. 26. *Scanned thin section 24EX111SEB, 3.8 cm wide, XPL. Unannotated version in Appendix 1. A) Cauliflower-shaped rims outlined in red, birdbeak shaped terminations and separate birdbeak shapes oulined in white. Each fringed termination is classified as a formed gypsym selinite disc. SEM-verified anhydrite inclusions in megaquartz circled in red. Pseudomorphs are rimmed by quartz, pyrite, and baryte. B) Megaquartz (labelled B in A) is embedded in sparry calcite. SEM-verified anhydrite inclusions are marked with red arrows, calcite inclusions with green arrows. C) Close-up of the red and green-framed area in B, stripe of anhydrite encapsuled by calcite.*

Additionally, the nodular pseudomorphs contain megaquartz with multiple inclusions of anhydrite (Fig. 26B), verified through SEM analysis. Raman spectroscopy confirmed the identity of anhydrite even in inclusions with low total weight percentages (<70%), ensuring they are not gypsum. In addition to nodular pseudomorphs, intergrown birdbeak-shaped pseudomorphs up to 1.3 cm long are also present. Their clustered morphology, irregular spacing, displacive growth and varying size identifies them as pseudomorphs of intrasedimentary gypsum. They contain a high percentage of baryte, both within their interiors and along their rims (Fig. 27B).

A small amount of celestite is dispersed among the sparry calcite and occurs as inclusions within megaquartz (Fig. 27C). In the latter case, a subhedral celestite crystal is surrounded by anhedral baryte, implying replacement of celestite by baryte. SEM analysis confirms that all examined celestite contains Ba, with concentrations reaching up to 24.3 wt%. Galena infills fractures in baryte, and a larger cumulate of galena (>200 µm) is present in the general matrix.

The matrix surrounding the gypsum and anhydrite pseudomorphs consists of Ba-bearing K-feldspar, graphite, framboidal pyrite, and altered dolomite rhombs. The dolomite exhibit zonation, with chemistry shifting toward calcite at the rims. Additionally, they display a saw-tooth texture (Fig. 27), indicating ongoing calcification of dolomite. Thin section 24EX111SEB is somewhat damaged from the preparation process, resulting in numerous voids within the matrix. These voids exhibit rhombic, triangular, and square shapes, suggesting that the missing minerals may have been dolomite, pyrite, and/or galena.

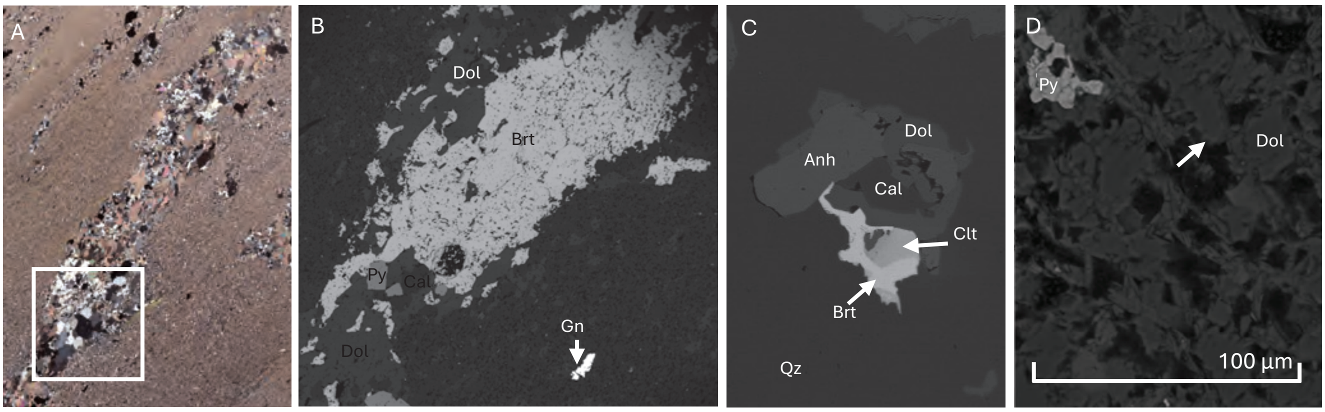

Fig. 27. *Dol = dolomite, Brt = baryte, Py = pyrite, Gn = galena, Anh = anhydrite, Cal = calcite, Clt = celestite, Qz = quartz. A) Pseudomorph of intergrown discs of birdbeak-shaped gypsum, shown in XPL. B) BSE image of framed area in A shows that baryte occupies more than 50% of the pseudomorph and is also present along its rim. C) Subhedral celestite crystal surrounded by anhedral baryte. D) General matrix of dolomite with saw-tooth edges and rims that exhibit decreasing Mg and increasing Ca content (marked with a white arrow), indicating calcification of dolomite. Framboidal pyrite is scattered throughout the matrix.*

3.6 Bed 7: Gypsum Pyritisation

Bed 7 is characterised by thin, lenticular, protruding knobs (Fig. 28). Petrographic analysis of thin section 24EX16SE (Fig. 29), with polarising microscope, reveals the matrix is primarily composed of dolomite, with minor components of muscovite, quartz, and pyrite. A flaky, opaque mineral is classified as graphite due to morphological similarities to SEM-verified graphite in other beds.

Fig. 28. *Sample of Bed 7, before cutting. Examples of protruding knobs marked with white arrows.*

The protruding knobs consist of single and intergrown lenticular birdbeak shapes (Fig. 29). Although some quartz rims and minor carbonate are present, most pseudomorphs consist predominantly or entirely of pyrite, consistent with gypsum pyritisation documented by Hall (1982). Based on shape, mineralogy, irregular spacing, clustered growth, displacive growth, and size variations, the knobs are classified as pseudomorphs of intrasedimentary gypsum.

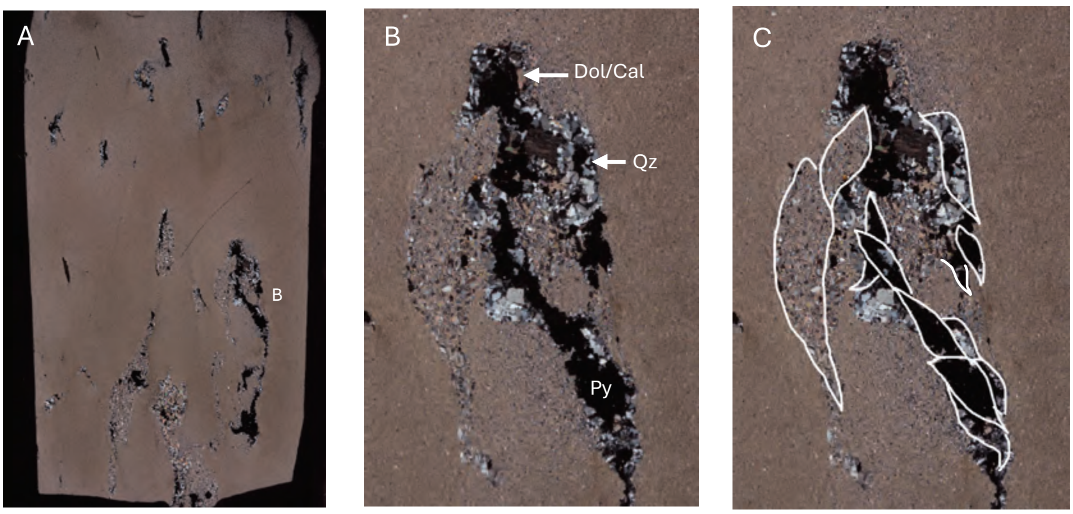

Fig. 29. A) *Thin section 24EX16SE (3.6 cm tall), XPL. Multiple pseudomorphs of single and intergrown birdbeak shapes, mostly pyritised B) Close-up of pseudomorph. C) Annotated version of B.*

3.7 Bed 8: Varied Morphology of Stromatolites

Bed 7 was identified underlying two distinct stromatolite morphologies, leading to the assumption that both types of stromatolites belong to the same stratigraphic unit—Bed 8. One morphology is domal, ranging from 60 to 80 cm in height and 40 to 70 cm in diameter. These appear individually and are spaced more than a metre apart. The other morphology is classified as columnar stromatolites appearing as a group, elongated toward the northwest (NW). These stromatolites display club-shaped heads and basal portions that are connected at the surface (Fig. 30). The tallest examples are oriented in a NW direction and exceed 1 m in height. As this bed is partly hidden by sand, there is a possibility that the bed is tilted. The columnar stromatolites lack remnants of overlying beds, while the more isolated domal forms are overlain by clay and sand.

Fig. 30. *Stromatolites with club-shaped heads, appearing as a group elongated in a NW direction. The stromatolites are connected at the surface. Note the hammer (35 cm tall) for scale.*

3.8 Beds 12–15: Stromatolites Covered by Clay and Sand

The next stromatolite-bearing unit (Fig. 31A) is Bed 12, where only domal stromatolites have been identified. These structures range from 0.9 to 1.2 m in height and 0.6 to 1.5 m in width. These domal stromatolites are overlain by Bed 13, a clay-rich unit characterised by irregular protrusions (Fig. 31B). This bed is represented in thin sections 24EX01SEA and 24EX01SED (Fig. 31C). Bed 14 consists of sand.

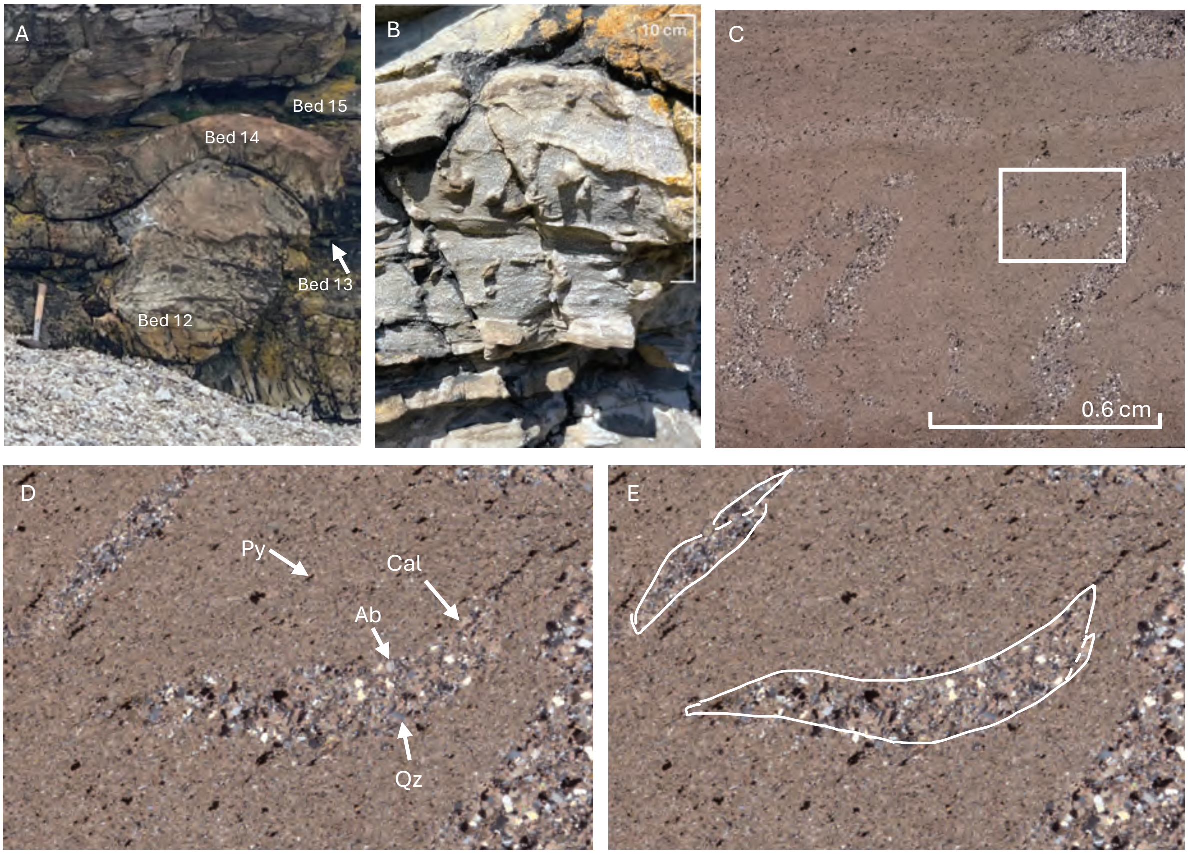

Fig. 31. *A) Field image of a domal stromatolite from Bed 12. Bed 13 appears only faintly between the stromatolite (Bed 12) and the overlying sand bed (Bed 14), but thickens further away from the stromatolite. B) Field image of Bed 13, with irregular protrusions. C) Part of thin section 24EX01SED (XPL), sampled from Bed 13, is presented. The full width of the thin section is 4 cm. D) Close-up of framed area in C. E) Annotated version of D. Dashed lines are interpretations of internal shape based on orientation of fringed terminations. Py = pyrite, Ab = albite, Cal = clacite, Qz = quartz.*

Examination of thin section 24EX01SEA (Fig. 31B) under a polarising microscope reveals that the protrusions are connected to laminae consisting of rutile, albite and relatively large and rounded grains of quartz. The pseudomorphs contain similar mineralogy as these lamina, but with the addition of calcite. Detrital minerals within pseudomorphs and lack of a rim lead to classifying the suggested gypsum precursor to have dissolved at the surface. The general matrix consists of muscovite and dolomite. Elongated, framboidal pyrites are lineated throughout the matrix.

In thin sections 24EX01SEA and 24EX01SED, no pseudomorphs with rugose rims are identified. However, multiple lenticular shapes with hooked endings are present. Based on their morphology, these shapes are suggested to be pseudomorphs of intergrown gypsum selenite discs, having dissolved at a rate exceeding replacement. As these shapes appear within the general matrix, display irregular placement, variations in size and a clustered morphology, they are thought to be reflect intrasedimentary precipitation.The dolomitic clay matrix contains thin, opaque strips exhibiting lineation. These strips are classified as graphite based on their morphology and optical properties, which correspond to SEM-verified graphite observed in other thin sections.

Bed 15, which overlies the sand bed, is a clay-rich unit. In the field, lenticular, protruding knobs with black and/or red colouring are observed (Fig. 32). Thin section 24EX100SEB (Fig. 33A) reveals that these knobs are nearly fully pyritised birdbeak-shaped pseudomorphs (Fig. 33A–E), also containing quartz, minor calcite and biotite $K(Mg,Fe)_3AlSi_3O_{10}(OH)_2$. Reflected light microscopy shows partial replacement of pyrite by goethite.

Based on the birdbeak shapes of the pseudomorphs, their clustered morphology, irregular spacing, displacive growth and previous documentation of gypsum pyritisation by Hall (1982), the protruding knobs are classified as pseudomorphs of intrasedimentary gypsum. Pseudomorph-like forms with abundant strain fringes were excluded from interpretation. The general matrix consist predominantly of muscovite, with minor quartz, albite, and rutile.

Fig. 32. *Field image of bed 15, seen from above. Black arrows mark examples of protruding knobs.*

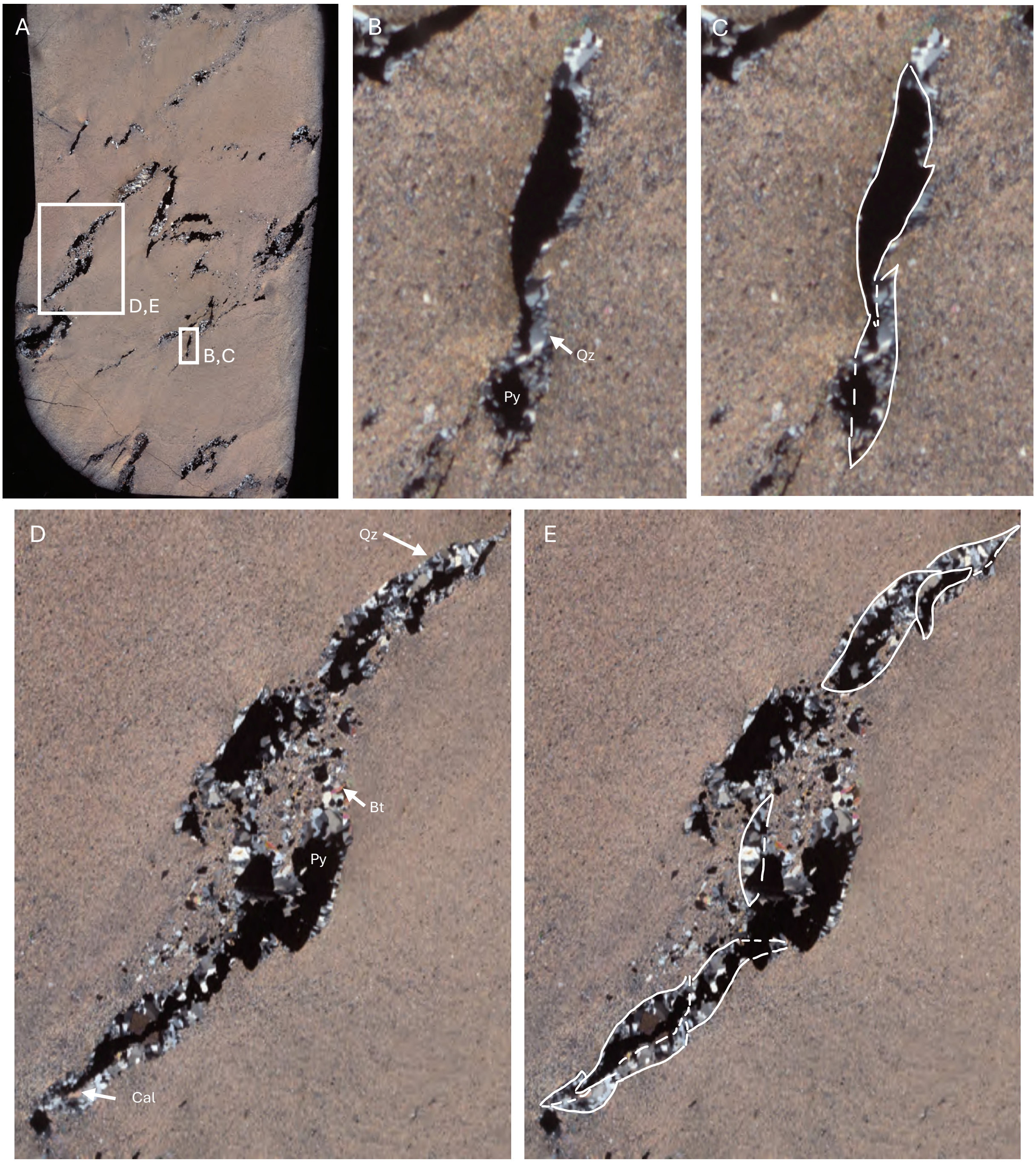

Fig. 33. All images shown in XPL. Dol = dolomite, Qz = quartz, Py = pyrite, Bt = biotite. A) Thin section 24EX100SEB (4 cm tall). Multiple pyritized pseudomorphs of intrasedimentary gypsum. B) Close up of frame, seen in A. C) Annotated version of B. D) Close-up of frame seen in A. E) Annotated version of D. Dashed lines are interpretations of probable continuation of shapes, based on orientation of fringed terminations.

3.9 Subsequent Stratigraphic Units and Evaporitic Features

Beds 16-34 in the stratigraphic column (Fig. 10) contain repeated occurrences of beds with microbialites, ripple marks, and density inversion structures. These units are interbedded with dolomitic strata containing varying proportions of mica and quartz. Beds in which quartz dominates are classified as silt or sand beds, those dominated by mica are classified as clay beds.

Due to the repetitive nature of these units they are described in groups of beds rather than individually. All samples related to the following descriptions were collected from Sections 1, 2, and 4 (Fig. 9), all of which exhibit nearly horizontal bedding. As previously described, in examined beds from Bed 1 to Bed 15 evaporitic pseudomorphs display rugose rims composed of quartz and pyrite. In beds correlated to the upper part of the stratigrahic column, pseudomorphs mostly lack distinct rims.

3.9.1 Beds 16, 18, 20, 24, 30, and 33: Rippled Beds

The upper part of the stratigraphic column contains six rippled beds (Fig. 34). These beds have been examined only in the field and not in thin section. They are inferred to consist of dolomitic sand and clay, with the presence of dolomite suggested by the orange-weathering pattern observed in the outcrops. However, this coloration may also be attributed to iron-rich sediments. Quartz-rich sections protrude from the surrounding, more clay-rich material. Where present, sand beds located above or below the rippled units are horizontally bedded, indicating that the rippled structures are not the result of folding.

Fig. 34. *Field image of a rippled bed. Thin beds of sand, lacking indications of deformation, marked with white arrows. Note hammer (35 cm) for scale.*

3.9.2 Beds 17, 19, 21, and 25: Lithified Microbial Mats

In addition to the previously described stromatolites, evidence of microbial activity is also preserved in the form of lithified microbial mats (Fig. 35) within four different beds. Most of them includes continous repetitions of microbial mats (Fig. 35B).

Two beds with lithified microbial mats were examined using a polarising microscope. The lowermost one of them, Bed 17, was analysed in thin section 24EX12SEB (Appendix 1), in which two pseudomorphs were detected (36A, B). The orientation of surrounding matrix conforms to the pseudomorphs shape, indicating displacive growth. Rims consist of quartz and pyrite.

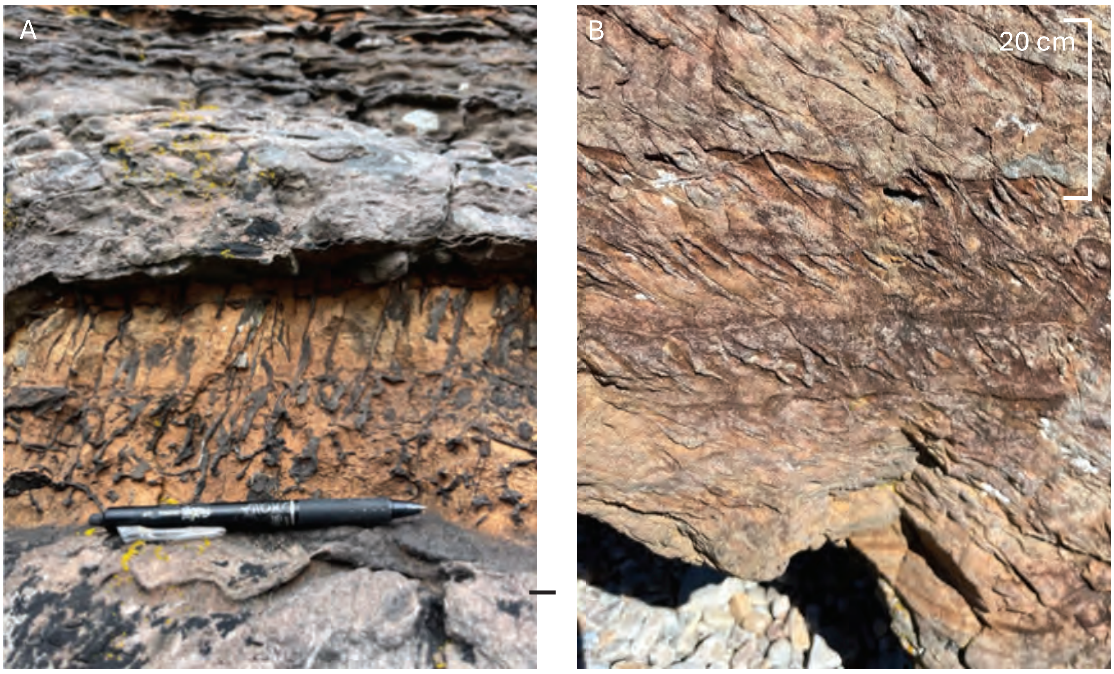

Fig. 35. *Field images of lithified microbial mats. A) horizontally bedded microbial mat, Bed 19. Dark brown features are quartz-dominated lithified microbial mats. Downgoing features represent mudcracks, forming at a drying surface. Note pen (14 cm) for scale. B) A natural crosscut of continuously repeated lithified microbial mats (documented as one bed all together) seen from side perspective, Bed 17.*

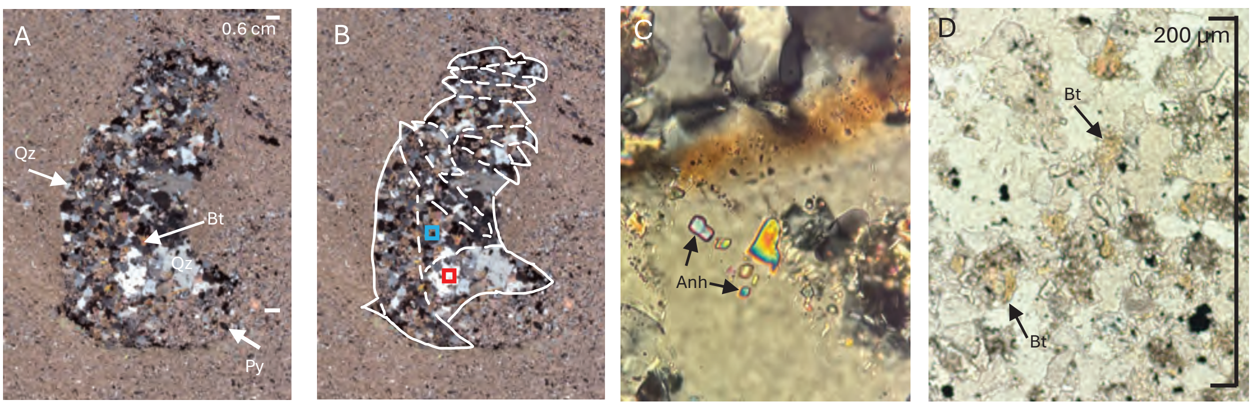

Fig. 36*. A-C, XPL. D, PPL. A) Largest intrasedimentary pseudomorph in thin section 24EX12SEB, with discontinuous rim of quartz and pyrite. Full thin section seen in Appendix 1. B) Annotated version of A. Interpretations of internal shapes masked with dashed lines, based on direction of fringed terminations. C) Close up of red frame in B, inclusions classified as anhydrite. D) Close-up of area framed in blue in B. Bt = Biotite, with no distinct crystal shapes.*

The largest pseudomorph (Fig. 36 A, B) contains megaquartz with anhydrite inclusions in its interior. Although these inclusions have not been verified using SEM, their position within megaquartz—along with their size, rectangular shape, and interference colours—closely resembles SEM-verified anhydrite inclusions observed in previously described thin sections. This pseudomorph also contains biotite, which is absent from both the general matrix and other structures within the same thin section. The biotite is classified as metamorphic, due to shape and positioning in the rimmed pseudomorph. The general matrix of thin section 24EX12SEB consists predominantly of dolomite, with minor muscovite and framboidal pyrite spread throughout the matrix.

The second lithified microbial mat analysed under a polarising microscope corresponds to Bed 25 in the stratigraphic column (Fig. 10) and was examined in thin section 24EX23SED (Fig. 37A). Several potential pseudomorphs are present, but many are distorted by pyrite with strain fringes and have been excluded. However, pseudomorphs free from pyrite strain fringes exhibit characteristic glauberite shapes (Fig. 37 B-E). All pseudomorphs lack rims and contain quartz and biotite, some contain minor calcite and pyrite. Biotite is absent from the general matrix. As in Bed 17, the biotite lacks distinct crystal shapes and are inferred to be metamorphic.

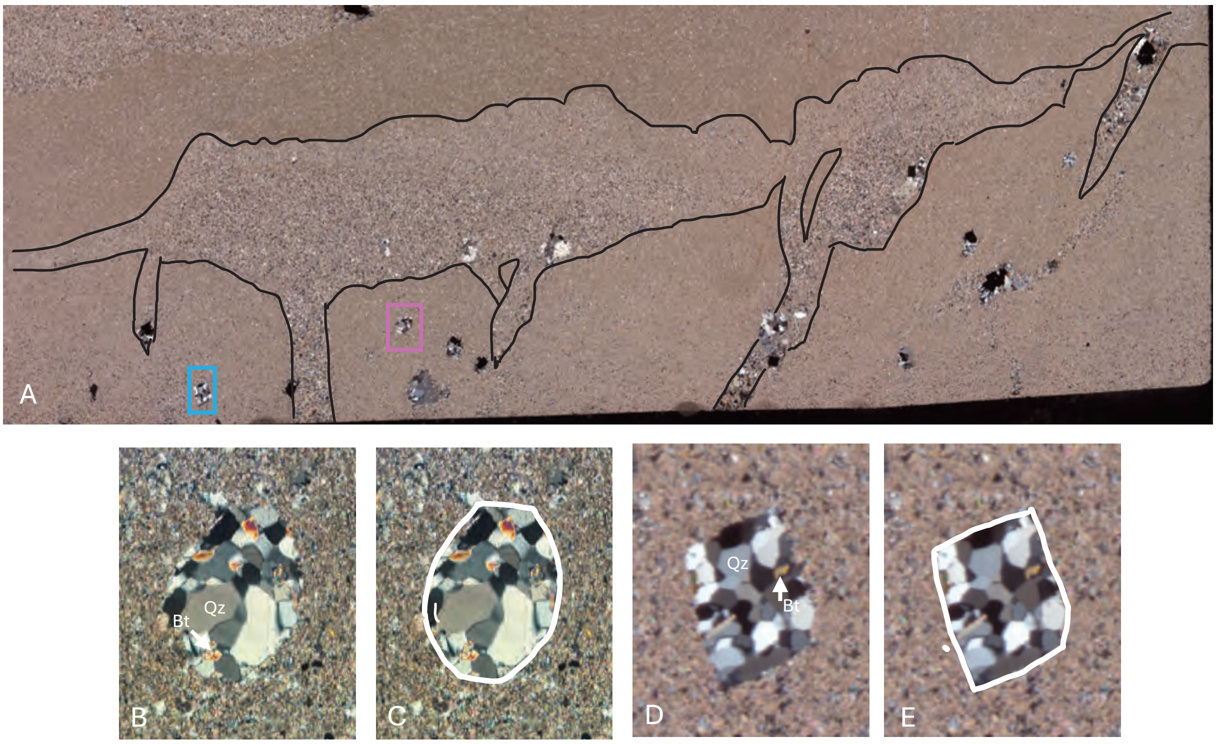

Fig. 37. *All images are shown in XPL. A) Scanned thin section 24EX23SED (3.9 cm wide), Annotation of microbial mat in black. Full thin section without annotations is seen in Appendix 1. B) Close-up of pink frame in A. Pseudomorph lacking rim, displaying glauberite crystal shape. C) Annotated version of B. D) Close-up of blue frame in A. Pseudomorph displaying the more rectangular crystal habit of glauberite. E) Annotated version of D.*

The lithified microbial mat in thin section 24EX23SED is preserved as a quartz-rich structure containing dolomite, rutile, and albite. The surrounding matrix consists almost entirely of dolomite, with minor muscovite and quartz. The matrix conforms around the shape of the pseudomorph, indicating displacive, intrasedimentary growth.

3.9.3 Bed 26; Bands of Pyrite

One bed that stands out from the repetitive structures in the upper part of the stratigraphic column is Bed 26. Part of Section 1 (Fig. 9) is protected from wind and rain; here, a powdery grey portion of Bed 26 is exposed (Fig. 38). When touched, it has a flour-like texture. In areas exposed to rain, the bed exhibits an orange-brown coloration.

Fig. 38. *Field image of Bed 26, displaying bands of pyrites.*

Bed 26 has a striped appearance due to thin beds densely packed with pyrite. Investigation with polarising microscope of thin section 24EX17SEA reveal most of the pyrite displays extensive strain fringes, making it difficult to distinguish plausible pseudomorphs. However, three distinct pseudomorphs are present, all with shapes typical of glauberite (Fig. 39). The pseudomorphs consist of quartz and biotite, sometimes also calcite and pyrite. All pseudomorphs lack distinct rims. The matrix conforms to the shapes of pseudomorphs, which also display clustered morphology and irregular spacing.

The surrounding matrix is dominated by muscovite, with approximately 10–20% each of dolomite, quartz, and biotite which is aligned with the muscovite. In pseudomorphs, biotite follow shapes of quartz along the edges or in the interior of the pseudomorph. Also, biotite is present in strain fringes. All biotite in Bed 26 is classified as metamorphic.

Fig. 39. Pseudomorphs with clustered morphology of glauberite, seen in thin section 24EX17SEA, XPL. Full thin section seen in Appendix 1. Interpretations of internal shapes in dashed lines. Matrix surrounding pseudomorphs adapt to the pseudomorphs shapes.

3.9.4 Beds 27, 29 and 31 – Density Inversion Structures

The uppermost part of the stratigraphic column includes three density inversion structures, where one bed has sunk into the underlying strata. The sinking sections are referred to as "downgoing features." Beds over- and underlying density inversion structures remain undisturbed apart from the regional metamorphism (Fig. 40), ruling out seismic activity as the cause of these intrabed slumps (Fig. 41).

The two most similar density inversion structures, Beds 27 (Fig. 42 C) and 29 (Fig. 41) (Fig. 42 A), were examined under a polarising microscope using thin sections 24EX27SED and 24EX13SEB, respectively (Fig. 42 B, D). Although these structures comprise three distinct beds, they are represented as a single unit in the stratigraphic column (Fig. 10) due to their interactions. In the field, the uppermost bed and its downgoing features appears dark brown to black (hereafter referred to as "black"). It slumps into a 3–7 cm thick enterolithic, orange middle bed, occasionally penetrating it completely. In bed 29, pseudonodules are released from the black bed into the underlying strata (Fig. 41). The lowermost of the three beds is greyish-brown to beige in colour (hereafter referred to as "brown"). Its basal portion exhibits a sagging geometry with coherent internal layering that conforms to the downgoing features of the uppermost black bed.

Fig. 40. Field image with overview of Bed 29 (white arrows). Adjacent beds are not disturbed apart from the regional greenschist metamorphism. The density inversion structure appear as intrabed slumps.

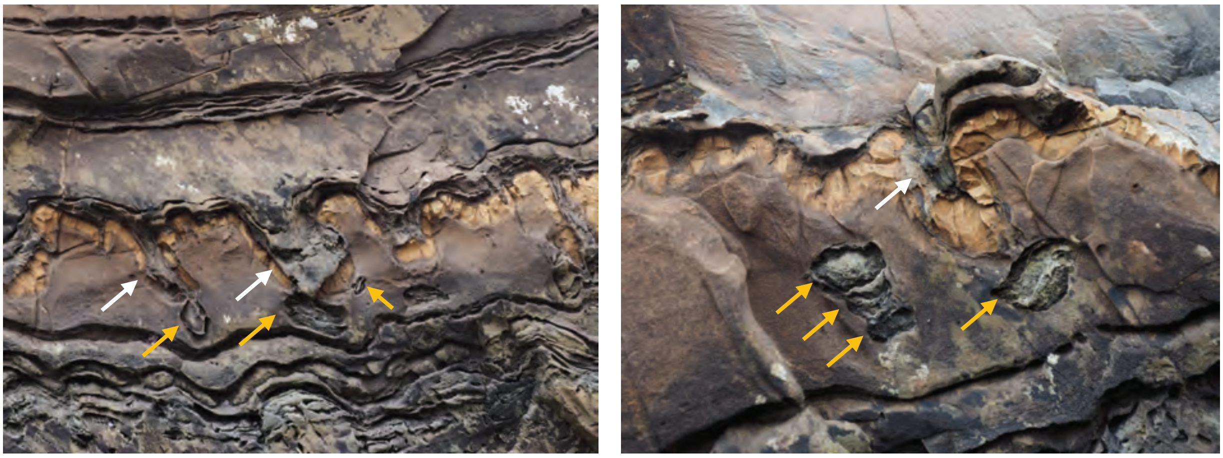

Fig. 41. Field images showing examples of downgoing features (white arrows) and pseudomodules (orange arrows) of Bed 29. Images; courtesy of Alasdair Skelton.

Under the polarising microscope, the mineralogy of the downgoing features in thin sections 24EX13SEB and 24EX27SEA exhibits similarities. Both contain abundance of heavy minerals (Table 2); rutile, albite, fluorapatite and biotite along with clusters of relatively large calcite. Zircon and monazite were detected with the SEM in Bed 29. Both Beds 27 and 29 exhibit a cryptocrystalline texture appearing pale to dark brown in PPL (Fig. 42C, F). SEM analysis of this texture in thin section 24EX13SEB reveals it consists of fluorapatite, quartz, and dolomite (Fig. 43). Multiphase texture including apatite and carbonate is typically formed in detrital accumulations undergoing mineralization at the sediment-water interface (Yi et al., 2013).

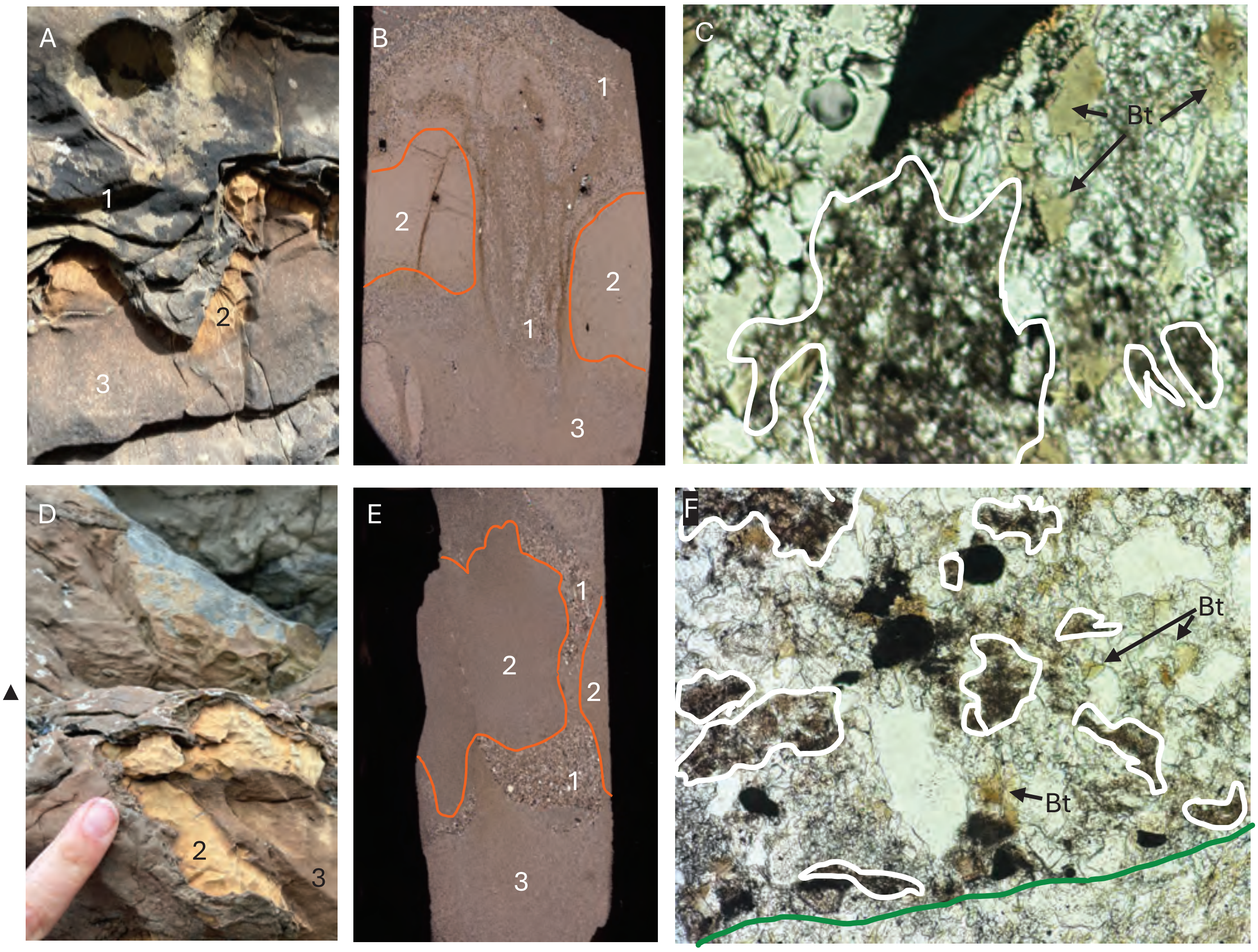

Fig. 42. *(1) the overlying black bed, from which the downgoing features originate (not seen in field image 42D); (2) the enterolithic orange bed, varying between 3 and 7 cm in thickness. (3) the lowermost brown bed. Unannotated versions of images B, C, E, and F are available in Appendix 1. A) Field image of Bed 29, which was examined in B) thin section 24EX13SEB, XPL. C) Cryptocrystalline texture, annotated in white, in thin section 24EX13SEB, PPL, 18,320× magnification. D) Bed 27, examined in E) thin section 24EX27SED, XPL. Annotations of orange bed based on the corresponding hand sample. F) Cryptocrystalline texture in thin section 24EX27SED, PPL, 4,580× magnification. Boundary between the downgoing feature and the lowermost bed marked in green. Bt = biotite.*

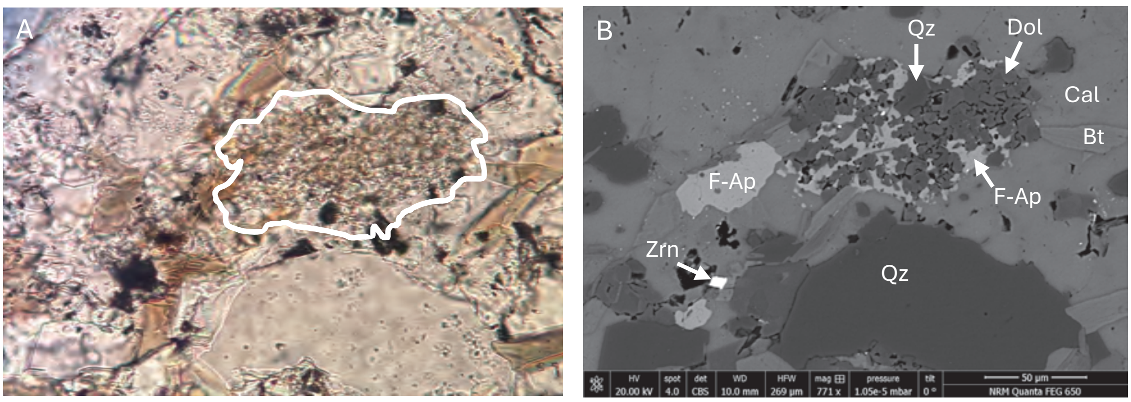

Fig. 43. *A) Cryptocrystalline texture in thin section 24EX13SEB, PPL. Unannotated version of image in Appendix 2. B) BSE-image of the cryptocrystalline texture seen in A). F-Ap = fluorapatite, Qz = quartz, Dol = dolomite, Bt = biotite, Cal = calcite Mn- and Fe-bearing, Zrn = zircon.*

Overlying, black bed	Rel. grain size	Rel. abundance	Av. density g/cm3
Biotite	medium-large	large	3.09
Calcite	very large	large	2.71
Dolomite	minimal	minor	2.84
F-apatite	medium and large	medium	3.19
Rutile	small-medium	medium	4.2
Pyrite	medium-large	small	5
Monazite	small	small	4.6-5.7
Zircon	small	small	4.6-4.7
Quartz	predominantly small	small	2.65
Chalcopyrite	minimal	minor	4.19
Goethite	minimal-small	minor	3.8
Cryptocrystalline texture	medium-large	medium	3.8
Middle, orange bed			
Dolomite	minimal	large	2.84
Quartz	equal to quartz in black bed	small	2.65
Biotite	equal to quartz in this bed	small	3.09
Underlying, brown bed			
Biotite	same as black bed	medium	3.09
Calcite	medium-large	minor	2.71
Quartz	small	small	2.65
F-apatite	medium-large	small	3.19
Rutile	small-medium	small	4.2
Dolomite	minimal	large	2.84
Pyrite	small-medium	minor	5
Monazite	small	minor	4.6-5.7
Zircon	small	minor	4.6-4.7

Table 2. *Mineralogy, densities (mindat.org), relative grain size and relative abundance of minerals in the 3-bed succession of Bed 29, examined in thin section 24EX13SEB. The amount of zircon and monazite increases with depth of the downgoing feature of the black bed. Note that these densities are average densities. In thin section 24EX13SEB, calcite is as dense as biotite, due to enrichment in Fe and Mn.*

Heavy minerals are more concentrated in the black bed of Bed 29 than in Bed 27, comprising ≥90% of the composition, with quartz ≤5%. These values exclude calcite-rich clusters. Quartz grains are generally equal in size to or smaller than the heavy minerals. In contrast, Bed 27 contains relatively large and rounded quartz, classified as detrital, and heavy minerals make up ≤50% of the black bed.

In Bed 27, the orange bed contains equal amounts of muscovite and dolomite, while the brown bed is dominated by quartz with equal parts of biotite, dolomite, and aligned muscovite. In Bed 29, the orange bed consists predominantly of dolomite, with 10% biotite and 10% quartz. The lowermost brown bed is composed of dolomite with minor muscovite and ≥30% of the same heavy minerals as the black bed. In thin section 24EX13SEB, the downgoing feature penetrates the orange bed. At the contact between the black and the brown bed, the biotite rim of the downgoing feature appears diffuse, and minerals from the black bed seem to have migrated into the underlying brown bed (Fig. 44). At the very bottom of the downgoing feature examined in thin section 24EX13SEB there is a U-shaped accumulation of chert.

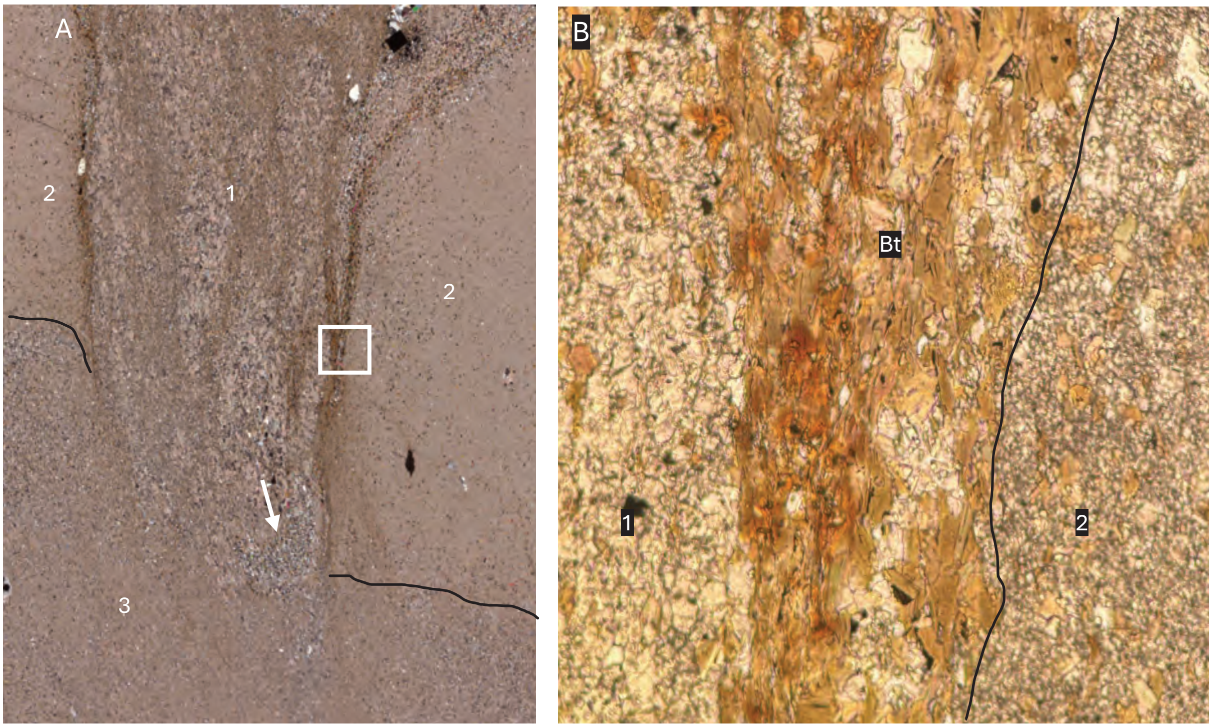

Fig. 44. *A) Downgoing feature of the black bed (1) penetrating the orange, enterolithic bed (2). At the contact with the brown bed (3), the rim of aligned biotite appears diffuse, and heavy minerals from the black bed seem to migrate into the brown bed. The boundary between Beds 2 and 3 is annotated in black. Accumulation of chert marked with white arrow. The full thin section, without annotations, is available in Appendix 1. B) Close-up of the framed area in A. Biotite is dispersed throughout the black bed and its downgoing feature but also aligns to form a rim contouring the downgoing structure. The boundary between the downgoing feature of Bed 1 and the orange Bed 2 annotated in black. Bt = biotite.*

The downgoing feature in thin section 24EX13SEB is bordered by a distinct rim of biotite (Fig. 44), whereas the downgoing feature in thin section 24EX27SEA lacks such a rim. The biotite in the rim in thin section 24EX13SEB is classified as detrital as it exhibits distinct, yet fragmented, crystal shapes with irregular and/or rounded terminations. The same texture is observed in biotite dispersed within the rest of the black bed and biotite scattered throughout the brown bed of the same thin section. In the black bed, the orientation of biotite is fairly horisontal in sections not slumping downwards and vertical within the downgoing feature. In contrast, biotite in the orange bed of thin section 24EX13SEB is classified as metamorphis, due to its random orientation and lack of well-defined crystal shapes. A similar texture and irregular orientation are seen in the biotite of Bed 27 (Fig. 42F), thin section 24EX27SED.

Apart from the multiphase fluorapatite/dolomite/quartz texture typical for detrital accumulations, thin section 24EX13SEB includes another texture commonly found in detrital accumulations; Leucoxene (Fig. 45). SEM measurements reveal that the leucoxene in thin section 24EX13SEB consist of rutile and quartz.

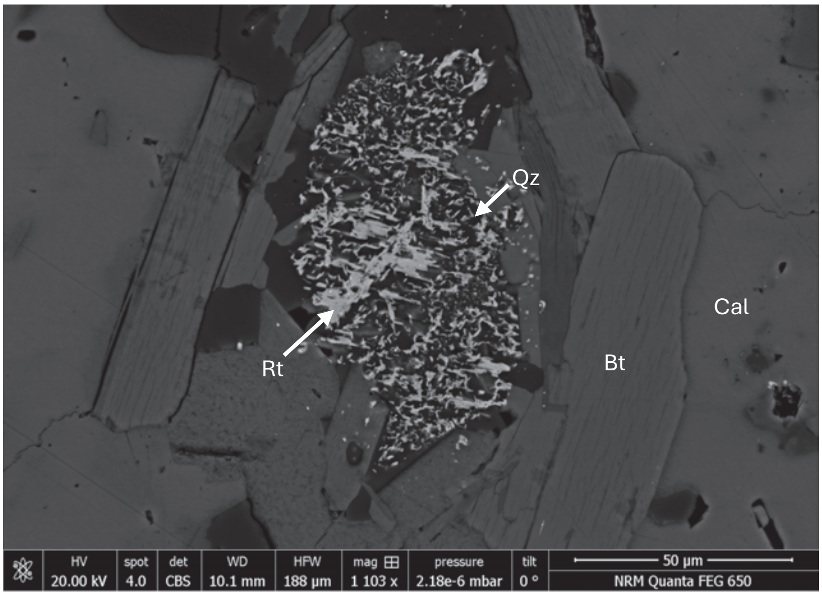

Fig. 45. *BSE image of leucoxene, thin section 24EX13SEB.*

Monazite and zircon increase in abundance with depth along the downgoing feature seen in thin section 24EX13SEB (Fig. 46A). Some monazite grains are rounded, while others are more angular and exhibit sharp, thin protrusions. SEM analysis of monazite in 24EX13SEB reveals Th concentrations ranging from 1.43 to 2.53 wt%, with no Y detected. Ca content is depleted in some of them. Monazite has been identified as authigenic in low-grade metamorphic rocks, typically displaying Th concentrations below 3 wt% and depleted Y and Ca values (Zi & Rasmussen, 2024). The findings by Zi & Rasmussen (2024) combined with the values retrieved with the SEM suggest that some of the monazite may be authigenic. The black bed in thin section 24EX13SEB contains fluorapatite with saw-tooth textures and zoned fluorapatite grains (Fig. 46 B, C). SEM analysis shows that these fluorapatite grains have Ce- and Nd- bearing cores, while lacking these elements in their rims.

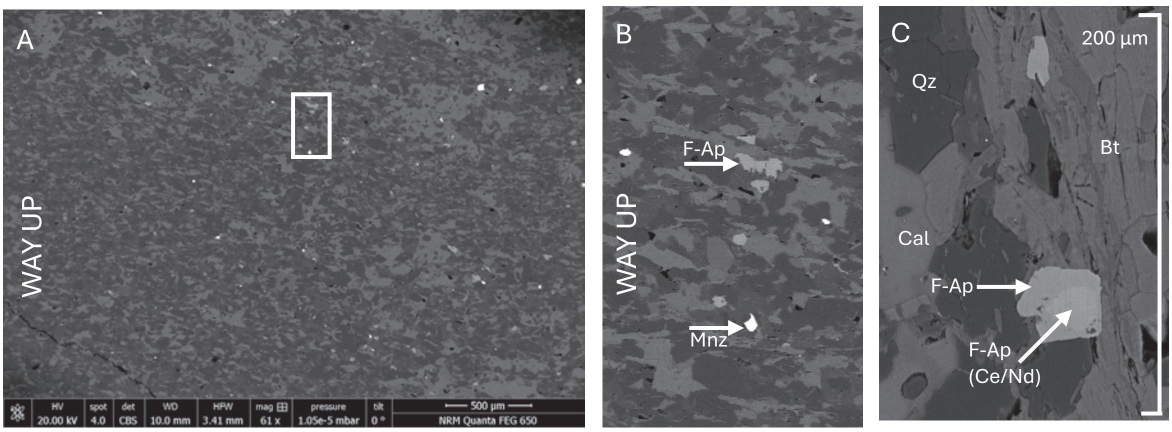

Fig. 46. *BSE images from the interior of the downgoing feature in thin section 24EX13SEB.* ***A)*** *Abundance of monazite and zircon (the most pale phase) increases towards the bottom of the downgoing feature.* ***B)*** *Framed area seen in A. Sawtooth fluorapatite and monazite with sharp protrusion. C) Zoned fluorapatite. F-Ap = fluorapatite, Cal = calcite, Qz = quartz, Bt = biotite.*

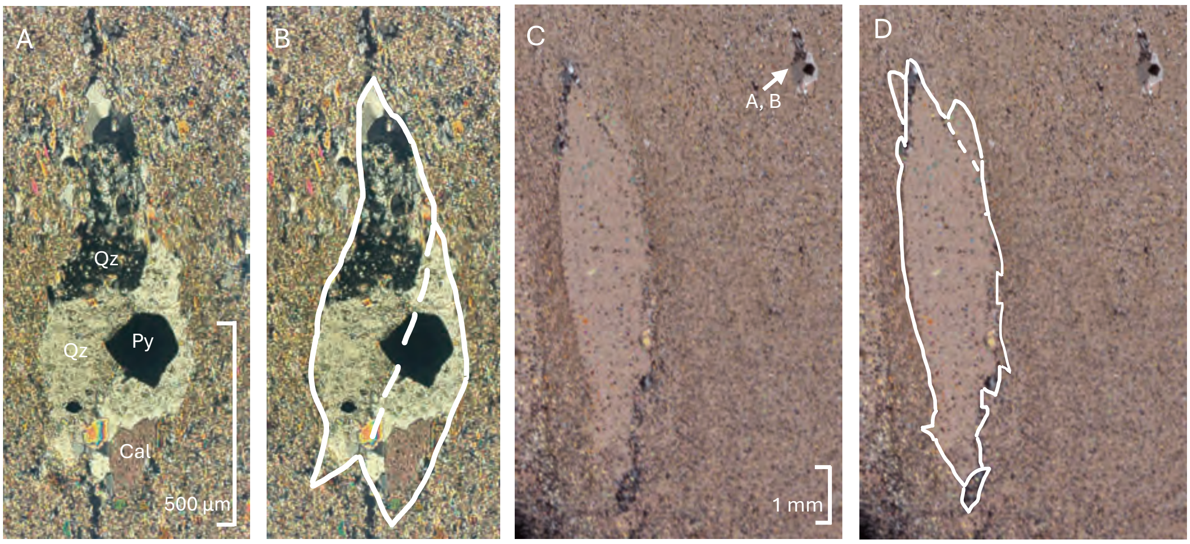

Fig. 47. *A) One of several pseudomorphs, from the brown bed seen in thin section 24EX13SEB, XPL. These pseudomorphs lack rims. B) Annotated version of A, with interpreted former crystal shapes (dashed line) based on fringed terminations. B) Relatively large lenticular pseudomorph with partial rim and somewhat fringed terminations.*

The orange and brown bed seen in thin section 24EX13SEB contain several pseudomorphs (Fig. 47). Most of them are 1-2 mm tall and consist of poikilitic quartz, calcite and sometimes pyrite. Some of the shapes display birdbeak endings, while some display a more oval shape. Calcite typically occur at the bottom of the pseudomorphs. Also, the brown bed contain two larger shapes, with partial rims of quartz and pyrite. Their interior consist of dolomicrite. The pseudomorphs are classified as gypsum, possibly glauberite.

The calcite clusters, mentioned in the beginning of this section, consist of relatively large calcite (up to 400 µm) positioned within the downgoing features of both thin sections 24EX13SEB and 24EX27SEA. Even thought he calcite is clustered it remains separated by heavy minerals. SEM analysis reveals that the calcite is as dense as biotite due to its Mn- and Fe-bearing composition, with concentrations reaching up to 0.23 wt% Mn and 0.83 wt% Fe. This composition is consistent with the capillary pore water chemistry described in previous sections. The calcite is porous and frequently conforms to the shape of surrounding minerals, suggesting it is authigenic rather than detrital.

Pyrite in thin section 24EX13SEB is partially or fully replaced by goethite (FeO(OH). In some instances, pyrite also contains specks of chalcopyrite ($CuFeS_2$). Additionally, copper is observed in rare occurrences of malachite, verified by SEM in thin section 24EX13SEB.

The third density inversion structure is observed in Bed 31 (Fig. 48A) and was examined in thin section 24EX10SEC (Fig. 48B). Unlike Beds 27 and 29, this structure lacks an enterolithic middle bed. Instead, an overlying bed intrudes directly into an underlying unit in a multidirectional, knobbly pattern. The downgoing features consist mainly of relatively large, rounded, non-poikilitic quartz, classified as detrital. Additionally, rutile and biotite are present, both exhibiting distinct crystal shapes with broken edges, supporting their classification as detrital. Clusters of relatively large calcite conforms to the shapes of surrounding grains and is classified as authigenic. The underlying bed is composed predominantly of muscovite, with minor amounts of dolomite.

Within this bed, inclusions closely resembling SEM-verified anhydrite were identified using a polarising microscope. Some inclusions display square, pink shapes with a central blue stripe (Fig. 48C), identical in appearance to those observed in calcite-hosted anhydrite in Bed 6. Others are similarly square and exhibit the same distinctive blue colour in cross-polarised light as described in several beds.

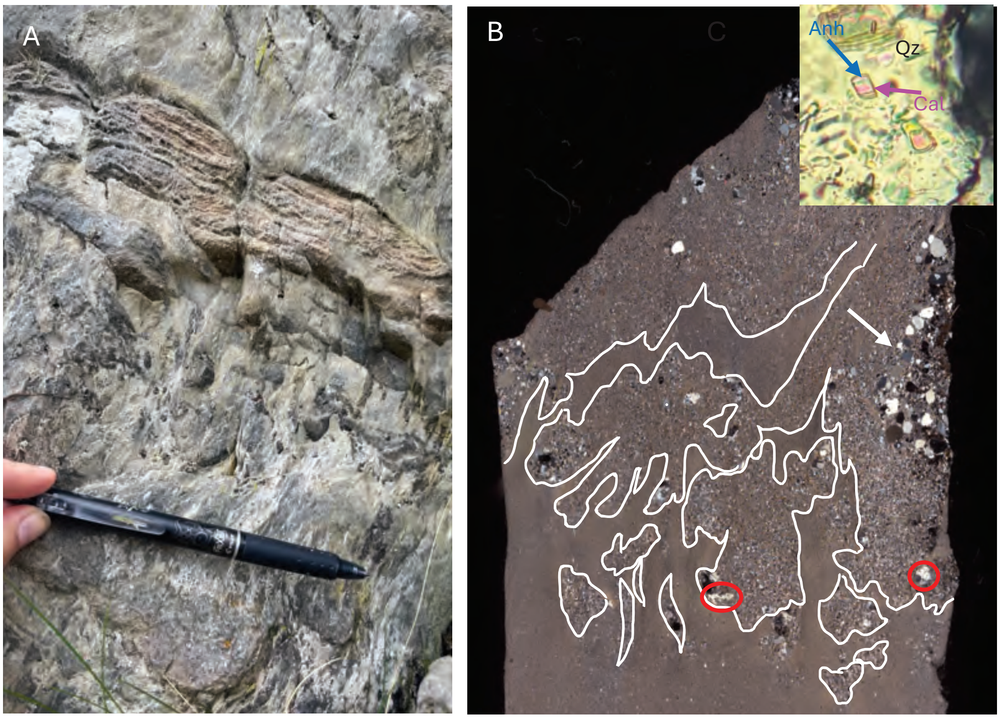

***Fig. 48**. **A)** Field image of bed 31. **B)** Thin section 24EX10SEC (max height 4 cm). Sinking, knobbly structures and gypsum birdbeak shapes annotated in white. Locations of megaquartz with inclusions resembling anhydrite inclusions marked in red. Unannotated version of thin section seen in Appendix 1. C) Close-up of megaquartz with inclusions of suggested calcite (pink) encapsulating anhydrite (blue stripe), identical to an inclusion verified as anhydrite/calcite with SEM in Bed 5.*

4. Discussion

This study documents an extensive presence of pseudomorphs of intrasedimentary evaporites, establishing that evaporite formation was controlled by capillary brines. The only evaporitic environment where capillary action is the dominant hydrological process is a sabkha. Other evaporitic environments, such as salars and salinas, can also be influenced by capillary action, but it is not the dominant process. Apart from pseudomorphs of intrasedimentary evaporites there is further evidence supporting a sabkha as depositional environment and major cause of diagenetic overprint for Member 3 of the BDF. These include mineralogy, ion recycling, fluctuating oxygen levels, and structures such as haloturbation and dissolution of salt beds on the sabkha surface.

Even the gypsum pseudomorphs in Bed 2, which only displays intrasedimentary characteristics around their base, fits the sabkha theory. In sabkhas, evaporites may precipitate from an evaporating outcrop of the brine on the sabkha's surface. Such evaporites sit in cracks, formed along the shape of the evaporite (Warren, 2016).

Compared to modern sabkhas, Member 3 of the BDF exhibits anomalously high detrital input, suggesting unusual levels of precipitation. For evaporites to have formed in an environment with recurring heavy rainfall, evaporation rates during dry periods must have been exceptionally high. Thus, an extremely warm climate is inferred. The morphology of gypsum selenite birdbeak discs suggests minimum depositional temperatures of 35 °C (Warren, 2016), with no evidence of colder conditions.

The occurrence of gypsum and anhydrite in Member 3 of the BDF is consistent with precipitation in both near-marine/supratidal and continental sabkhas. The presence of glauberite—typical of continental sabkhas—in the uppermost beds of the stratigraphic column suggests a partial transition from a supratidal to a continental sabkha. This continental sabkha would still have been situated near the ocean but without influence by marine flooding.

The evolution of pseudomorphs, from those with rugose rims of quartz and pyrite in the lowermost and middle beds to those lacking rims in the upper beds, indicates a shift in dissolution or replacement rates. Pseudomorphs with distinct rims are interpreted to have been dissolved and replaced solely by capillary brines, while those lacking rims likely underwent dissolution at the surface, even allowing detrital minerals to infill vugs formed by the dissolution of evaporites. This type of dissolution is thought to reflect influxes of marine and/or meteoric water.

In regards to dolomite formation, resurging groundwaters cause a diagenetic overprint within the sabkha, causing widespread dolomitisation. At the same time, biogenic dolomite is thought to have been precipitated by microbialites.

Vertical Recycling

Resurging groundwater in the capillary zone causes ion recycling. The capillary brine redistributes ions vertically as it moves upward and downward—dissolving and precipitating minerals (Warren, 2016). This is evident in several aspects of Member 3 of the BDF. Dolomitisation of phreatic mud is inferred in beds containing both clay and subhedral to euhedral dolomite. In Member 3 of the BDF, dolomite significantly exceeds calcite, implying a generally high Mg/Ca ratio in the brine. Geochemical redistribution is also indicated by the depletion and enrichment of elements such as Ce, Nd, Ti, Mn, and Al in various minerals.

A continuous enrichment of iron (Fe) is observed in the consistent presence of pyrite and ferroan dolomite from the lowermost to the uppermost beds of the stratigraphic column. During a panglaciation, large amounts of soluble Fe would be suspended in ocean water, persisting over extended periods (Hoffman et al., 2017). The enrichment of Fe and Mg in the capillary brine may reflect subsurface lateral inflow of marine water. In regards to Fe, marine flooding of the sabkha may also have deposited clay minerals with Fe bound to their surfaces. Iron release does not occur at modern surface temperatures unless microbial respiration is active. Microbial extraction and reduction of Fe from clay releases Ca, Fe, and bicarbonate. In the presence of sulphate reduction, pyrite will nucleate, and the resulting Ca and bicarbonate will precipitate as carbonate (Vorhies, 2009).

As surface waters does not affect the brine chemistry at large (Warren, 2016), the presence of baryte within pseudomorphs is thougt to derive from subsurface processes. The appearance of baryte within pseudomorphs coincides with the appearance of detrital Ba-bearing feldspars. This could be linked to the capillary brine incorporationg Ba^{2+} from the detrital feldspar, precipitating it as baryte simultaneously as dissolving $CaSO_4$. The appearance of baryte could also be linked to subsurface laterar inflow of continental groundwater.

The overall dissolution and replacement of evaporites in Member 3 of the BDF is assumed to have occurred prior to metamorphism, driven by flushing from resurging groundwater in the capillary zone. During the Grampian Orogeny, pseudomorphs were tilted, and strain fringes formed in areas where pyrite had been displaced. Metamorphism increases the mobility of Fe, and the complete pyritisation of gypsum pseudomorphs in Beds 7 and 15 may be linked to this process. As Bed 7 is associated with the Bed 8, containing columnar stromatolites, the complete pyritisation of gypsum in this bed may also reflect an influx of marine water, contributing further Fe enrichment.

The vertical movement of capillary brine is also reflected in fluctuating oxygen levels (Warren, 2016). The consistent presence of goethite replacing pyrite is interpreted to reflect anoxic groundwater rising and oxic groundwater sinking, after being oxygenated near or at the surface of the sabkha.

Thoughts on Former Interpretations of Depositional Facies

Previous studies (Spencer & Spencer, 1972) (Fairchild, 1980) of Member 3 of the BDF ruled out evaporite formation and a system controlled by capillary brine. This conclusion was based on the absence of documented intrasedimentary evaporites and the presence of low-porosity sand beds, which were assumed to inhibit capillary flow. However, more recent research (Warren, 2016) has demonstrated that capillary rise can occur through seemingly impermeable beds, provided they do not exceed a critical thickness (see Introduction, Table 1). All previously inferred impermeable beds within Member 3 fall below this threshold. Furthermore, this study demonstrates that intrasedimentary evaporite pseudomorphs are not absent—they are extensively present. Together, these findings prompt a revision of earlier interpretations of the depositional facies and palaeoclimate of the BDF.

Spencer & Spencer (1972) and Fairchild (1980) interpreted the depositional setting of Member 3 as strandzone facies—ranging from intertidal to supratidal and lagoonal environments—partly based on the presence of stromatolites and microbialites. This study acknowledges that ancient stromatolites and microbial mats are found in both marine and continental freshwater environments, likely due to elevated atmospheric CO_2 concentrations during the time of microbial growth (Warren, 2016) (Lehn et al., 2023).

The interpretation of strandzone facies by Spencer & Spencer (1972) and Fairchild (1980) is supported in this study. First, the presence of columnar stromatolites in Stratigraphic Log 3 suggests a high-energy channel connecting a landward water body to the ocean. Second, giant ripples observed in Stratigraphic Log 1 indicate a transgressive stage involving marine flooding of a supratidal zone—precisely where near-marine sabkhas are typically situated.

The detrital input in the BDF and formation of rippled beds has previously been attributed to precipitation and storm events (Fairchild, 1980) (Spencer & Spencer, 1972). The author of this study agrees that recurring storms and precipitation likely led to deposition of detrital minerals and formation of rippled beds. Detrital minerals are documented in all beds examined in this study, inferring that while evaporatic conditions were continous, so were intense precipitation and storms.

A potential source contributing detrital minerals and Ba^{2+} ions to the BDF is the Rhinns Complex, which today forms the basement of Islay (Fig. 49). It is dated to 1782 ± 5 Ma (Muir et al., 1994) and comprises mylonitic syenite and gabbro.

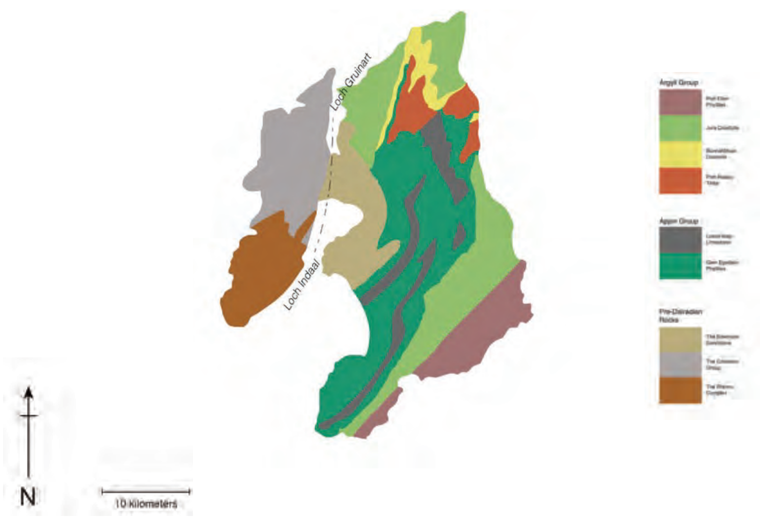

Fig. 49. *Map of Islay today, with geological units mapped out (redrawn from Skelton et al., 1995). The location of the Rhinns Complex at time of deposition of the BDF is unknown.*

Syenite is deficient in quartz and enriched in K-feldspar, with Ba^{2+} concentrations ranging from 500 to 2000 ppm. The Rhinns Complex syenite contains anomalously high Ba^{2+} concentrations of up to 2639 ppm. Other minerals present in the Rhinns Complex include biotite, fluorapatite, zircon, rutile, and ilmenite (Muir et al., 1994).

If the Rhinns Complex was geographically close to the depositional area of the BDF at the time, it is a plausible source of detrital minerals and partial Ba^{2+} enrichment observed in Member 3 of the BDF. Additionally, the heavy mineral concentration in Bed 29 includes two detrital alteration products: leucoxene, and a multigranular texture composed of dolomite, fluorapatite, and quartz. The Rhinns Complex host minerals required for their formation.

Connection to the Sea

The variation in stromatolite morphology and height within Bed 8 indicates a period with differences in water depth and energy levels within the same body of water. The group of columnar stromatolites which are connected at the surface are interpreted to have formed in a channel connecting a former continental water body to the open sea. The domal stromatolites are inferred to have developed in lower-energy, shallower waters (Fig. 50).

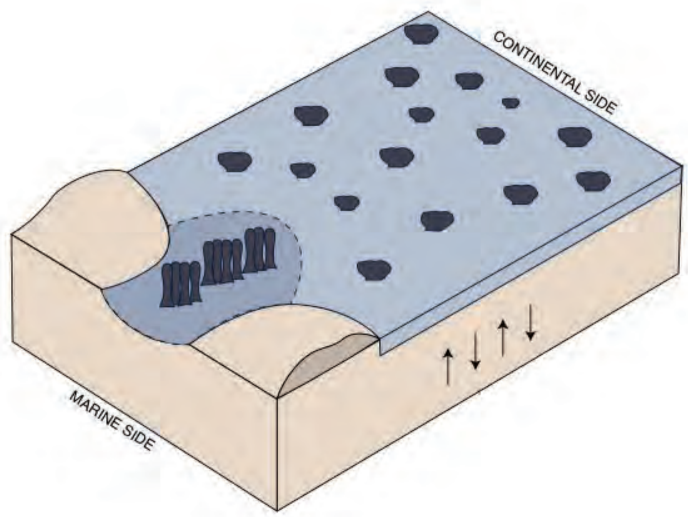

Fig. 50. *Hypothetic disposition of columnar and domal stromatolites, occurring in the same bed. Arrows mark capillary flow. Not to scale.*

Bed 6, the bed with concentrations of anhydrite nodules, is deposited shortly before the appearance of stromatolites in Bed 8. In Bed 6, calcification of dolomite is inferred. This could be linked to an increase of the concentration of bicarbonate in the brine. At the time of deposition of the BDF, high atmospheric CO2 levels in the aftermath of Snowball Earth are reflected in high amounts of CO2 dissolving in water. Dissolution of CO2 in water leads to formation of bicarbonate (Hoffman, 2017). Influence of meteoric water in lowerlying beds has not led to calcification of dolomite, and it is inferred that the bicarbonate was likely derived from marine water.

Bed 6 also contain celestite. This could reflect an influx of Sr-rich marine water. It could also reflect the depletion of Br2+ in the brine (Hanor, 2000). As there is a high abundance of baryte in this bed, one might conclude the precipitation of baryte increased the Sr/Br ratio, eventually precipitating celestite.

Transgressive Stage

The giant ripples (Fig. 22) seen in Bed 4 indicate a transgressive stage (Hoffman, 2017). This bed was deposited shortly after Bed 3 (Fig. 19–21), in which siliciclastic laths and protrusions have previously been interpreted as distorted mudcracks filled with sand (Spencer & Spencer, 1972; Fairchild, 1980). At the time of those interpretations, evaporites had not been documented in the BDF. With gained insight in evaporitic conditions, this study offers an alternative interpretation: repeated haloturbation and replacement of former evaporite accumulations. This is supported by typical features of haloturbated beds—such as chicken-wire structures and evaporitic pseudomorphs with rugose rims connected to both the siliciclastic and black matrices (Warren, 2016).

Haloturbation is commonly connected to marine flooding of sabkhas situated in the supratidal zone (Warren, 2016). As Bed 4 was deposited shortly after Bed 3, the suggested haloturbated and replaced salt beds might be linked to the transgressive stage. This implies that some of the water causing haloturbation was marine. Terrestrial input is indicated by the presence of zircon, Ba-bearing feldspars, Ti-bearing albite, and relatively large, rounded quartz grains. Their presence suggests that meteoric water also played a role in the flooding. As detrital minerals are most abundant in the siliciclastic replacement matrix, the dissolution and replacement of salt beds are thought to have been primarily driven by meteoric water influx. The black matrix may reflect a predominantly marine influx, depositing mud that was later dolomitised by capillary flow. Even though the siliciclastic structures are well cemented, the thin laths would still enable capillary rise (Table 1) (Warren, 2016). Each time flooding of the sabkha withdraws, evaporation of surface water results in deposition of a new cumulate of salt. As flooding recurs, this cycle repeats—ultimately producing 21 m of strata with repeated haloturbation features. The giant ripples are thought to represent intense storms at the end of the transgressive stage.

Bed 2 contain kaolinite, which is typical for warm, wet tropical environments with adjoined extensive leaching (Limmer et al., 2012).

The presence of kaolinite alongside pseudomorphs of gypsum increase the insight in the extremely varying climate conditions during deposition of the BDF. Bed 2 is thought to reflect a transitional stage in between Bed 1, which apart from detrital input of fluorapatite and rutile, shows little signs of a wet period, and Bed 3, where marine and meteoric flooding of the sabkha appear.

Transgressive stages are typically extensive in post-Marinoan sequences but minor or absent in post-Sturtian sequences. Linking Bed 3 and the overlying giant ripples to a transgressive stage raises the question of whether the BDF represents post-Sturtian or post-Marinoan deposition. However, post-Marinoan sequences commonly contain seafloor-precipitated baryte and aragonite fans (Rugen et al., 2024). In contrast, all baryte in Member 3 of the BDF occurs as a replacement mineral within pseudomorphs—a texture associated with capillary brine dissolution and replacement (Warren, 2016). No former aragonite fans have been observed in this study. One bed contains minor Sr-bearing calcite and dolomite. Although calcite and dolomite derived from aragonite are often enriched in Sr, the Sr-bearing carbonates in this case are only found within intrasedimentary gypsum and anhydrite pseudomorphs.

Furthermore, banded iron formations—associated with Sturtian glaciation—are present in the Port Askaig Formation (PAF), which directly underlies the BDF. Isotopic measurements of the Lossit Limestone, which underlies the PAF, match Tonian ocean chemistry (Rugen et al., 2024).

Therefore, although a transgressive stage is recorded in Member 3 of the BDF, the overall evidence supports a post-Sturtian climatic setting.

Further Structures Linked to Dissolution and Schizohaline Conditions

Haloturbation, as suggested being the cause of the chaotic siliciclastic structure of Bed 3, is indicative of schizohaline conditions. Bed 5, a brecciated dolomitic bed with teepee structures, also indicates schizohaline conditions. While intrabreccia and teepee structures can form in various settings, in sabkhas they are commonly linked to the lowering of the saline water table, allowing intrusion of less saline surface waters (Warren, 2016). The presence of mudcracks connected to brecciated sections indicate this bed was at the surface during brecciation and formation of teepee structures.

In Beds 27 and 29, density inversion structures involving an enterolithic dolomitic bed point to differential dissolution of a salt bed.

Dissolution of hydrous evaporites, as gypsum, cause liquefaction and would have allowed the overlying accumulation of heavy minerals to slump into the salt bed as it dissolves.

The presence of gypsum pseudomorphs in Bed 29 further supports this interpretation. As salt beds dissolve, they leave behind insoluble residues which, in the capillary zone, become dolomitised by resurging groundwater (Warren, 2016). The accumulation of abundant heavy minerals is inferred to be linked to severe storm events. Storm activity may trigger ground shaking, enhancing the downward movement of dense deposits through liquefied remnants of a former salt bed. The presence of multiple pseudonodules separating from the black bed in Bed 29 suggests repeated intense shaking (Owen, 1978). The accumulation of chert in Bed 29 is yet another indicator of dissolution of salt (Warren, 2016). For a salt bed to form on the surface, evaporation of a saline brine is required (Warren, 2016). Such beds may reflect deposition in a saline pan—a depression in the sabkha where the capillary fringe crops out.

Metamorphic Grade

Member 3 of the BDF is mapped within a region affected by regional greenschist facies metamorphism at chlorite grade (Harte & Graham, 1975). In this study, no chlorite was detected in any of the 14 beds examined in thin section. Instead, biotite was observed in seven beds, from Bed 15 and upward in the stratigraphic column. SEM results show no evidence of biotite chloritisation. The biotite appears as strain fringes of pyrites, aligned with muscovite in the matrix of one bed and in the interior of rimmed pseudomorphs.

In two of the seven beds, Bed 29 (Fig. 44B) and 31, biotite is classified as detrital based on its texture and association with other detrital minerals and detrital mineral textures. This biotite shows no signs of metamorphic alignment.

Beds 15 (Fig. 33D), 17 (Fig. 36D) and 26 (Fig. 39) contain pseudomorphs that include biotite with irregular shape in their interiors. The biotite appears to conform to surrounding minerals and does not display distinct crystal shapes. The dissolution of evaporites creates vacant pore spaces, which, in sabkha environments, are typically filled by minerals precipitated from capillary brines (Warren, 2016). Detrital biotite would not be expected within the interior of pseudomorphs unless the evaporite dissolved immediately at the surface, leaving an open vug subsequently filled by multiple detrital minerals. Fast dissolution at the surfce would not yield a rim.

The texture and positioning of biotite within rimmed pseudomorphs and in strain fringes of pyrite supports the interpretation that the biotite is of metamorphic origin.

Biotite observed aligned within muscovite in Bed 25 is likewise interpreted as metamorphic.

Member 3 of the BDF exhibits a continuous presence of K-feldspar and is also enriched in Fe and Mg, while Al content remains consistently low. In pelitic rocks with low Al concentrations, biotite can be stable at chlorite-grade conditions (Miyashiro & Shido, 1985). Furthermore, Member 3 is crosscut by several Palaeogene dolerite dykes (Fairchild, 1980). Contact metamorphism can locally raise temperatures (Neiva, 1980). As no chlorite has been documented in this study, it is argued that local bulk rock composition, combined with the possible effects of contact metamorphism, resulted in the development of a local biotite zone within a regionally chlorite-grade metamorphic setting.

5. Conclusion

This study identifies the depositional environment of Member 3 of the BDF as a sabkha, with estimated formation temperatures of at least 35 °C for all beds examined in thin section. Precipitation levels are inferred to have far exceeded those of modern sabkhas. These findings update previous interpretations regarding hydrology and paleoclimate during deposition. Additionally, the study proposes that the local metamorphic grade corresponds to greenschist facies at biotite grade, rather than chlorite grade.

The primary aim of this study was to identify paleoclimate indicators in Member 3 of the BDF. An extensive presence of evaporitic pseudomorphs has been documented. Furthermore, features such as the haloturbated bed, teepee structures, intrabreccias, and beds affected by differential saltbed dissolution are all associated with processes of precipitation, dissolution, and replacement of evaporites.

Extreme precipitation and elevated temperatures would be expected globally in the aftermath of a panglaciation. Thus, the findings of this study provide further support for the Snowball Earth hypothesis.

6. Acknowledgments

Alasdair Skelton, your ability to reflect your passion for geology on to us students was a big part in why I decided to complete this program. I am forever thankful for this and for your immense support during the work with this thesis. Thank you for sharing your knowledge and valuable contacts with me and for making me feel appreciated for my efforts and ideas. Thank you, Anton Eriksson for assisting me during most of my field study. You carried a heavy load of samples, tent and my endless talking. Thank you, Ian Fairchild for taking the time to discuss various ideas, your experience and feedback helped me evolve my conclusions. Thank you to my beloved sister Jennifer Elvestedt for your help in digitalizing some of my handmade sketches, and redrawing some pre-existing illustrations, seen in Fig. 1, 10, 49 and 50. Thank you Andreas Karlsson at NRM, for sharing your huge knowledge in working with the SEM and with Raman spectroscopy. Thank you, Ian Pitcairn for including me in the reflective microscopy-lab, as my samples are packed with sulfides and oxides it was of great interest. And thank you to my wonderful kids, Ines and Anton, for applauding me all the way. You believing in me gave me the courage to switch careers mid-life, you inspire me to spend my days on something truly meaningful.

7. References

Anovitz, L.M. & Essene, E.J., 1987. Phase equilibria in the system $CaCO_3$-$MgCO_3$-$FeCO_3$. Journal of Petrology, 28(3), pp.389–414.

Aref, M.A. & Mannaa, A.A., 2021. The significance of gypsum morphology in interpreting environmental changes caused by human construction, Red Sea coastal evaporation environment, Saudi Arabia. Environmental Earth Sciences, 80(47). https://doi.org/10.1007/s12665-020-09298-4

Bąbel, M., & Schreiber, B.C. (2014). Geochemistry of evaporite basins and the habitability of Martian environments. In T. Platz, M. Massironi, P.K. Byrne, & H. Hiesinger (Eds.), Volatiles in the Martian Crust (pp. 153-193). Elsevier.

Betkowski, W.B., Harlov, D. & Rakovan, J.F., 2016. Hydrothermal mineral replacement reactions for an apatite-monazite assemblage in alkali-rich fluids at 300–600 °C and 100 MPa. American Mineralogist, 101, pp.2620–2637.

Burkhard, M., 1993. Calcite twins, their geometry, appearance and significance as stress-strain markers and indicators of tectonic regime: A review. Journal of Structural Geology, 15(3–5), pp.351–368. https://doi.org/10.1016/0191-8141(93)90132-T

Church, M., 1997. Bed material transport and the morphology of alluvial river channels. Annual Review of Earth and Planetary Sciences, 34, pp.325–354.

Cocks, L.R.M., Torsvik, T.H. & Robin, M., 2011. The Palaeozoic geography of Laurentia and western Laurussia: A stable craton with mobile margins. Earth-Science Reviews, 106(1–2), pp.1–51. https://doi.org/10.1016/j.earscirev.2011.01.007

Dalziel, I.W.D. & Soper, N.J., 2001. Neoproterozoic extension on the Scottish Promontory of Laurentia: Paleogeographic and tectonic implications. The Journal of Geology, 109(3), pp.299–317. https://doi.org/10.1086/319972

Deysel, K., 2007. Leucoxene study: a mineral liberation analysis (MLA) investigation. In: The 6th International Heavy Minerals Conference – Back to Basics. Johannesburg: The Southern African Institute of Mining and Metallurgy.

Dill, H.G., 1998. A review of heavy minerals in clastic sediments with case studies from the alluvial-fan through the nearshore-marine environments. Earth-Science Reviews, 45(1–2), pp.103–132. https://doi.org/10.1016/S0012-8252(98)00036-3

Duverger, A., Berg, J.S., Busigny, V., Guyot, F., Bernard, S. & Miot, J., 2020. Mechanisms of pyrite formation promoted by sulfate-reducing bacteria in pure culture. Frontiers in Earth Science, 8, Article 588310. https://doi.org/10.3389/feart.2020.588310

El Tabakh, M., Schreiber, B.C., & Warren, J.K., 1998. Origin of fibrous gypsum in the Newark rift basin, eastern North America. Journal of Sedimentary Research, 68(1), pp.88–99. https://doi.org/10.2110/jsr.68.88

Fairchild, I.J., 2018. Tonian–Cryogenian boundary sections of Argyll, Scotland. Precambrian Research, 319, pp.207–229. https://doi.org/10.1016/j.precamres.2017.09.019

Fairchild, I.J., 1980. Sedimentation and origin of a late Precambrian dolomite from Scotland. Journal of Sedimentary Petrology, 50(2), pp.423–446. https://doi.org/10.1306/212F7A7D-2B24-11D7-8648000102C1865D

Farías, M.E., Contreras, M., Rasuk, M.C. et al., 2014. Characterization of bacterial diversity associated with microbial mats, gypsum evaporites and carbonate microbialites in thalassic wetlands: Tebenquiche and La Brava, Salar de Atacama, Chile. Extremophiles, 18, pp.311–329. https://doi.org/10.1007/s00792-013-0617-6

Friedman, G.M., 1980. Concepts and Models of Dolomitization. SEPM Special Publication, 28, pp.215–235. https://doi.org/10.2110/pec.80.28.0215

Hanor, J.S., 2000. Barite–Celestine geochemistry and environments of formation. Reviews in Mineralogy and Geochemistry, 40(1), pp.193–275. https://doi.org/10.2138/rmg.2000.40.4

Hanor, J.S., 2001. Reactive transport involving rock-buffered fluids of varying salinity. Geochimica et Cosmochimica Acta, 65, pp.3721–3732.

Hardie, L.A., 1978. Anhydrite and gypsum. In: Fairbridge, R.W. (ed.) Sedimentology. Encyclopedia of Earth Science. Springer, Berlin, Heidelberg. https://doi.org/10.1007/3-540-31079-7_7

Harte, B. & Graham, C.M., 1974. The graphical analysis of greenschist to amphibolite facies mineral assemblages in metabasites. Journal of Petrology, 15(3), pp.238–273.

Hoffman, P.F., Abbot, D.S., Ashkenazy, Y., Benn, D.I., Brocks, J.J., Cohen, P.A., Cox, G.M., Creveling, J.R., Donnadieu, Y., Erwin, D.H., Fairchild, I.J., Ferreira, D., Goodman, J.C., Halverson, G.P., Jansen, M.F., Le Hir, G., Love, G.D., Macdonald, F.A., Maloof, A.C., Partin, C.A., Ramstein, G., Rose, B.E.J., Rose, C.V., Sadler, P.M., Tziperman, E., Voigt, A. & Warren, S.G., 2017. Snowball Earth climate dynamics and Cryogenian geology–geobiology. Science Advances, 3(11), e1600983. https://doi.org/10.1126/sciadv.1600983

Hoffman, P.F., Kaufman, A.J., Halverson, G.P. & Schrag, D.P., 1998. A Neoproterozoic Snowball Earth. Science, 281(5381), pp.1342–1346.

Katz, A., Sass, E., Starinsky, A. & Holland, H.D., 1972. Strontium behavior in the aragonite–calcite transformation: An experimental study at 40–98 °C. Geochimica et Cosmochimica Acta, 36(4), pp.481–496. https://doi.org/10.1016/0016-7037(72)90037-3

Keeling, J., 2004. Metal ion dispersion through transported cover at Moonta, South Australia. In: Roach, I.C. (ed.), Regolith 2004: Proceedings of the CRC LEME Regional Regolith Symposia. CRC LEME, pp.233–238.

Kennedy, M.J., Christie-Blick, N. & Sohl, L.E., 2001. Are Proterozoic cap carbonates and isotopic excursions a record of gas hydrate destabilization following Earth's coldest intervals? Geology, 29, pp.443–446. https://doi.org/10.1130/0091-7613(2001)029<0443:APCCAI>2.0.CO;2

Kirschvink, J.L., 1992. Late Proterozoic low-latitude global glaciation: the Snowball Earth. In: Schopf, J.W. & Klein, C. (eds), The Proterozoic Biosphere: A Multidisciplinary Study. Cambridge University Press, pp.51–52.

Kuisma-Kursula, P., 2000. Accuracy, precision and detection limits of SEM-WDS, SEM-EDS and PIXE in the multi-elemental analysis of medieval glass. X-Ray Spectrometry, 29(1), pp.111–118.

Lan, Z., Chen, Z.-Q., Wang, Y., & Zheng, X., 2012. Megaripples from the Mesoproterozoic of the Kimberley region, northwestern Australia and its geological implications. Journal of Palaeogeography, 1(1), pp.15–25. https://doi.org/10.3724/SP.J.1261.2012.00015

Lehn, I., Paim, P.S.G. & Chemale Jr., F., 2023. From the sea to the land: How microbial mats dominated marine and continental environments in the Ediacaran Camaquã Basin, Brazil. Precambrian Research, 385, 106751.

Leica Microsystems, n.d. Brief introduction to coating technology for electron microscopy. [online] Available at: https://www.leica-microsystems.com/science-lab/life-science/brief-introduction-to-coating-technology-for-electron-microscopy/ [Accessed 15 March. 2025].

Li, Z.X., Bogdanova, S.V., Collins, A.S., Davidson, A., De Waele, B., Ernst, R.E., Fitzsimons, I.C.W., Fuck, R.A., Gladkochub, D.P., Jacobs, J., Karlstrom, K.E., Lu, S., Natapov, L.M., Pease, V., Pisarevsky, S.A., Thrane, K. & Vernikovsky, V., 2008. Assembly, configuration, and break-up history of Rodinia: A synthesis. Precambrian Research, 160(1–2), pp.179–210. https://doi.org/10.1016/j.precamres.2007.04.021

Limmer, D.R., Manners, H.R., Dixon, R.J., Clift, P.D., Gaedicke, C., Schwenk, T. & White, L.T., 2012. Chemical weathering and provenance evolution of Holocene–Recent sediments from the Western Indus Shelf, Northern Arabian Sea inferred from physical and mineralogical properties. Marine Geology, 326–328, pp.101–115. https://doi.org/10.1016/j.margeo.2012.07.009

Loughland, R.A., Al-Khayat, J.A., Fadel, I., & Krupp, F., 2016. Coastal Sabkha (Salt Flats) of the Southern and Western Arabian Gulf. In: Khan, M.A., Böer, B., Öztürk, M., Al Abdessalaam, T.Z., Clüsener-Godt, M., & Gul, B. (eds) Sabkha Ecosystems: Volume IV: Cash Crop Halophyte and Biodiversity Conservation. Springer, Dordrecht, pp. 1–14. https://doi.org/10.1007/978-94-007-7411-7_14

McLoughlin, N., 2014. Stromatolites. In: Amils, R. et al. (eds), Encyclopedia of Astrobiology. Springer, Berlin, Heidelberg. https://doi.org/10.1007/978-3-642-27833-4_1528-3

Miyashiro, A. & Shido, F., 1985. Tschermak substitution in low- and middle-grade pelitic schists. Journal of Petrology, 26(2), pp.449–487. https://doi.org/10.1093/petrology/26.2.449

Milodowski, A.E., Morgan, D.J. & Warne, S.St.J., 1989. Thermal analysis studies of the dolomite–ferroan dolomite–ankerite series. II. Decomposition mechanism in flowing CO_2 atmosphere. Thermochimica Acta, 152(2), pp.279–297.

Mougenot, D. & Al-Shakhis, A.A., 1999. Depth imaging sub-salt structures: A case study in the Midyan Peninsula (Red Sea). GeoArabia, 4(4), pp.445–464. https://doi.org/10.2113/geoarabia0404445

Mücke, A. & Bhadra Chaudhuri, J.N., 1991. The continuous alteration of ilmenite through pseudorutile to leucoxene. Ore Geology Reviews, 6(1), pp.25–44.

Muir, R.J., Fitches, W.R. & Maltman, A.J., 1994. The Rhinns Complex: Proterozoic basement on Islay and Colonsay, Inner Hebrides, Scotland, and on Inishtrahull, NW Ireland. Transactions of the Royal Society of Edinburgh: Earth Sciences, 85, pp.77–90.

Neiva, A.M.R., 1980. Chlorite and biotite from contact metamorphism of phyllite and metagraywacke by granite, aplite-pegmatite and quartz veins. Chemical Geology, 29(1–4), pp.49–71.

Owen, G., 1978. Ball-and-pillow (pillow) structure. In: Middleton, G.V. et al. (eds), Encyclopedia of Sediments and Sedimentary Rocks. Encyclopedia of Earth Sciences Series. Springer, Dordrecht. https://doi.org/10.1007/978-1-4020-3609-5_18

Roberts, J.L. & Treagus, J.E., 1979. Stratigraphical and structural correlation between the Dalradian rocks of the SW and Central Highlands of Scotland. In: Harris, A.L., Holland, C.H., & Leake, B.E. (eds) The Caledonides of the British Isles—Reviewed. Geological Society, London, Special Publications, 8, pp. 199–204. https://doi.org/10.1144/GSL.SP.1979.008.01.19

Rosen, M.R. & Warren, J.K., 1990. The origin and significance of groundwater-seepage gypsum from Bristol Dry Lake, California, USA. Sedimentology, 37(6), pp.983–996. https://doi.org/10.1111/j.1365-3091.1990.tb01848

Rugen, E.J., Pastore, G., Vermeesch, P., Spencer, A.M., Webster, D., Smith, A.G.G., Carter, A., & Shields, G.A., 2024. Glacially influenced provenance and Sturtian affinity revealed by detrital zircon U-Pb ages from sandstones in the Port Askaig Formation, Dalradian Supergroup. Journal of the Geological Society. https://doi.org/10.1144/jgs2024-029

Spencer, A.M. & Spencer, M.O., 1972. The Late Precambrian/Lower Cambrian Bonahaven Dolomite of Islay and its stromatolites. Scottish Journal of Geology, 8(4), pp.269–282. https://doi.org/10.1144/sjg08040269

Taylor, S.R. & McLennan, S.M., 1985. The Continental Crust: Its Composition and Evolution. Blackwell Scientific Publications, Oxford.

Warren, J.K., 1997. Evaporites, brines and base metals: fluids, flow and 'the evaporite that was'. Australian Journal of Earth Sciences, 44(2), pp.149–183. https://doi.org/10.1080/08120099708728305

Warren, J.K., 2016. Evaporites: A Geological Compendium, 2nd edition. Springer, Berlin. https://doi.org/10.1007/978-3-319-13512-0

Yaroshevsky, A.A., 2006. Abundances of chemical elements in the Earth's crust. Geochemistry International, 44, pp.48–55. https://doi.org/10.1134/S001670290601006X

Yi, H., Balan, E., Gervais, C., Segalen, L., Fayon, F., Roche, D., Person, A., Morin, G., Guillaumet, M., Blanchard, M., Lazzeri, M., & Babonneau, F., 2013. A carbonate-fluoride defect model for carbonate-rich fluorapatite. American Mineralogist, 98(5–6), pp.1066–1069. https://doi.org/10.2138/am.2013.4445

Zi, J.-W., Muhling, J.R. & Rasmussen, B., 2024. Geochemistry of low-temperature (<350 °C) metamorphic and hydrothermal monazite. Earth-Science Reviews, 249, 104668. https://doi.org/10.1016/j.earscirev.2023.104668

Webster, D., Anderton, R., & Skelton, A., 2015. A Guide to the Geology of Islay – An Introduction to Islay's Geological Past with 12 Illustrative Walking Excursions. Ringwood Publishing, Glasgow, pp.24–27.

Appendix 1: unannotated images of thin sections and figures

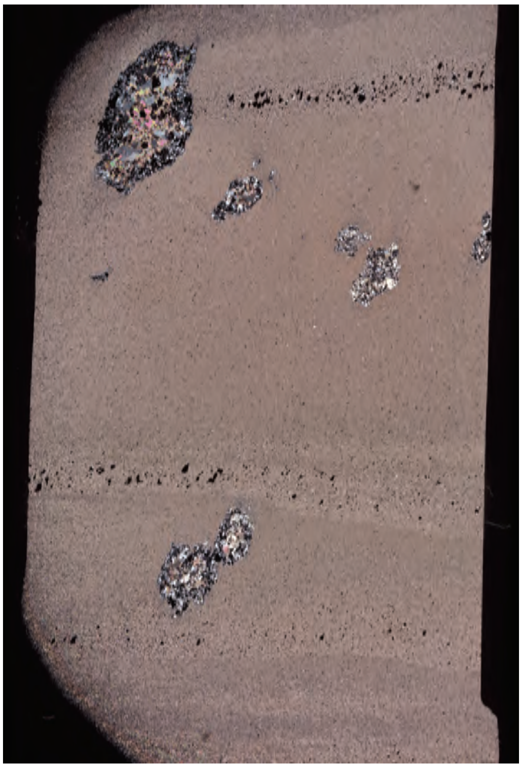

Thin section 24EX07SEA, seen in Fig. 11.

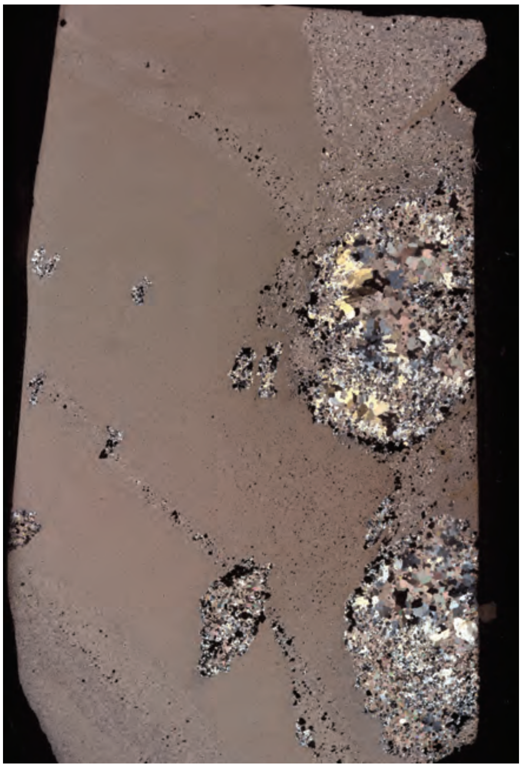

Thin section 24EX06SEA, seen in Fig. 13.

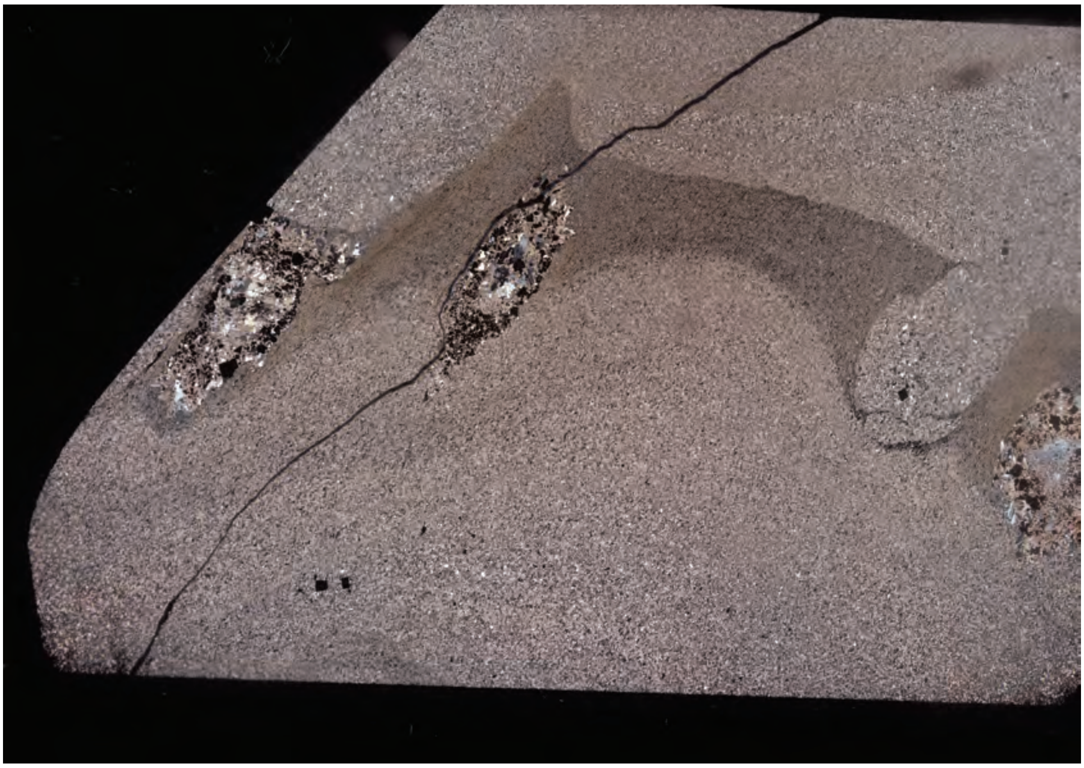

Thin section 24EX04SEC, seen in Fig. 16.

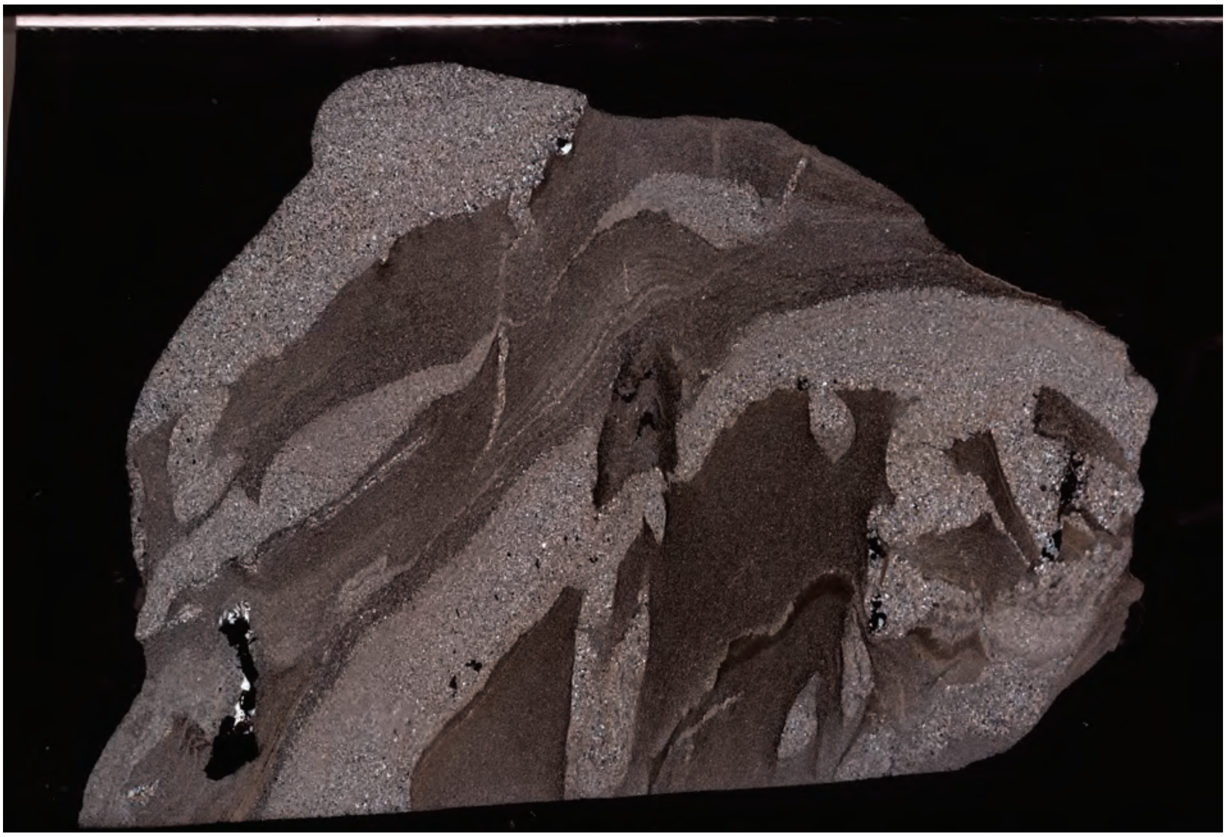

Thin section 24EX05SEC, seen in Fig. 20.

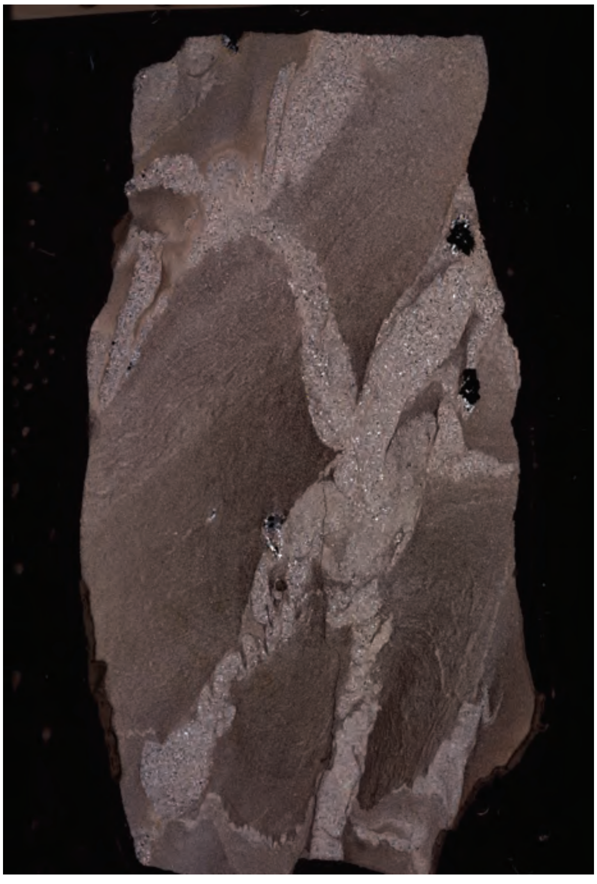

Thin section 24EX05SEG, seen in Fig. 20.

Thin section 24EX16SE, seen in Fig. 29.

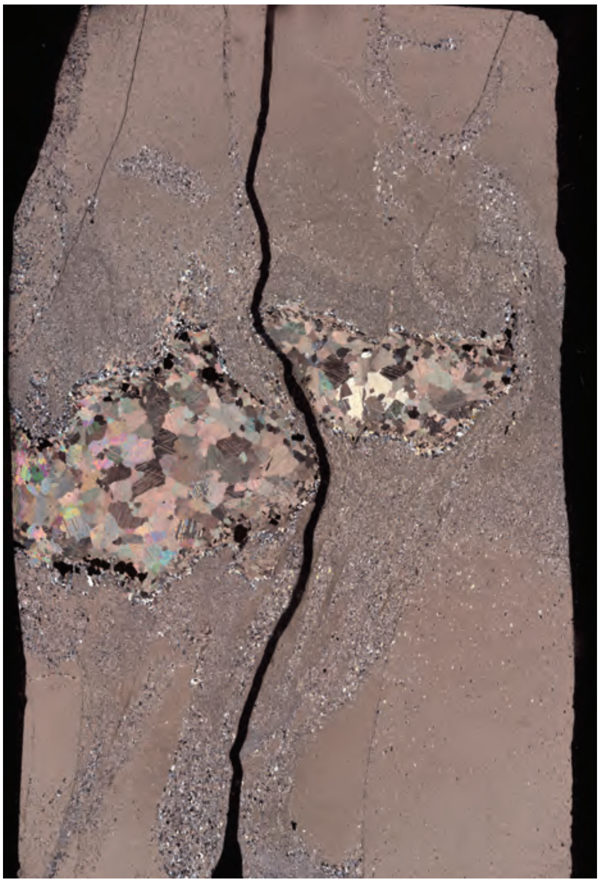

Thin section *24EX26SEG, detail seen in Fig. 24.*

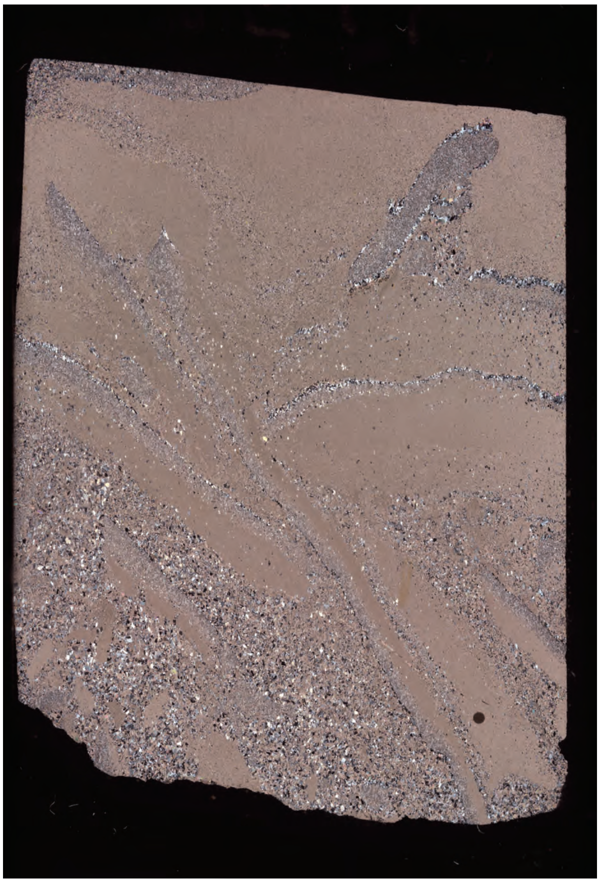

Thin section *24EX26SED, detail seen in Fig. 25.*

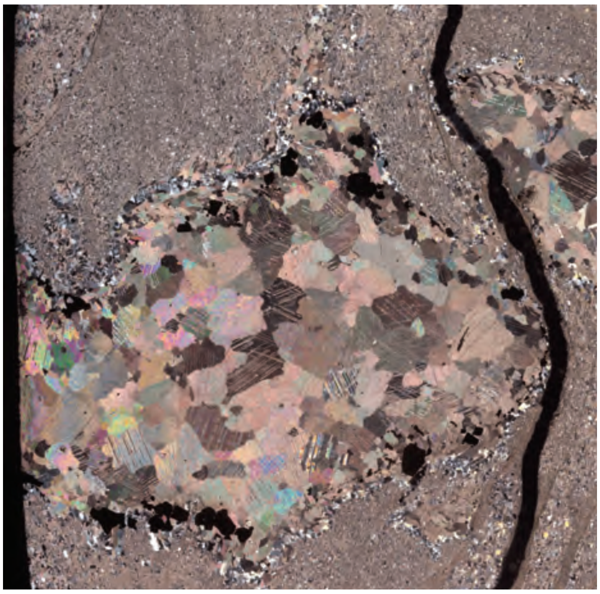

Detail of thin section *24EX26SEG, seen annotated in Fig. 24.*

Detail of thin section *24EX26SED, seen annotated in Fig. 24.*

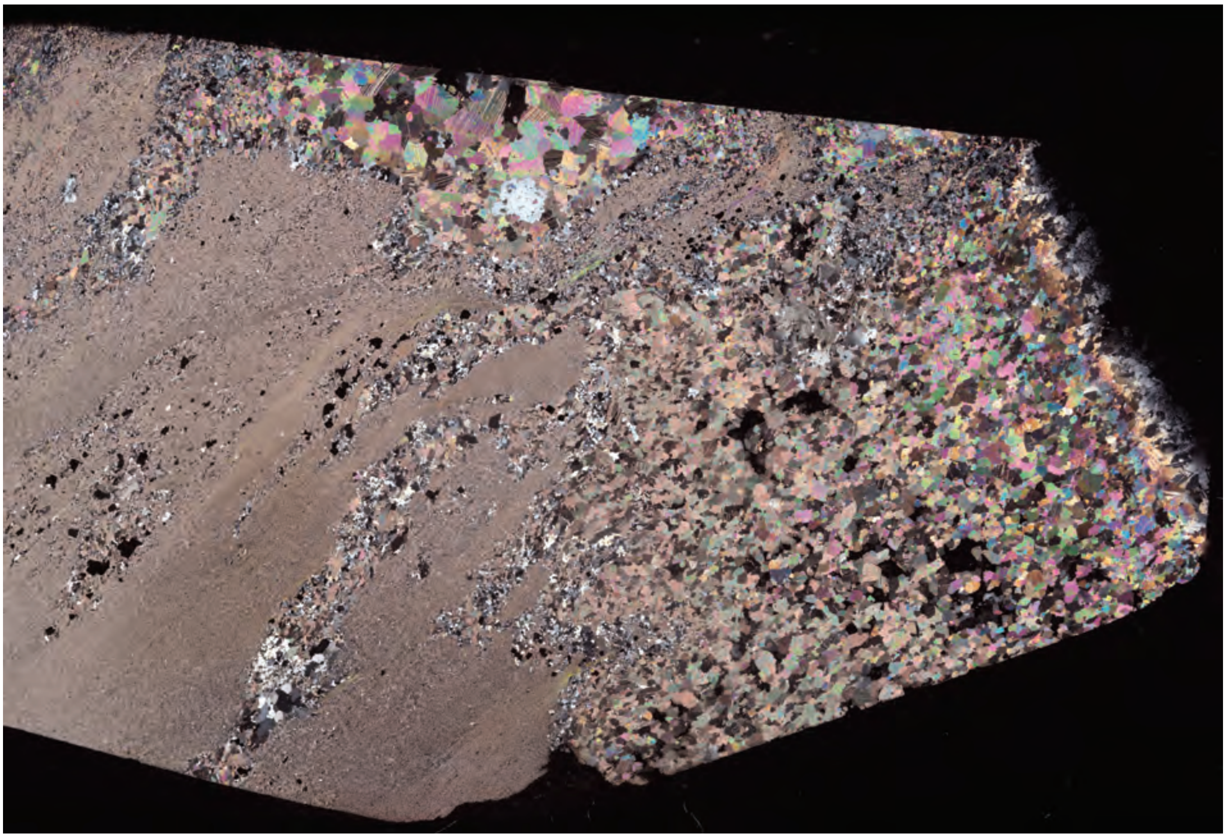

Thin section 24EX111SEB, seen annotated in Fig. 26.

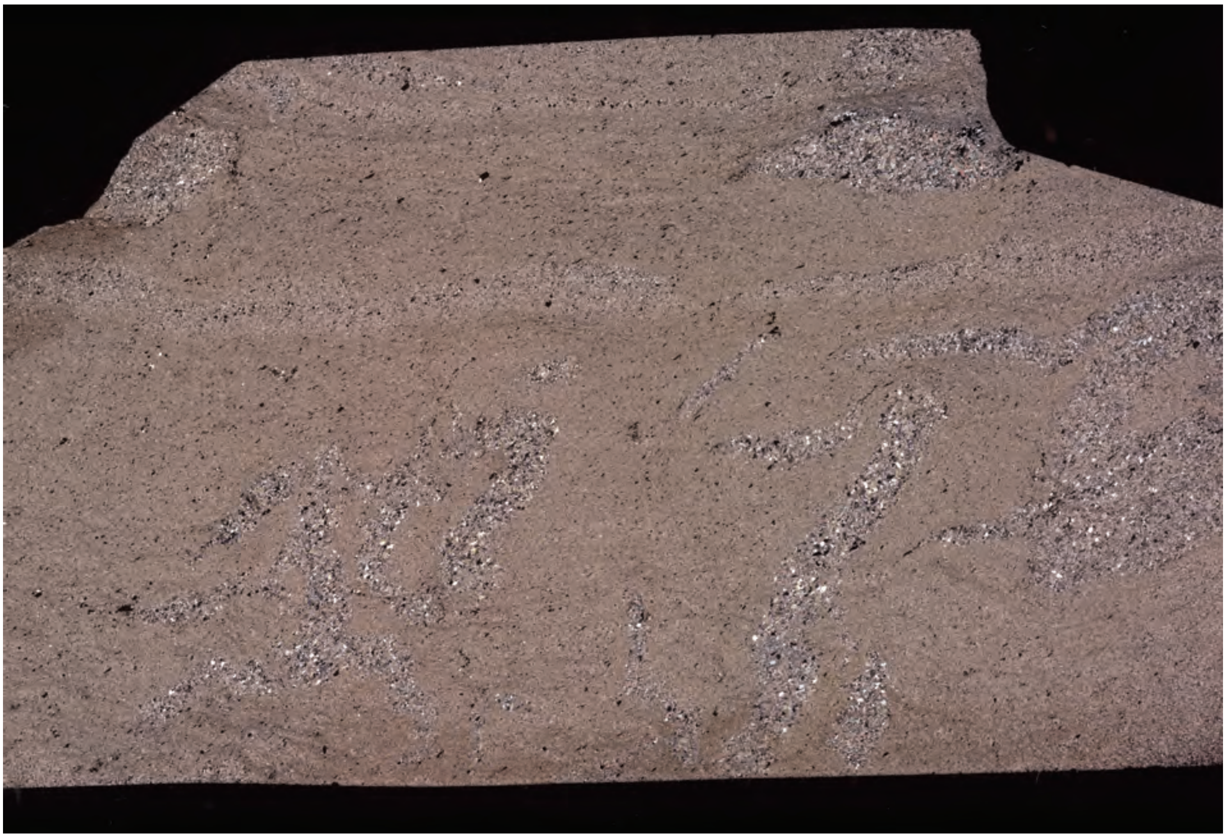

Thin section 24EX01SED, seen cropped in Fig. 31.

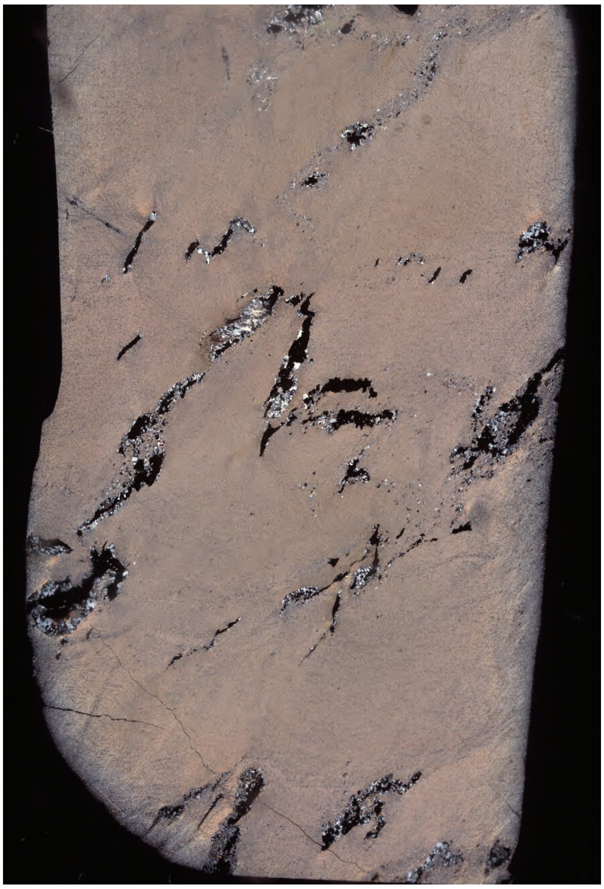

Thin section 24EX100SEB, Fig. 33.

Thin section 24EX12SEB, seen cropped in Fig. 36.

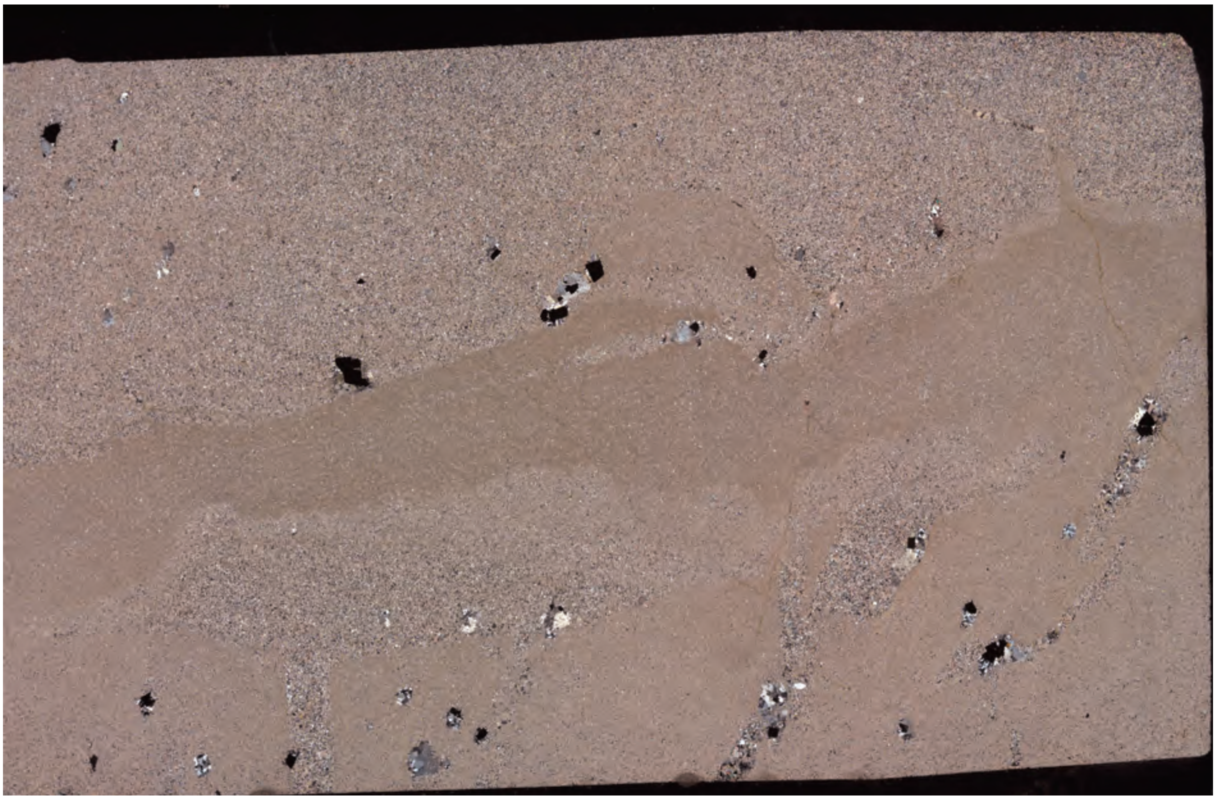

Thin section 24EX23SED, seen cropped and annotated in Fig. 37.

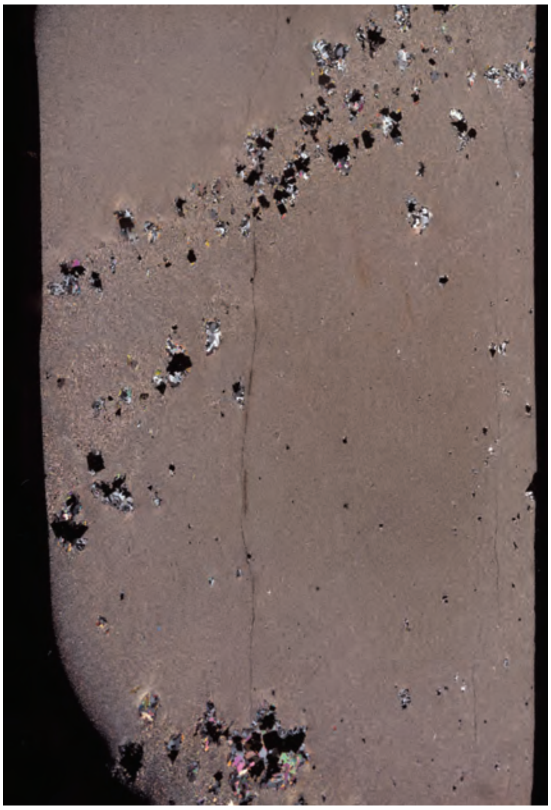

Thin section 24EX17SEA, seen cropped in Fig. 39.

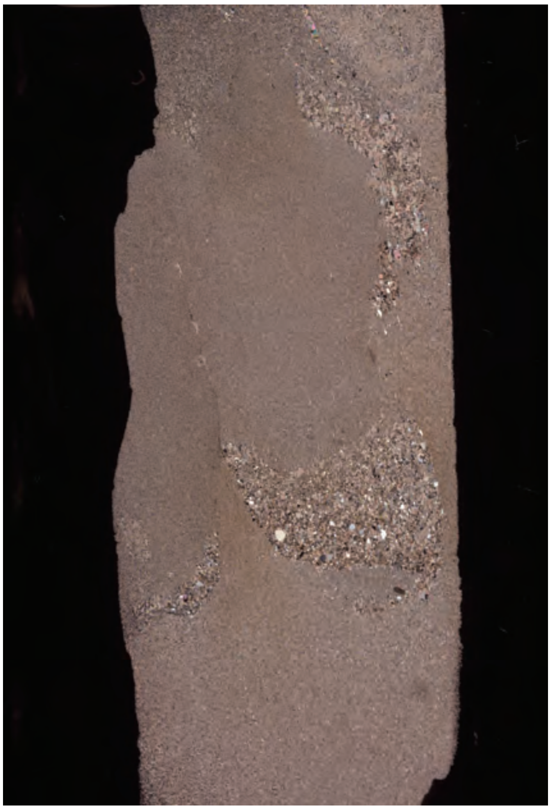

Thin section 24EX27SED, seen annotated in Fig. 42.

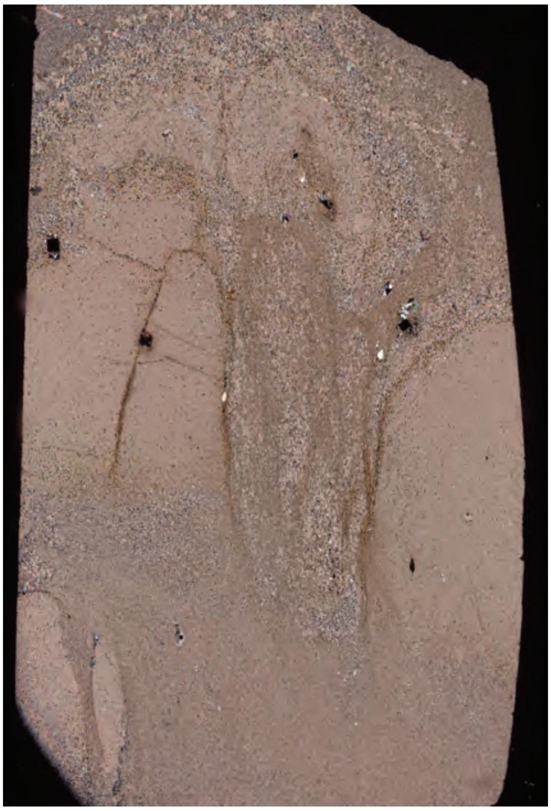

Thin section 24EX13SEB, seen annotated in Figs. 42 and 44.

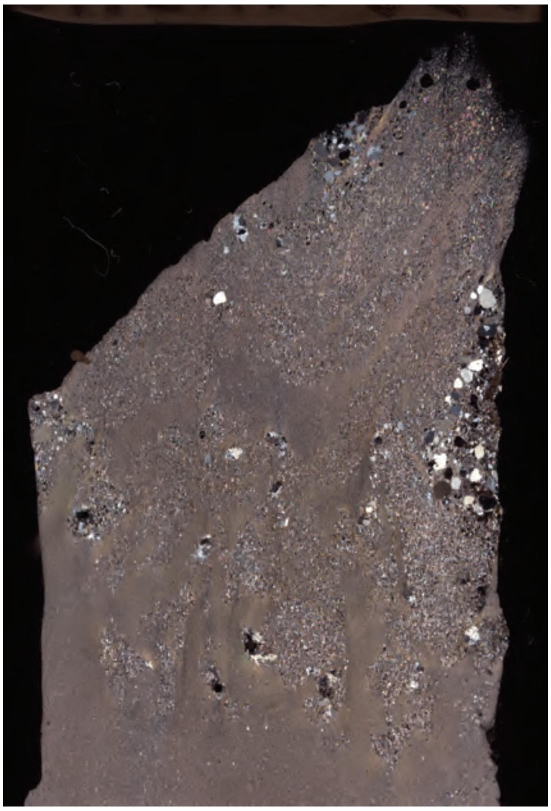

Thin section 24EX10SEC, seen annotated in Fig. 48.

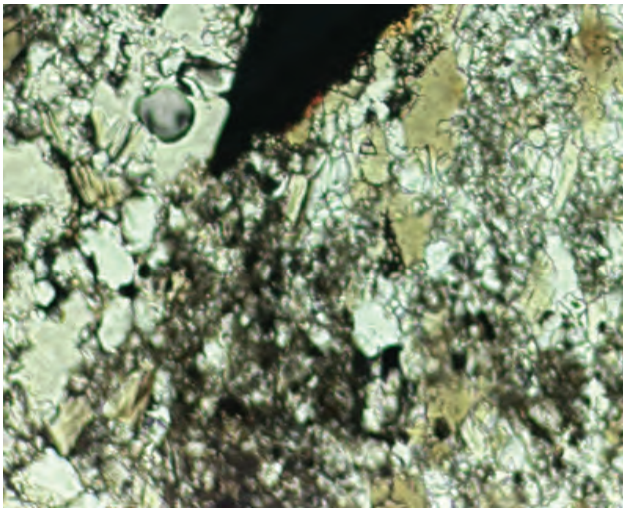

Unannotated version of Fig. 42C, thin section 24EX13SEB

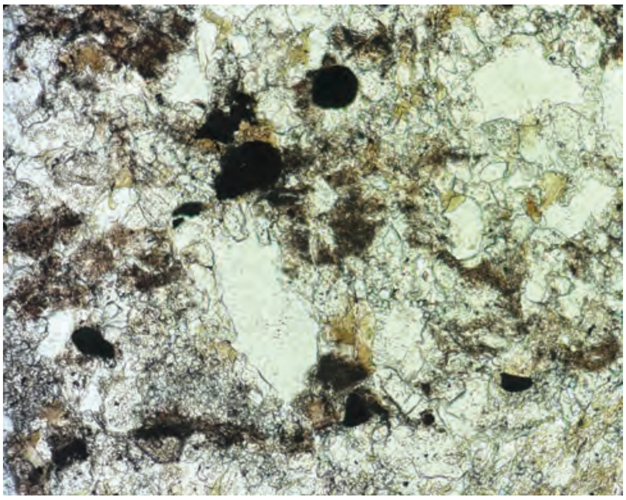

Unannotated version of Fig. 42F, thin section 24EX27SED.

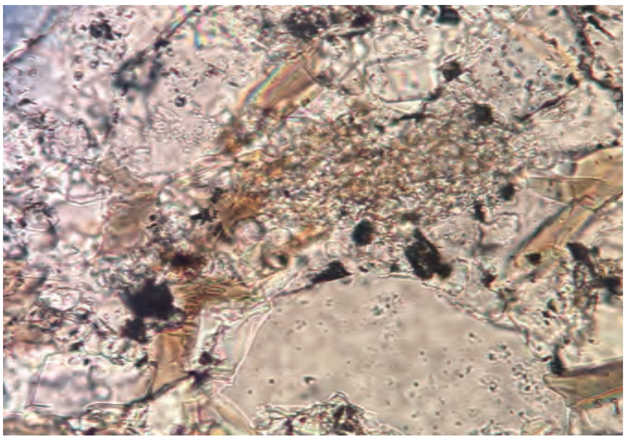

Unannotated version of Fig. 43A, thin section 24EX13SEB.